NOTE TO USERS

This reproduction is the best copy available.

Serrated Flow and Enhanced Ductility in Coarse-Grained Al-Mg Alloys

by

Ehab Samuel

Library and Archives
Canada

Published Heritage
Branch

395 Wellington Street
Ottawa ON K1A 0N4
Canada

Bibliothèque et
Archives Canada

Direction du
Patrimoine de l'édition

395, rue Wellington
Ottawa ON K1A 0N4
Canada

NOTICE:

The author has granted a non-
exclusive license allowing Library and
Archives Canada to reproduce,
publish, archive, preserve, conserve,
communicate to the public by
telecommunication or on the Internet,
loan, distribute and sell theses
worldwide, for commercial or non-
commercial purposes, in microform,
paper, electronic and/or any other
formats.

The author retains copyright
ownership and moral rights in this
thesis. Neither the thesis nor
substantial extracts from it may be
printed or otherwise reproduced
without the author's permission.

AVIS:

L'auteur a accordé une licence non exclusive
permettant à la Bibliothèque et Archives
Canada de reproduire, publier, archiver,
sauvegarder, conserver, transmettre au public
par télécommunication ou par l'Internet, prêter,
distribuer et vendre des thèses partout dans le
monde, à des fins commerciales ou autres, sur
support microforme, papier, électronique et/ou
autres formats.

L'auteur conserve la propriété du droit d'auteur
et des droits moraux qui protège cette thèse. Ni
la thèse ni des extraits substantiels de celle-ci
ne doivent être imprimés ou autrement
reproduits sans son autorisation.

In compliance with the Canadian
Privacy Act some supporting forms
may have been removed from this
thesis.

While these forms may be included
in the document page count, their
removal does not represent any loss
of content from the thesis.

Conformément à la loi canadienne sur la
protection de la vie privée, quelques
formulaires secondaires ont été enlevés de
cette thèse.

Bien que ces formulaires aient inclus dans
la pagination, il n'y aura aucun contenu
manquant.

Canada

ABSTRACT

Aluminum 5XXX alloys are of industrial importance and interest as they combine a wide range of desirable strength, forming and welding characteristics with a high resistance to corrosion. The presence of Mg in these alloys ensures favorable mechanical properties. However, the room temperature stretching performance of these alloys is limited. Moreover, Al-Mg alloys are known for being susceptible to the Portevin-LeChatelier effect when deformed at room temperature. Nevertheless, improvements in ductility can be achieved through warm forming, especially when the ductility approaches superplastic levels.

The aim of this study was to test for enhanced ductility in three *coarse-grained* Al-Mg alloys namely, super-pure Al-3%Mg and Al-5%Mg, and commercial AA 5056 alloy. The temperature-dependent flow stress and rate sensitivity behavior of these alloys was investigated by means of tensile testing using ASTM E8M-04 standard samples. Samples were deformed to 10% strain to allow enough deformation to occur such that serrations in the dynamic strain aging (DSA) temperature/strain rate range would be rendered visible on a stress-strain curve. Using this information, the regions of negative and higher-than-normal strain rate sensitivity ('m') were plotted and tensile tests to failure were performed in the vicinity of maximum 'm'. ASTM E2448-06 standard samples for superplasticity tensile testing were used in this case.

A maximum ductility of 170% was recorded with these samples and this was found to increase to nearly 300% when the gage length was shortened. It was observed that the DSA serrations were more prominent at lower strain rates, higher temperatures and higher Mg

contents. The results of this study show clearly that if the rate sensitivity is high enough, then enhanced ductility in coarse-grained materials is possible at temperatures well below the maximum test temperature.

RÉSUMÉ

Les alliages d'aluminium de la série 5XXX sont d'une grande importance pour l'industrie puisqu'ils combinent un large éventail de résistances, de bonnes caractéristiques de mise en forme et de soudure ainsi qu'une haute résistance à la corrosion. La présence de Mg dans ces alliages assure des propriétés mécaniques favorables. Cependant, à la température ambiante la performance d'étirage de ces alliages est limitée. De plus, les alliages Al-Mg sont connus comme étant susceptibles à l'effet Portevin-Chantelier lorsque déformés à la température ambiante. L'amélioration de la ductilité peut être accomplie par un formage à chaud, spécialement lorsque la ductilité approche les niveaux superplastiques.

Le but de cette étude était de tester l'amélioration de la ductilité pour trois alliages Al-Mg à grains grossiers : super pur Al-3%Mg, Al-5%Mg et l'alliage commercial AA 5056, à proximité de la sensibilité maximale de la vitesse de déformation. Le comportement de la contrainte d'écoulement dépendante de la température et de la sensibilité de la vitesse de ces alliages a été examiné au moyen d'échantillons de traction normalisés selon la norme ASTM E8M-04. Les échantillons ont été déformés à 10% de leur longueur pour permettre suffisamment de déformation, ainsi la dentelure dans la plage de la température/vitesse de déformation du DSA (dynamic strain aging) deviendrait visible sur la courbe contrainte-déformation. En utilisant ces informations, les régions de sensibilité négative et supérieure à la normale de la vitesse de déformation ('m') ont été dessinées et des essais de traction jusqu'à la rupture ont été faits à proximité du 'm' maximum. Des échantillons normalisés (ASTM E2448-06) pour des essais de traction superplastiques ont été utilisés dans ce cas.

Un maximum de 170% de ductilité a été enregistré et cette valeur a monté à tout près de 300% lorsque la longueur de mesure a été raccourcie. Il a été trouvé que la dentelure DSA était plus proéminente à basse vitesse de déformation, en augmentant la température et à concentration élevée de Mg. Les résultats de cette étude montrent clairement que si la sensibilité de la vitesse de déformation est suffisamment haute, alors l'amélioration de la ductilité pour les matériaux à grains grossiers est possible à une température bien inférieure à la température maximale du test.

ACKNOWLEDGMENTS

I would like to express my sincere thanks to Professor John J. Jonas, my thesis supervisor, for his unique approach to research, and for his support and encouragement throughout the course of this study.

Many thanks are also due to the staff members of the Department of Materials Engineering. In particular, I would like to thank Edwin Fernandez and Pierre Vermette for test sample preparation and Barbara Hanley for her support and advice regarding administrative affairs. Special thanks are owed to Dr. Stuart MacEwen and Peter Rice of Novelis (Kingston, ON) for material preparation. I am also grateful to Dr. Real Bouchard for his help with low temperature tensile testing at CANMET Materials Testing Laboratories (Ottawa, ON) as well as for numerous engaging discussions regarding various aspects of the work.

I wish to thank Dr. Stéphane Godet, Dr. Lan Jiang, Dr. Gregg Stewart, Phuong Vo, Dr. Faramarz Zarandi, Dr. Rocco Varano, Dr. Jessica Calvo and Dr. Ahmad Rezaeian for their help, whether through insightful discussions, suggestions regarding alternative testing methods, or for pointing out areas of interest that added to my bank of knowledge. I would also like to thank Alain Bérubé, Julien Tremblay and Mathieu Paradis from Université du Québec à Chicoutimi (UQAC) for their assistance received in this study.

Finally, I would like to express my gratitude to my friends and family for their unwavering support, inspiration, advice and encouragement throughout my studies. I dedicate this thesis to them.

TABLE OF CONTENTS

LIST OF FIGURES

Chapter 2

Chapter 3

Chapter 4

Chapter 5

LIST OF TABLES

CHAPTER 1

INTRODUCTION

Aluminum 5XXX alloys find wide interest in the automotive and aerospace industries since the presence of Mg ensures adequate strength and weldability, as well as desirable ductility and formability characteristics [1-4]. Despite these favorable properties, the room temperature stretching performance of these alloys is limited [4, 5]. Improvements in ductility can be achieved in warm forming, especially in coarse-grained and low impurity Al-Mg alloys, when the ductility approaches superplastic levels, thus removing any need for special microstructure design and/or deformation conditions [1]. Consequently, investigations into the superplastic behavior of Al 5XXX alloys have been a constant focus of interest in research [6-11].

Superplasticity is defined as the ability to achieve high tensile ductilities (usually in excess of several hundred percent) in polycrystalline materials [12-15]. The basic structural requirement for this phenomenon is a microstructure composed of very fine and nearly equiaxed grains; the latter must remain stable during deformation [16-18]. Superplastic materials are typically characterized by a uniformity of flow and lack of necking and are used to produce complex shapes through high temperature deformation at very low stress levels [19-23]. Superplastic flow is traditionally attributed to grain boundary sliding [13, 14, 18, 24].

Recently, certain coarse-grained materials have been reported to exhibit superplasticity [10, 11, 17, 18, 24-29]. However, investigations into this type of deformation have concluded that grain boundary sliding is *not* the underlying mechanism. Although the observed enhanced ductility is modest in coarse-grained materials compared to fine-grained materials [2, 4, 20, 30], if the value of 'm' or the strain rate sensitivity is ≥ 0.3, this eliminates the requirement of a fine grain size [10]. Conventional fine-grained materials often display large tensile elongations in certain temperature ranges above $0.5T_m$ (where T_m is the absolute melting temperature) at strain rates commonly used for tensile testing superplastic materials [13, 14].

Dynamic strain aging (DSA) is a well-known phenomenon that occurs in many alloys as the result of an interaction between solute atoms and moving dislocations during deformation [31-43]. When dislocations encounter solute atoms, they may become pinned and this may result in an increase in the applied or developed stress. Conversely, when such dislocations break away from their solute atmospheres, the stress required is lowered, until a subsequent barrier is encountered. This sporadic increase and decrease in applied stress leads to serrated stress-strain curves (usually after a critical strain), surface marks in the form of Lüders bands and negative strain rate sensitivity in the temperature/strain rate regime where the DSA phenomenon is prevalent.

Although commonly associated with negative strain rate sensitivity [44-49] and a loss in ductility [44, 47, 50], dynamic strain aging is also known to impart a hardening effect on materials such that the flow stress dependence on increasing temperature displays a 'hump' rather than decreasing gradually in the temperature/strain rate regime where DSA occurs [31, 43,

51-55]. In the work of Barnett and Jonas [52, 55], it was shown that at higher temperatures (i.e. out of the DSA regime), this 'hump' effect leads to an abnormal increase in the strain rate sensitivity in the form of a local maximum in the rate sensitivity or 'm' value. The latter is coupled with the negative rate sensitivity that is ordinarily expected of materials subject to DSA. With still higher temperatures, the rate sensitivity returns to normal. This local increase in rate sensitivity results in enhanced elongations for the temperature/strain rate combinations at which the maximum 'm' occurs. The aim of this work was to test for enhanced ductility in *coarse-grained* Al-Mg alloys in the vicinity of the maximum 'm' in order to overcome the need for a fine-grained structure and still obtain larger than normal values of ductility.

A summary of the literature relevant to the occurrence of DSA as well as to superplasticity in Al-Mg alloys, with emphasis on coarse-grained materials, is presented in Chapter 2. The causes and effects of DSA in terms of postulated and refined models, the implications of coarse-grained superplasticity, as well as the trend in strain rate sensitivity are among the subjects covered. It will be shown that DSA is related to rate sensitivity, which in turn is related to 'superplasticity' or enhanced ductility.

In Chapter 3, the experimental methods used to carry out the present work will be addressed in detail, including sample preparation, mechanical testing equipment used, equations employed, as well as the testing conditions. The results obtained are presented in Chapter 4 and these in turn are discussed in Chapter 5. A summary of the major findings and the contributions to original knowledge are given in Chapters 6 and 7, respectively.

CHAPTER 2

LITERATURE SURVEY

2.1   Superplasticity

2.1.1   Introduction

Superplasticity refers to a material's ability to achieve high tensile ductilities (in excess of several hundred percent) at high temperatures and very low stress levels [12-15]. The elevated temperature deformation behavior of metals and alloys continues to draw scientific and commercial interest. Moreover, superplastic materials are typically characterized by a uniformity of flow and lack of necking. Consequently, this phenomenon has been extensively researched [6-11, 13, 15, 24-27, 30, 56-58]. Examples of superplasticity are given in Figure 2.1, where the ductility obtained was in excess of 1000%, and Figure 2.2.

Al-Mg-Sc T=475^{0}C

untested

$\dot{\varepsilon} = 1.38 \cdot 10^{-2} \, s^{-1}$ elong. = 1130%

12 mm
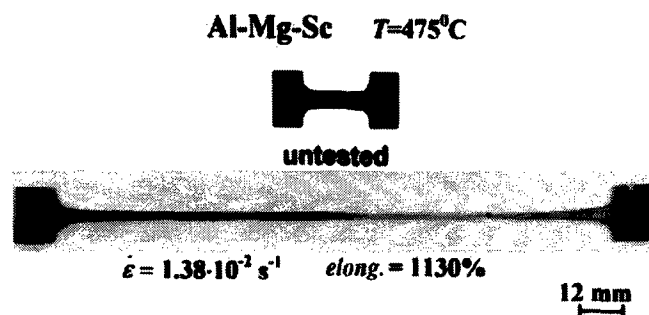
Figure 2.1.   Example of superplasticity for an Al 5XXX alloy [30].
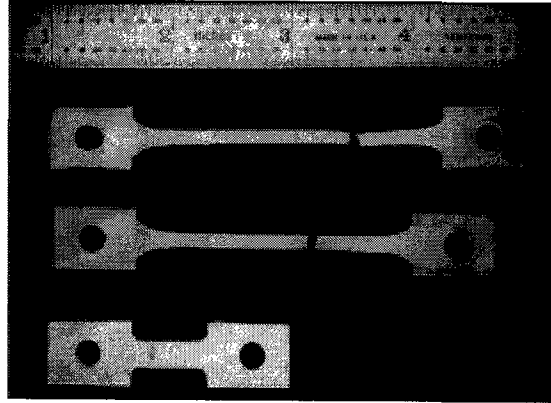
Figure 2.2. **Example of superplasticity for an Al 6XXX alloy showing deformations of 375% and 350% for the top and middle samples, respectively. as well as the original undeformed sample (bottom) [56].**

Aluminum 5XXX alloys are of particular interest in the automotive and aerospace industries as the presence of Mg ensures strength, good corrosion resistance, ductility, and formability [1-4]. However, improvements regarding their room temperature stretching performance are still required [4, 5]. According to Romhanji *et al.* [1], enhanced ductility can be achieved at elevated temperatures, especially, when the ductility approaches superplastic levels.

2.1.2   Fine-Grained Superplasticity vs. Coarse-Grained Enhanced Ductility

The stress (σ) – strain rate ($\dot{\varepsilon}$) relationship involved in superplastic deformation is analyzed based on the assumption of steady-state deformation during superplastic flow. The constitutive equation introduced by Backofen [12, 38, 59] for superplastic flow is given by

$$\sigma = \kappa \dot{\varepsilon}^{m} \qquad\qquad (2)$$

where 'σ' is the stress, '$\dot{\varepsilon}$' is the strain rate, 'κ' is a constant, and 'm' is the strain rate sensitivity exponent. Strain rate sensitivity can be thought of as the resistance to localized necking in the sample as it is being deformed; this resistance to necking is greatest in materials having high 'm' values, resulting in increased tensile elongations [60]. Coarse-grained materials should thus be able to experience enhanced ductility if a high value of 'm' is achieved [27].

Although superplastic materials, such as that shown in Figure 2.1, normally possess fine-grained structures (on the order of ~10μm or less) to facilitate grain boundary sliding, certain coarse-grained materials have recently been reported to exhibit higher than normal elongations [10, 11, 17, 18, 24-29] and this subject has therefore been addressed in the past [61-64]. Investigations into the superplastic deformation of coarse-grained materials have concluded, however, that grain boundary sliding is not the underlying mechanism for this phenomenon.

Enhanced tensile ductilities have been observed in several coarse-grained Al-Mg solid solution alloys [4, 10, 11, 17, 18, 28, 29, 61, 64]. Sherby and Wadsworth [58] have suggested that the behavior of coarse-grained alloys such as the Al-5%Mg-based alloys [11], which exhibit superplasticity, can be described by the so-called Class I solid solution creep, where the glide segment of the glide/climb dislocation process is the rate controlling element since solute atoms impede dislocation motion. Class I alloys are of interest under coarse-grained conditions at elevated temperatures since they demonstrate an intrinsically high 'm' value (~0.33) and have no grain size dependence [21, 58].

According to Nieh *et al.* [13, 57], as a result of solute drag, intragranular dislocation glide

has been recognized as the rate controlling process in Al-Mg alloys. Likewise, Taleff *et al.* [10,

18] concluded that solute-drag controlled or viscous-glide controlled creep behavior is the

prominent deformation mechanism responsible for an observed 'm' value of ~0.33, from their

work on the enhanced ductility of coarse-grained (30-140μm) Al-Mg alloys. Otsuka *et al.* [11]

have reported maximum elongations of ~330% and ~280% at 725 K in Al-5%Mg alloys having

mean grain sizes of ~40 μm to ~95 μm, and ~200 μm, respectively. Woo *et al.* [28] studied the

deformation of an Al-4Mg-0.4Sc alloy at 450°C with grain sizes varying from 67 μm to 100 μm.

Their results show that for a coarse grain size of 67μm, tensile elongations of nearly 170% were

obtained. These are given in Figure 2.3.
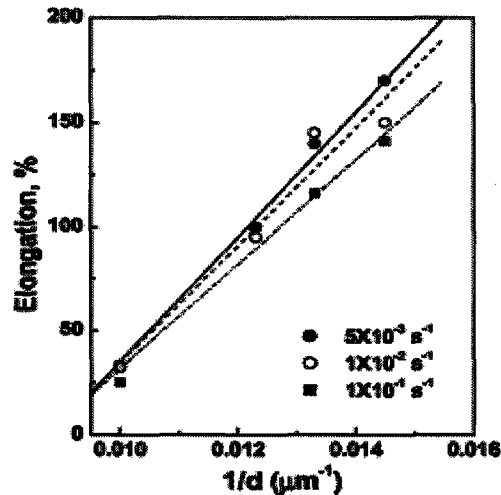
Figure 2.3.   Percent elongation as a function of (coarse) grain size in Al-4Mg-0.4Sc at 450°C [28].

Watanabe *et al.* [24] have also attributed the high ductility they observed in coarse-

grained materials to a glide-controlled dislocation creep/solute drag creep deformation

mechanism. Solute-drag creep leads to high values of 'm' and has no grain size dependence.

Therefore, as far as strain rate sensitivity is concerned, coarse-grained materials could potentially experience enhanced high temperature ductility, provided a high enough value of 'm' is achieved (usually $\geq$ 0.3) [10]. Woo *et al.* [17] suggested this as well for the enhanced ductility they observed in coarse-grained Al-Mg alloys, where peak ductilities of 270%, 350% and 240% were obtained for Al-5.3%Mg, Al-7%Mg and Al-11%Mg, respectively. The authors anticipated tensile elongations of ~200-300% at m = 0.3, based on the earlier work of Woodford [65].

From the work of Verma *et al.* [4] on superplasticity in a 5083 aluminum alloy in a two-step deformation sequence, it was observed that the ductility obtained in a fine-grained sample (d~9 μm) was nearly four times greater than in a coarse-grained sample (d~39 μm), as shown in Figure 2.4. Similar work was carried out by Wert on a 7475 Al alloy of varying grain sizes [66].
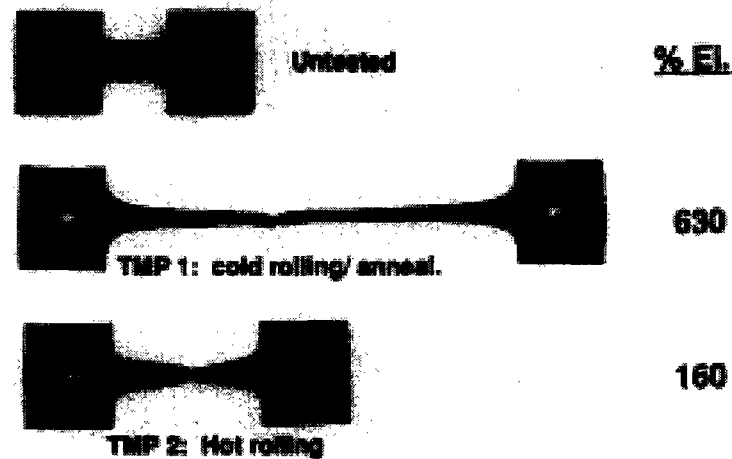
Figure 2.4.   **Superplasticity in 5083 aluminum alloy in a two-step deformation sequence (1.2×10^{-2} s^{-1} to a strain of 0.5, followed by 8×10^{-4} s^{-1} to failure); two samples were subjected to TMP's resulting in a fine-grained (9 μm; 630% elongation) and coarse-grained sample (39 μm; 160% elongation) [4].**

Therefore, although the exact mechanism responsible for coarse-grained superplasticity is still unclear, enhanced ductility leads to more modest elongations in coarse-grained materials than in fine-grained materials, where the value of 'm' is usually ≥ 0.3 [10, 11, 26, 58].

Despite demonstrating large "neck-free" elongations, many superplastic materials suffer from internal cavitation during deformation. This, in turn, imposes significant limitations on the industrial use of superplastically formed components. According to the work of Bae and Ghosh on superplasticity in Al-Mg alloys [67-69], general cavitation in superplastic metals occurs after an appreciable strain (i.e. ~ 0.2), where the emergence of cavities appears to be related to debonding along certain particle-matrix interfaces. Furthermore, they observed that the density of the cavities increased with strain, suggesting that the nucleation of cavitites by debonding is strain-controlled. Since coarse-grained materials exhibit moderate degrees of elongation when compared to the much higher elongations observed in fine-grained materials, cavitation takes on a more significant role in the premature necking and failure of coarse-grained samples.

2.2   Dynamic Strain Aging

2.2.1   Introduction

Dynamic strain aging (DSA) is a well-known phenomenon occurring in many alloys as a result of the interaction between solute atoms and moving dislocations *during* deformation [70-79], as opposed to static strain aging [80-82], where the solute-dislocation interactions occur *after* deformation. According to Morris and coworkers [31, 39-42], the stress vs. temperature curves of Al alloys experience a transient region due to dynamic strain aging, where the intensity

of strain aging increases with Mg content. Although DSA is known to bring about a loss in ductility [50], the flow stresses observed are greatly increased via the strengthening effect of the pinned dislocations [31]. Stress vs. temperature curves for Al-Mg alloys, where the transient region is the result of DSA, are shown in Figure 2.5.

2.2.2   Evidence of Jerky Flow

Curves a, b and c in Figure 2.5 correspond to the occurrence of significant, moderate and little DSA, respectively; the dashed line represents the stress vs. temperature curve for pure aluminum [31]. As the alloy is deformed, the dislocations will repeatedly break free from and be re-pinned by the solute atmospheres, resulting in serrated yielding or "jerky flow".
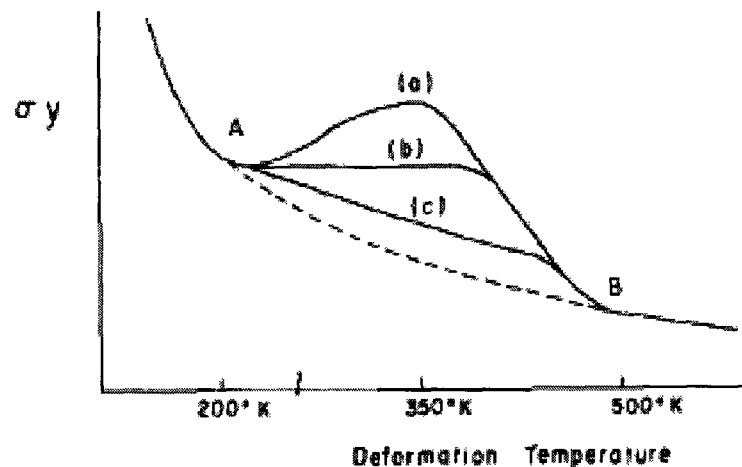
Figure 2.5.   Flow stress-deformation temperature curves for an Al-Mg alloy [31].

Visible evidence of jerky flow/load serrations associated with the DSA effect is related to the propagation of deformation bands and the formation of surface markings on the gage portion of the deformed samples [50, 70, 83-85]. The propagation of these serrations may occur in a continuous or discontinuous manner. An example of DSA serrations is given in Figure 2.6 for an

Al-3.5%Mg alloy. As can be seen, the photo on the top shows the initial bands that form. With

further straining, the sample gage length is entirely consumed in DSA bands, as shown in the

bottom photo.
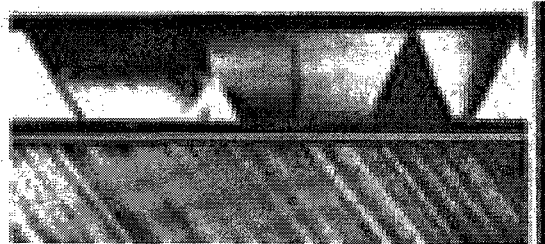
**Figure 2.6.   DSA serrations for an Al-3.5%Mg alloy after an initial amount (top) and
increased amount (bottom) of straining [88].**

The most important indication of DSA is that the strain rate sensitivity becomes negative

[38, 49, 86, 87] during the temperature interval where serrations occur. In other words, at a given

temperature and strain rate in the DSA regime, the deformed sample experiences a decreased

stress when the strain rate is increased. This is shown in the flow stress vs. temperature

schematic in Figure 2.7, where it is seen that, in the DSA regime (shaded), stresses are lower at

higher strain rates.
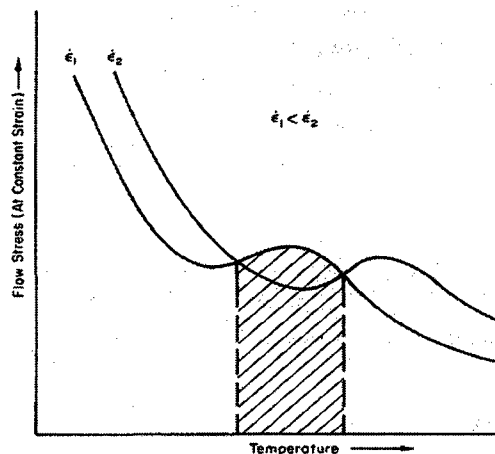
Figure 2.7.   Negative strain rate sensitivity region associated with DSA (shaded) [49].

Serrations occurring in this region are more pronounced at lower strain rates, given that there is more time allowed for the DSA reaction to take place when deforming to a given amount of strain as compared to deforming at a higher strain rate to the same desired strain (at a given temperature). Load serrations are indicative of the DSA phenomenon as well as the occurrence of negative strain rate sensitivity. Serrations will be further explored in Section 2.2.5.

2.2.3   Theories of Dynamic Strain Aging

The earliest DSA theories considered the interactions between solute and dislocations to occur during the free motion of the dislocations. Cottrell and Bilby [89] developed their theory of DSA in iron based on the segregation of carbon atoms to temporarily arrested dislocations. They proposed that at temperatures where the rate of solute diffusion is significant, the interaction between solute atoms and dislocations leads to solute segregation and pinning of mobile dislocations, forming the so-called "Cottrell atmosphere". Such a solute atmosphere exerts a drag force on moving dislocations, resulting in a necessary increase in the applied stress.

Conversely, when the dislocation breaks away from its solute atmosphere, the applied stress is lowered, until a new dislocation barrier is encountered. This sporadic increase and decrease in applied stress leads to serrated yielding, as evidenced by serrations in the load-displacement and stress-strain curves of the deformed material. Serrated yielding is also termed the Portevin LeChatelier (PLC) effect after Portevin and LeChatelier's work published in 1909.

More recently, it was proposed that solute-dislocation interactions occur when the mobile dislocations are temporarily arrested by obstacles in their path, such as forest dislocations. The

solutes segregate toward the relatively immobile dislocations and create a solute atmosphere, thus locking the dislocations. Van den Beukel [82, 90] and McCormick [32, 71, 86, 87], among others, modified the Cottrell-Bilby model to include the idea of solute saturation at the dislocations during this arrest or waiting time, t_w.

Van den Beukel suggested that DSA involves solute diffusion through the lattice and eventual clustering of solute atoms at the arrested dislocations forming a solute-dislocation lock as well as causing an increase in the lock strength. The amount of solute gathered at the dislocation depends on t_w, which itself depends on the strain rate and the average dislocation density. With an increase in the applied stress, the dislocation can break free from the solute cloud and this process is repeated for every period of arrest in dislocation motion.

2.2.4   Forces Involved in Dynamic Strain Aging

The various forces arising from dislocation motion during DSA have been investigated [91-93] and are summarized in Figure 2.8. This plot consists of curves 1 (lattice friction), 2 (solute drag force), 3 (force effect of the concentration of diffusing solutes) and 4 (the net result of the forces of curves 1-3). As can be seen, lattice friction forces and solute drag forces increase with increased dislocation velocity, while the effect of the concentration of the diffusing solutes near the dislocation varies inversely with dislocation velocity. The resultant behavior of a dislocation during DSA is given in curve 4.
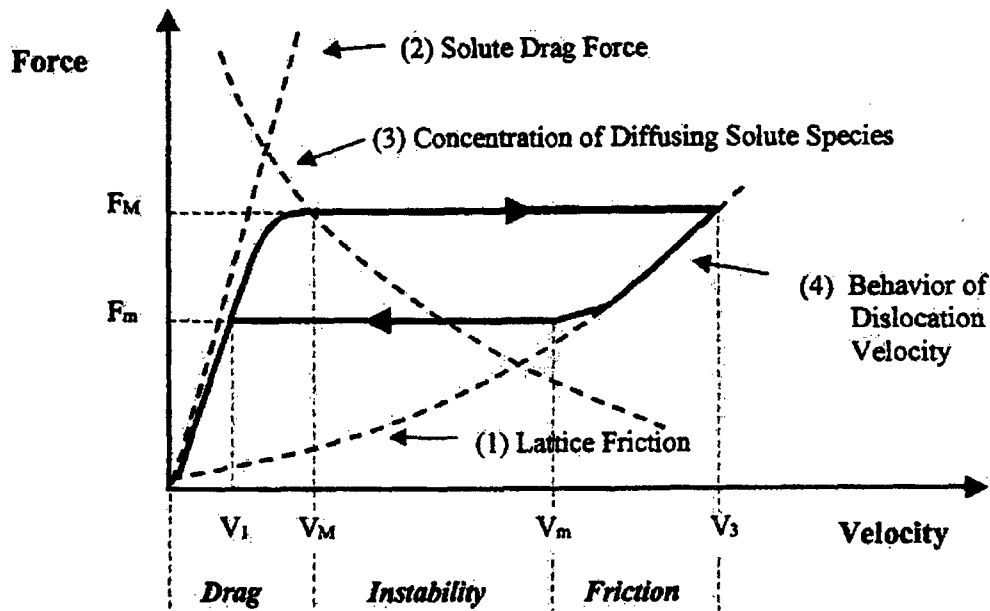
Figure 2.8.   Force vs. velocity diagram for a mobile dislocation during DSA [93].

At dislocation velocities less than V_M, the dislocation is in the drag regime. Here, the diffusing solute atoms have speeds comparable to the dislocation and can thus effectively form solute atmospheres. As the force and dislocation velocity increase, a critical force value (F_M) is attained and the dislocation enters the instability regime where the dislocation accelerates to where it can break away from the solute atmospheres.

With further increases in dislocation velocity, to V_3, lattice friction forces, including interactions with obstacles such as grain boundaries, precipitate particles and other dislocations, become dominant and the friction regime begins. By now, the dislocations lose speed until velocity V_m is reached, at which point dislocation motion is once again unstable. Consequently, the dislocation motion re-enters the drag regime at V_1 and the cycle is repeated, resulting in serrated yielding.

2.2.5   Dynamic Strain Aging Serration Types

Dynamic strain aging has been studied extensively [31-43] and the common serration

types are well-documented [84, 94-97]. Compared to interstitial systems, substitutional solid

solutions maintain serration types that are more readily identifiable. In substitutional solid

solution alloys, such as Al-Mg, the most recognizable serrations exist as Types A, B and C.

There also exist Types D and E, although there is less research covering them. Baird [96]

documents that the most common serration types (A, B and C) occur in face-centered cubic

metals containing substitutional solutes (e.g. Al-Mg alloys), based on the earlier work of

Brindley and Worthington [98]. These serrations are shown in Figure 2.9.
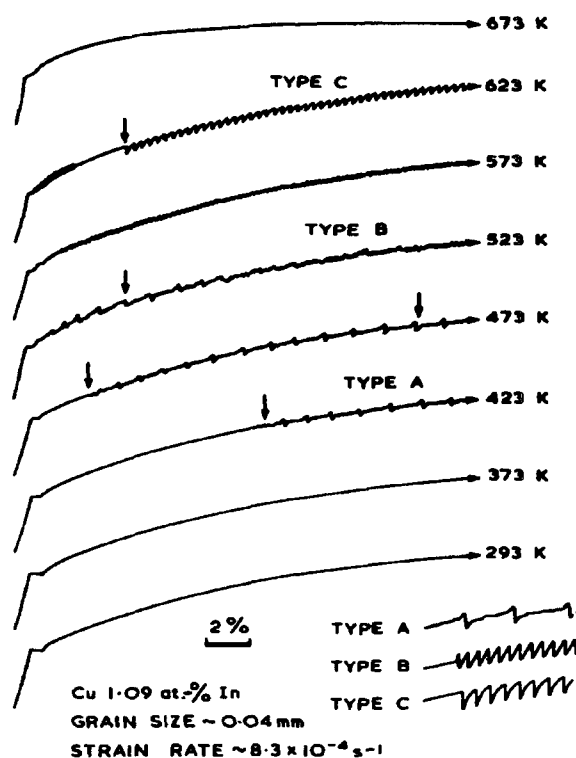
Figure 2.9.   **Stress-strain curves showing the appearance and disappearance of Type A, B and C serrations at increasing temperatures in a substitutional alloy system, based on the work of Brindley and Worthington [98] in a Cu-In alloy [96].**

Examples of Types D and E are given in Figure 2.10, following the work of Robinson and Shaw [97].
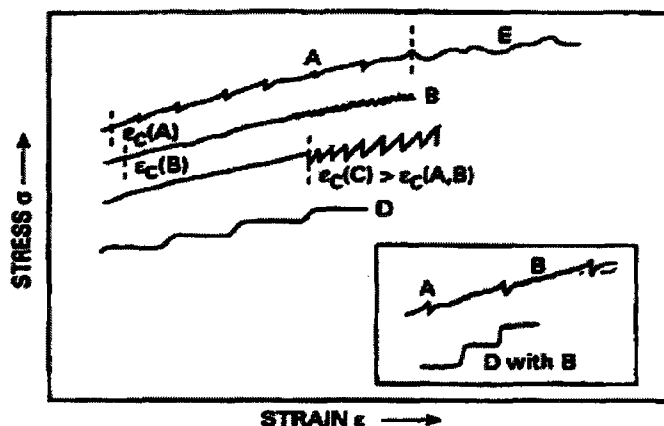
Figure 2.10. **Segments of stress-strain curves showing Type A-E serrations occurring in substitutional solid solution alloys [97].**

As can be seen from Figure 2.10, serration types can exist alone or can be manifested on a stress-strain curve as more than one type of serration. That is to say, that Type A, for example, will give way to Type B with increased strain, as shown at 523 K in Figure 2.9. Type A serrations, also known as 'locking serrations' are noted to occur in the low temperature/high strain rate portion of the DSA regime. Type B develops from Type A when the sample is taken to higher strains. They also occur at high temperatures and low strain rates. Type C serrations, or 'unlocking serrations', occur at higher temperatures and lower strain rates than Types A or B. Type D serrations resemble Type A, although with less work hardening taking place. Type E serrations also resemble Type A although only occurring at even higher strains. Stress-strain curves are not solely limited to one serration type at a time, especially at strains or temperature/strain rate conditions where a transition from one serration type to another occurs.

From the work of Li and Leslie [99], an example of the appearance and disappearance of serrations over the DSA domain (i.e. a finite temperature range for a given strain rate) in their work is given in Figure 2.11.
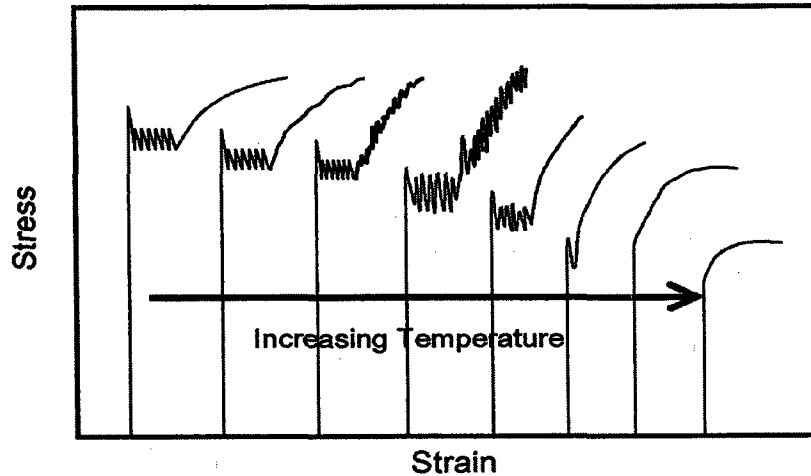
Figure 2.11. Stress-strain curves showing the appearance and disappearance of serrations with increasing temperature, for a given strain rate in the DSA domain for a given alloy [99].

As can be seen, dynamic strain aging is highly dependent on temperature and strain rate, since favorable combinations of temperature and strain rate will result in serrated yielding.

2.2.6   Temperature and Strain Rate Dependence of Dynamic Strain Aging

At very low temperatures, the solute atoms are too slow to catch up with dislocations during deformation. Conversely, when the temperature is too high, the solute atoms diffuse too quickly to exert any drag force on the dislocations. However, at intermediate temperatures, solute clouds can form around temporarily arrested dislocations. The diffusion coefficient of the solute

species varies exponentially with the inverse absolute temperature according to the following Arrhenius relation [74]:

$$D = D_0\exp[-Q_D/RT] \qquad (3)$$

where D_0 is the diffusivity of the solute, Q_D is the activation energy associated with diffusion of the solute, R is the gas constant and T is the absolute temperature. The diffusive mobility will thus increase rapidly with increasing temperature.

The DSA domain will move to higher temperatures with increasing strain rate since deformation is now at a higher rate, meaning that the dislocation velocity is increased and the arrest period is decreased. Consequently, the diffusive solute species must increase its mobility in order to effectively lock the dislocations. The onset of serrated yielding can be related to strain rate and temperature via another Arrhenius-type relation [74, 100, 101]:

$$\dot{\varepsilon} = A_f\exp[-Q/RT] \qquad (4)$$

where A_f is a frequency factor and Q is the activation energy for the either the onset or disappearance of serrations.

When Equation (4) is plotted in the form of the logarithm of strain rate vs. inverse absolute temperature, three distinct regimes become defined. These are illustrated in Figure 2.12.
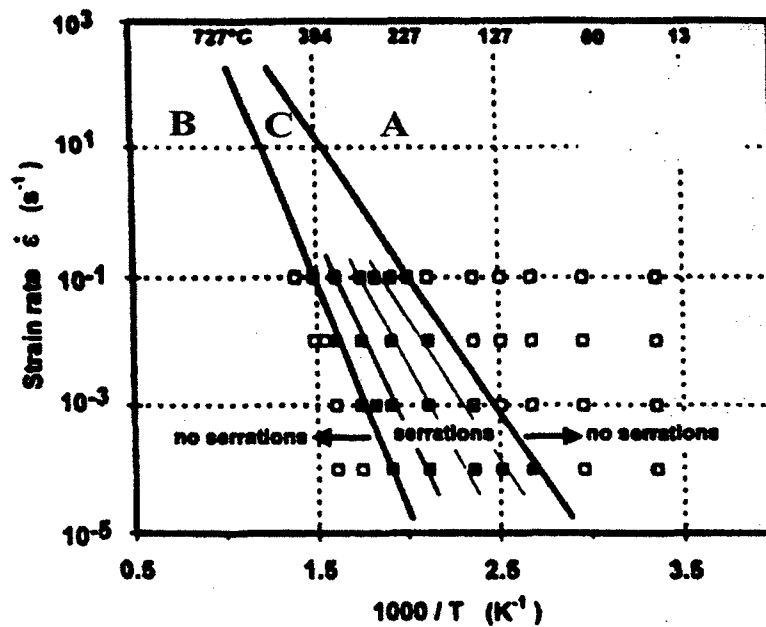
Figure 2.12. Strain rate vs. inverse temperature [74].

The two bold lines defining the DSA domain (i.e. area 'C' in Figure 2.12) represent the activation energies associated with the appearance and disappearance of serrations. The slope of the line separating the low and intermediate temperature regions represents the activation energy for the *onset* of serrations (when the temperature is increased). Similarly, the slope of the line separating the intermediate and high temperature regions represents the activation energy for the *disappearance* of serrations on further increases in temperature. Similar work has been carried out by Humphreys *et al.* [53], Pink and Grinberg [94], Romani *et al.* [102] and Picu *et al.* [103].

2.2.7   Critical Strain

Although DSA occurs at characteristic temperatures and strain rates, it has been shown that there exists a 'critical' strain (ε_c) required for the onset of serrated yielding in substitutional alloys [86, 90, 104-107]. As would be expected, this strain is sensitive to both temperature and

strain rate. The relationship between critical strain and strain rate for two different temperatures is demonstrated in Figure 2.13, where $T_2 > T_1$. It should be noted that under certain conditions of temperature and strain rate, serrations will begin immediately after yielding.
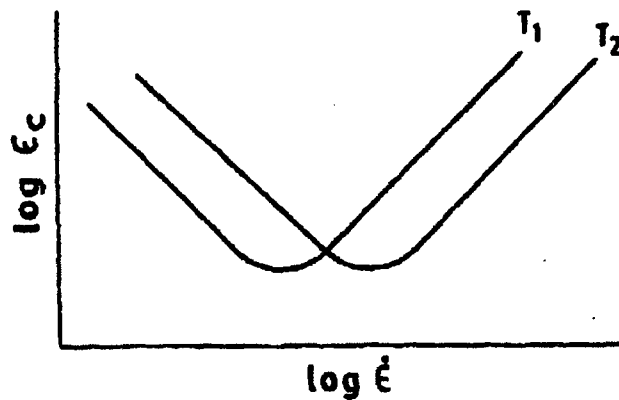
Figure 2.13. Critical strain (ε_c) vs. strain rate ($\dot{\varepsilon}$) for two given temperatures [97].

At low strain rates, the critical strain is seen to *decrease* with decreasing temperature and increasing strain rate. At high strain rates, the critical strain *increases* with decreasing temperature and increasing strain rate. At intermediate strain rates, the critical strain reaches a minimum and experiences very little change with temperature. According to Worthington and Brindley [108], the critical strain increases with increasing grain size. Therefore, coarser grained materials prone to DSA should experience higher critical strains than finer-grained materials, as greater strains are necessary to generate comparable dislocation densities.

2.2.8   Dynamic Strain Aging in Interstitial Alloys vs. Substitutional Alloys

Strain aging (static or dynamic) can be caused by interstitial solutes, substitutional solutes, or interstitial-substitutional complexes [109-111]. The bulk of research in this field has

been carried out on steels, where DSA is the result of interstitial carbon and nitrogen solute interactions with dislocations. As the mobility of interstitial solute species is also temperature-dependent, the manifestation of DSA serrations due to interstitial aging elements is readily observed in stress-strain curves in the DSA regime. There is also a higher probability of empty adjacent interstitial sites during deformation. The diffusion of substitutional aging species is dependent on the availability of vacancies to accommodate their larger atomic radii, in addition to temperature. The diffusion coefficient of substitutional solutes can be written as [109]:

$$D \propto C_V \exp[-Q_{SV}/kT] \qquad (5)$$

where C_V is the vacancy concentration, k is the Boltzmann constant and Q_{sv} is the activation energy associated with site exchange between substitutional solutes and vacancies. Due to this stronger dependence on vacancy concentration for diffusive *substitutional* elements over interstitial solutes, substitutional solute diffusion is considerably slower than interstitial solute diffusion.

Substitutional diffusion in steel is too slow to produce any noticeable strain-aging effects in the temperature range (100°C to 400°C) in which interstitial strain aging has been observed [109, 110]. In order for substitutional elements to achieve diffusion coefficients similar to those of carbon and nitrogen at 250°C, the temperature must exceed 900°C for phosphorus and 1400°C for chromium and nickel. Conversely, at such high temperatures, the interstitial elements diffuse too rapidly to exert any significant drag force on mobile dislocations and, in turn, produce no notable strain aging effects in this temperature range [109].

2.2.9   Strain Rate Sensitivity as a Result of Dynamic Strain Aging

Barnett and Jonas [51, 52] have shown that DSA alters the rate sensitivity of the material, which in turn affects the ease with which rapid flow localization, i.e. shear banding, can occur. Since shear bands involve localized flow, they are therefore sensitive to the deformation temperature, rate sensitivity, and work hardening rate [51-55]. In their work on low carbon steels, it was shown that the flow stress vs. temperature behavior of a steel prone to DSA exhibits a 'hump' in the temperature range where the DSA phenomenon occurs. In other words, for a given strain rate, the flow stress will increase to a local maximum and then eventually decrease with increasing temperature in the DSA regime. This is shown in Figure 2.14.
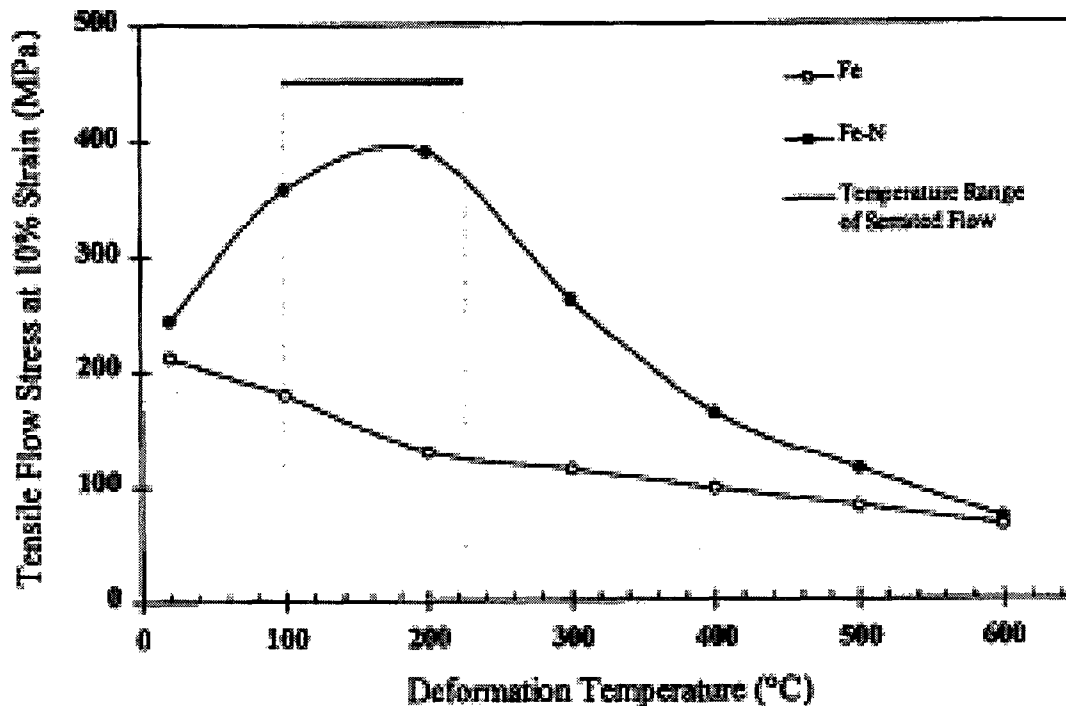
Figure 2.14.   Flow stress vs. temperature curves for an interstitial free iron compared to an iron containing 0.005% nitrogen. A 'hump' is noted to form where serrated flow/DSA occurs [52].

It was further observed that increasing the strain rate shifts the stress vs. temperature curve to higher temperatures (Figure 2.15). This increase in strain rate creates two distinct areas in Figure 2.15: a region of negative strain rate sensitivity at lower temperatures and a region of abnormally high strain rate sensitivity at higher temperatures.
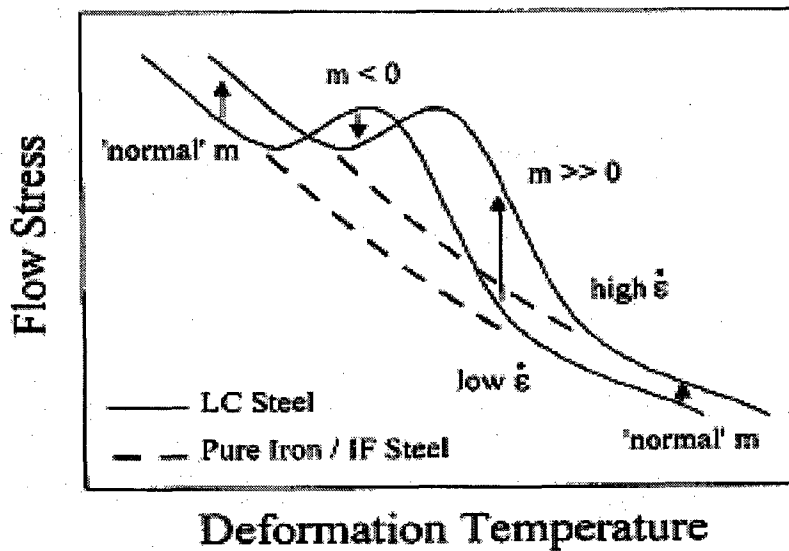
Figure 2.15. Flow stress vs. temperature curves for a low carbon (LC) steel which exhibits DSA vs. interstitial free (IF) steel which softens with temperature [55].

Therefore, an increase in strain rate directly affects the rate sensitivity in the presence of a DSA peak. Moreover, it is seen that a pure metal (i.e. free of solute elements and not subject to DSA) will soften gradually with increasing temperature and demonstrate a small positive strain rate sensitivity, whereas an alloy exhibiting DSA will experience an increase in strength during the DSA regime until a peak is reached. Following this, the stress felt by the alloy decreases and eventually meets up with the pure metal behavior.

For the two given strain rates of Figure 2.14 ($\dot{\varepsilon}_2 > \dot{\varepsilon}_1$) and the corresponding flow stresses (where σ_2 corresponds to $\dot{\varepsilon}_2$ and σ_1 corresponds to $\dot{\varepsilon}_1$), Equation (2) becomes:

$$m = \frac{(\ln \sigma_2 - \ln \sigma_1)}{(\ln \dot{\varepsilon}_2 - \ln \dot{\varepsilon}_1)} \qquad (6)$$

where 'm' increases with increasing strain rate. At high values of 'm', uniform deformation is promoted by delaying the onset of necking; high values of 'm' also inhibit the development of strain localizations. However, when a local increase in strain rate can no longer be counteracted by the stabilizing effect of the rate sensitivity, then the material stands to suffer a loss in ductility [70]. If the rate sensitivity is small and positive, then the tendency for strain localization will be enhanced. Liu et. al. [54] noted that moderate shear band formation corresponded to small positive rate sensitivity values, while intense shear band formation was observed for negative rate sensitivity values, since negative rate sensitivities enhance the formation of flow localizations [55].

For negative values of rate sensitivity, an alloy will be able to deform at increasing strain rates under decreasing stresses [70], yet the overall ductility is still limited compared to deformation at temperatures *outside* the negative rate sensitivity region and *in* the high rate sensitivity region. Barnett and Jonas [52] observed a local increase in the rate sensitivity vs. temperature behavior in their work as a result of having obtained a high 'm' value with increasing temperature out of the DSA regime. This high local 'm' is coupled with the negative 'm' characteristic of DSA. These observations are illustrated in Figure 2.16.
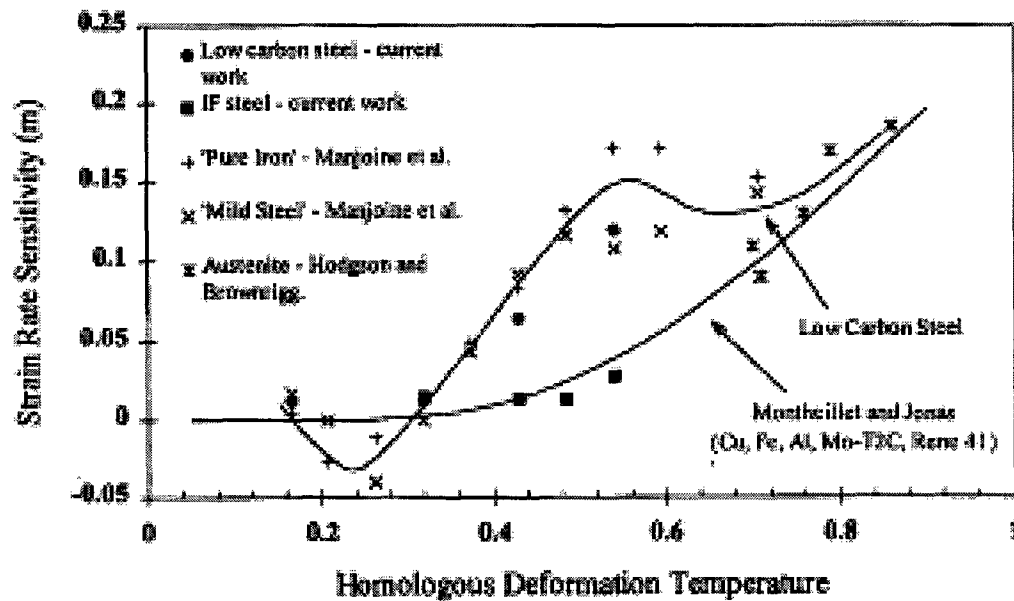
Figure 2.16. Strain rate sensitivity vs. homologous temperature plots from various researchers [52].

Humphreys *et al.* [53] also observed a local increase in the rate sensitivity vs. temperature behavior in their work. This was also attributed to the result of having obtained a high 'm' value with increasing temperatures out of the DSA regime. Moreoever, the high local 'm' region was coupled with a negative 'm' region, a characteristic of DSA. These observations are illustrated in Figure 2.18. The flow stress vs. deformation temperature behavior observed by Humphreys *et. al.* [53] leading to the results shown in Figure 2.18 is given in Figure 2.17.
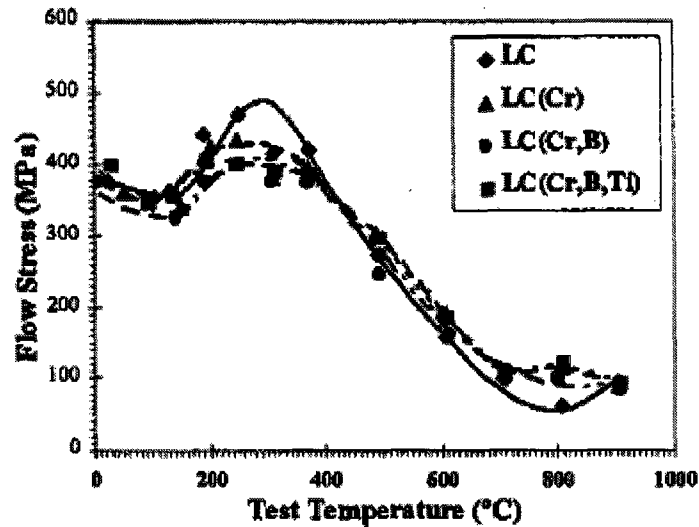
Figure 2.17. Flow stress vs. temperature curves for a low carbon (LC) steel prone to DSA vs. interstitial free (IF) steel for a mean strain rate of 10^{-2} s^{-1} [53].
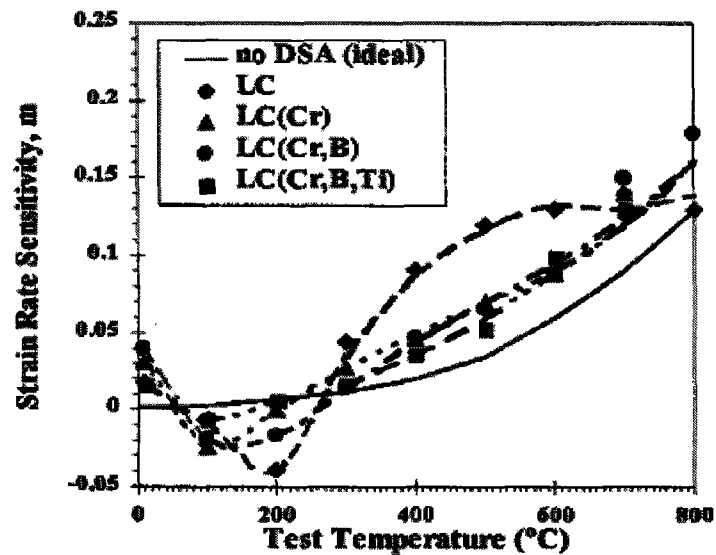
Figure 2.18. Strain rate sensitivity vs. temperature for a low carbon (LC) steel prone to DSA vs. interstitial free (IF) steel for a mean strain rate of 10^{-2} s^{-1} [53].

As can be seen from Figure 2.18, the strain rate sensitivity reaches an abnormally large local peak at temperatures outside the serration range. The negative strain rate sensitivity regime is coupled with this high strain rate sensitivity regime. It should also be pointed out that this local

peak occurs at a temperature less than the maximum test temperature. An extension of this work was done by Romani *et al.* [102] and is shown in Figure 2.19.
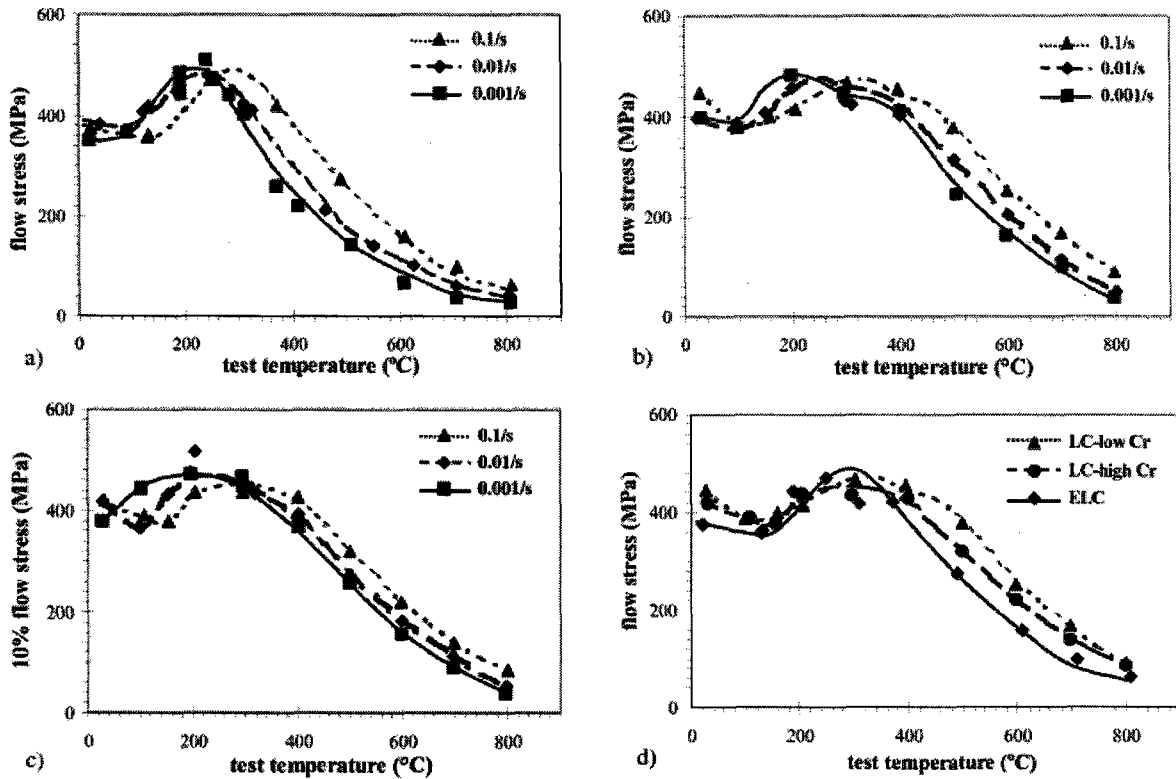
Figure 2.19.   Stress vs. temperature curves for (a) ELC, (b) LC with low Cr content, (c) LC with high Cr content and (d) all steels at a mean strain rate of 10^{-3} s^{-1} [102].

As can be seen from Figure 2.19(a) to (c), the stress-temperature curves shift to higher temperatures with increased strain rates similar to that given in Figure 2.17. Moreover, the effect of chemical composition on the resulting 'humped' stress-temperature curve is shown in Figure 2.19(d), at a mean strain rate of 10^{-3} s^{-1}.

Therefore, the 'hump' effect in the flow stress vs. temperature behavior of an alloy due to DSA leads to an abnormal increase in the strain rate sensitivity (coupled with the negative rate sensitivity that is ordinarily expected of materials subject to DSA) in the form of a local maximum in 'm' value. With still higher temperatures, the rate sensitivity returns to normal. This local increase in rate sensitivity results in enhanced elongation at the given temperature/mean strain rate combination at which the maximum 'm' occurs. If the rate sensitivity is high enough, then enhanced ductility in coarse-grained materials is possible. This, as mentioned before, eliminates the fine-grained structure restriction. The aim of this work was to test for enhanced ductility in coarse-grained Al-Mg alloys (i.e. a substitutional solid solution) in the vicinity of the maximum 'm' in order to overcome the need for a fine-grained structure and still obtain larger than normal values of ductility.

CHAPTER 3

MATERIALS AND METHODS

Three Al-Mg alloys were selected for this investigation: super-pure Al-3%Mg, super-pure Al-5%Mg, and commercial 5056 aluminum alloy. A further material, commercial purity aluminum, was used as a reference. The compositions of these materials are given in Table 3.1. These materials were prepared at Novelis in Kingston, Ontario and supplied in the form of 1 mm-thick rolled and annealed sheets.

Table 3.1   Chemical Compositions of the Test Materials (wt%)

Material	Mg	Cr	Fe	Mn	Si	Al
Al-3%Mg	2.77	0.001	0.005	0.002	0.007	Balance
Al-5%Mg	5.12	0.001	0.006	0.001	0.003	Balance
AA 5056	4.68	0.13	0.042	0.091	0.037	Balance
C.P. Al	-----	------	0.06	------	0.05	Balance

3.1   Preparation of Samples for Tensile Testing

From the rolled and annealed received sheets, tensile specimens were machined according to the ASTM E8M standard, as shown in Figure 3.1. Here, the typical sample gage length is 25 mm with a cross-sectional area of 6mm by 1mm. The samples were solution heat-

treated in air for 8 hours at 450°C in a Lindberg/Blue Box Furnace-type electric resistance furnace, water quenched and then immediately stored in a freezer until testing. Prior to testing, the samples were fine-ground using 800 and 1200-grit grinding paper. Papers of a lower grit (i.e. 600 and lower) were avoided so as not to induce any scratches on the material surface.
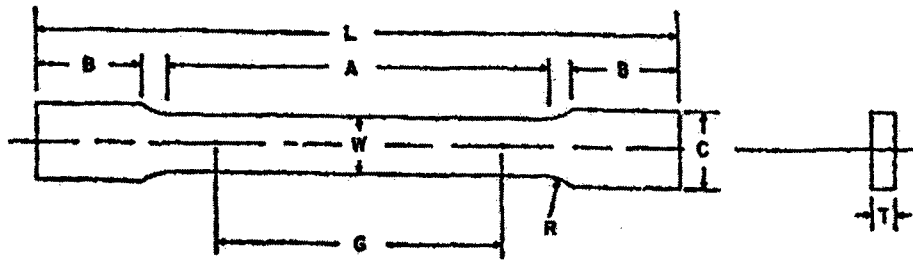
Figure 3.1. ASTM E8M specimen for flat-sheet tensile samples.

3.2   Uniaxial Tensile Tests to 10% Strain

The flow stress vs. temperature behavior of these alloys was studied by means of tensile tests carried out to 10% strain. Tension tests were conducted to a fixed strain of 0.1 in the temperature range of -75°C-450°C and using strain rates of $10^{-1}s^{-1}$, $10^{-2}s^{-1}$ and $10^{-3}s^{-1}$.

Tests from room to high temperature were performed using a Model 510 Servohydraulic MTS mechanical testing machine, as shown in Figure 3.2, at McGill University. The MTS machine consists of a 100 kN load frame, a hydraulic power supply, a servohydraulic valve system and a 1000 lb-f (5000 N) capacity load cell. Axial displacement is recorded via a linear variable differential transformer (LVDT) connected to a data acquisition system.

All tests are controlled by a TestStar II M computer, programmed and interfaced through MTS Model 793 software, which enables the data acquisition. Temperature is controlled by a 16-kW radiant furnace heated by four equally-spaced incandescent tungsten lamps, where the radiation is focused on the central axis of the furnace by four elliptical aluminum reflectors. The furnace, in turn, is controlled by a Micristar temperature controller connected to a closed-tip K-type thermocouple and is water cooled.
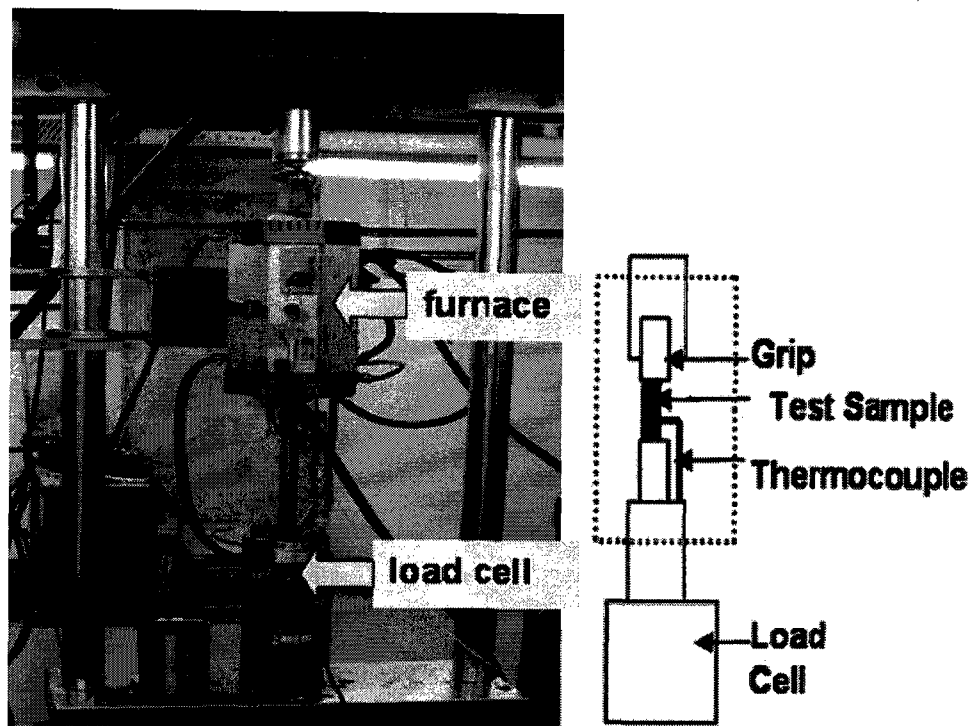
Figure 3.2.   MTS 100 kN tension/compression frame.

Tensile tests below room temperature were performed using a similar MTS servohydraulic machine with an environmental chamber cooled down by spraying liquid nitrogen. Test temperature was controlled to +/- 2°C at the CANMET-MTL laboratories in Ottawa, ON.

3.3   Uniaxial Tensile Tests to Failure (Enhanced Ductility Tests)

The enhanced ductility of these alloys was monitored by means of tensile tests to failure using shortened tensile specimens machined according to the ASTM E2448-06 standard, as shown in Figure 3.3.
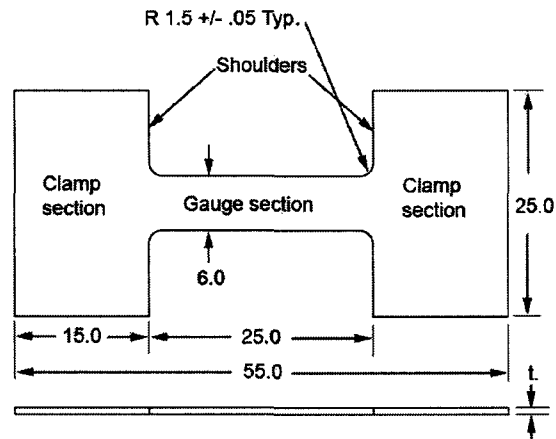
Figure 3.3.   E2448-06 specimen for flat-sheet superplasticity tensile samples.

These samples were solution heat-treated in air in a horizontally positioned 16-kW radiant furnace similar to that mentioned in the previous section. It should be noted that these samples were pulled to failure and scribed gage marks were used to measure the resulting ductility. These scribed gage marks were used in accordance with ASTM guidelines and the final elongation was recorded as the difference between the final and initial gage lengths, divided by the initial gage length.

It has occurred in the literature that some researchers have taken the final length and divided this value by the initial length, which yields a ratio of final to initial length and, in turn, results in an additional 100% in elongation. For example, "280%" elongation in the literature

may, depending on how the final sample length was measured, only equal "180%" in the present work. Likewise, "280%" in the present work could correspond to "380%" elongation in the literature. It has generally been observed that ductility values in the range of 200-300% are acceptable for superplasticity or 'enhanced ductility' in coarse-grained materials.

Moreover, to minimize sample surface oxidation and maximize the testing temperature range, the samples were solution heat treated for 2 hours at 560°C in an argon atmosphere. These samples were then quenched in water and immediately stored in a freezer to maintain the Mg in solid solution. Tensile tests were performed in the temperature range -75°C - 450°C and using strain rates of $5 \times 10^{-3} s^{-1}$.

3.4   Test Conditions

Tensile tests were carried out to a fixed strain of 0.1 to allow for serrations to develop in the DSA range. The test temperature range used was -75°C - 450°C and the prescribed strain rates were $10^{-1} s^{-1}$, $10^{-2} s^{-1}$ and $10^{-3} s^{-1}$. Following deformation, the flow stress at a given temperature and strain rate was recorded at 10% strain in order to acquire the flow stress vs. deformation temperature curves and determine the associated strain rate sensitivities. Three to five tensile tests were performed at each temperature so as to generate reproducible data and better define the 'hump' portion of each curve, which signifies the occurrence of DSA. For the superplasticity tests, the LVDT was dismantled and the shortened tensile specimens were used.

3.5   Metallographic Examination

To determine the grain size, specimens for metallography were sectioned from the sheet materials for examination in the as-received condition as well as after solution heat treatment. The specimens were mounted in bakelite, polished, and subsequently etched in a reagent composed of 0.5%HF acid in water. The etched samples were then examined using an Olympus optical microscope linked to a Clemex image analysis system to determine the grain size and shape prior to plastic deformation. Figure 3.4 shows the optical microscope-image analyzer set-up that was used for this purpose. Several micrographs were taken for each sample and the line-intercept method was employed to determine the average grain size.
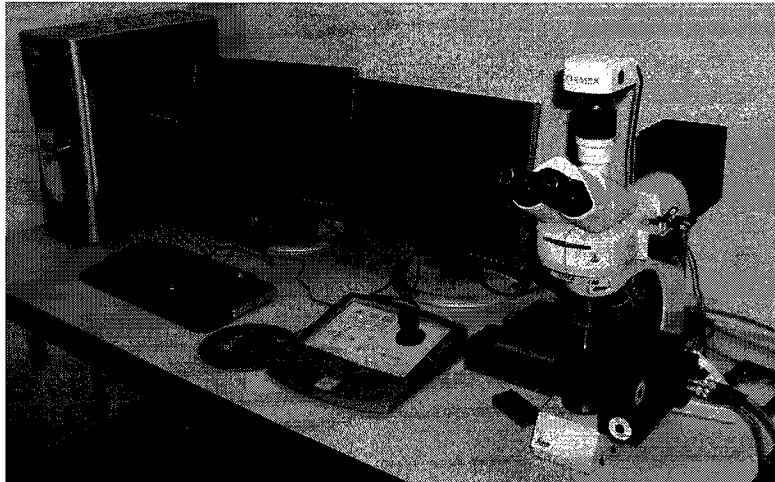
Figure 3.4.   Optical microscope - Clemex image analyzer system.

In order to determine whether the samples used for the superplasticity tests were oxidized and to what extent, electron probe microanalysis (EPMA) was employed to determine the Mg content across the width of the sample. This was required because the samples had been annealed in air and any loss of Mg would affect the solute-dislocation interaction expected to take place

during dynamic strain aging. For this, line scans were carried out across the gage widths of various alloy samples to measure the Mg content from edge to edge. Readings of the Mg concentration (wt%) were taken at 3µm intervals, first to avoid overlapping of the analyzed zones, and second, to obtain a continuous scan along the path selected. Figure 3.5 shows the JEOL JXA-89001 WD/RD combined microanalyzer that was used for these measurements. The operating conditions were 20 kV and 30 nA, using an electron beam size ~1µm in diameter.
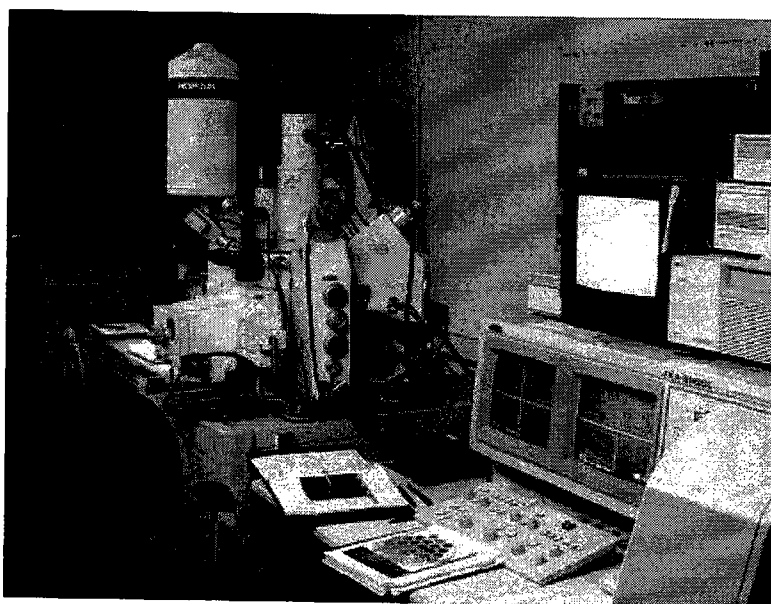
Figure 3.5.   The JEOL JXA-8900L electron probe microanalyzer.

CHAPTER 4

RESULTS

This section is divided into two major sections with corresponding subsections. The first major section accounts for the tensile tests carried out to 10% strain in order to observe any DSA activity in the form of serrated yielding. Here, the stress-temperature behavior of the alloys tested is compared with that of commercially pure aluminum to further emphasize the DSA activity observed. The serrated stress-strain curves are plotted for a given strain rate - in a given alloy - and are shifted by appropriate amounts of stress for clarity. The second major section demonstrates the enhanced ductilities observed in the materials tested.

4.1   Tensile Tests to 10% Strain

4.1.1   Introduction

Tensile tests were carried out to 10% strain. The samples were machined according to the ASTM E8M standard, as described in Chapter 3, and an LVDT was attached to the gage portion. All test data were recorded as load vs. displacement. This information was then converted into engineering stress vs. engineering strain data. Knowing that serrations begin to form at either a given critical strain or almost immediately after yielding, a strain of 10% was arbitrarily chosen to allow serrations to be seen on a stress vs. strain curve. If no serrations are observed at low

temperatures, it is anticipated that one is in the 'no serrations' region of Figure 2.9. Although

serrations *could* form at strains greater than 10%, given the temperature and strain rate

combination selected, 10% strain was the 'cutoff' employed.

The primary variables of interest are temperature and strain rate. The results are presented

in terms of increasing temperature at a given strain rate, for a given alloy. Serration intensity is

seen to increase with increasing temperature in the DSA regime before eventually disappearing.

A visible example of the DSA serrations obtained in this study is shown in Figure 4.1.
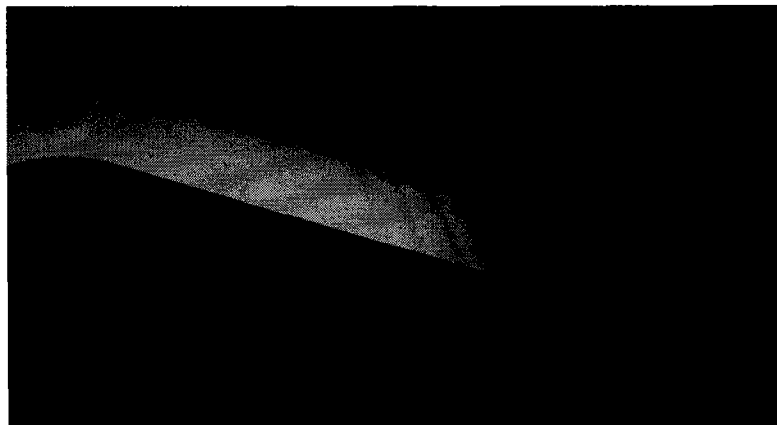
Figure 4.1.   Example of the dynamic strain aging markings observed across the Al-
5%Mg tensile sample at room temperature and a strain rate of 10^{-3} s^{-1}.

Also, knowing from the literature that the DSA phenomenon occurs in Al-Mg alloys at

low temperatures, the alloy tensile samples were solution heat treated for 8 hours at 450°C,

quenched, and then refrigerated to ensure that the Mg rests in solution. Coarse grain sizes of

~130 μm, ~145 μm and ~15 μm were observed in the Al-3%Mg, Al-5%Mg and AA 5056 alloys,

respectively, following the solution heat treatment. Examples are given in Figures 4.2 and 4.3.
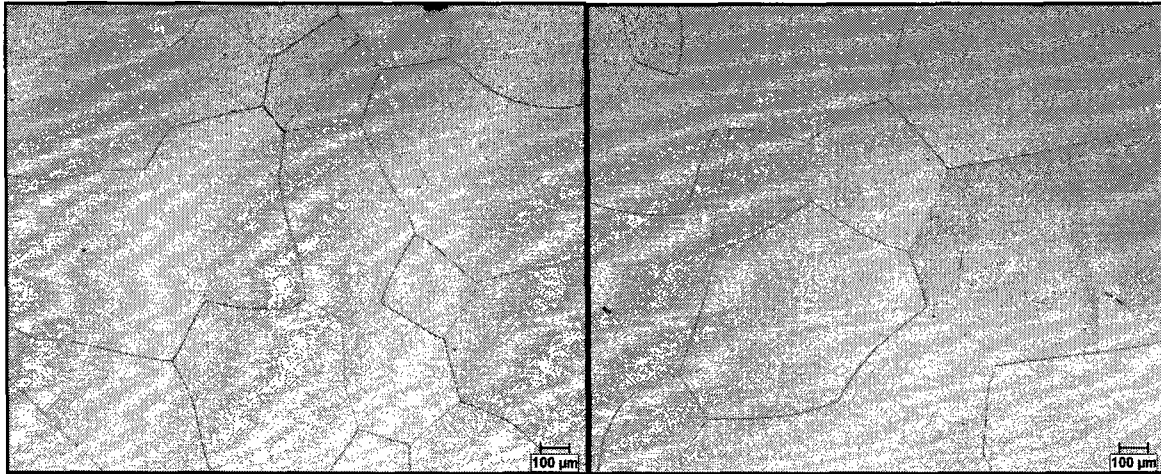
Figure 4.2.   Grain sizes for Al-3%Mg (left) and Al-5%Mg (right) after a solution heat-treatment of 8 hours at 450°C (i.e. before testing), taken at 50X.
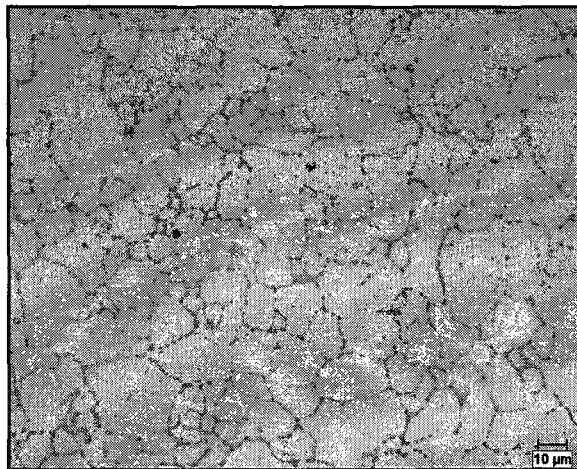
Figure 4.3.   Grain size for AA 5056 after solution heat-treatment of 8 hours at 450°C (i.e. before testing), taken at 500X.

The Mg content in the alloys is another variable of interest seeing as how the interaction between the Mg and the dislocations during deformation is responsible for the DSA phenomenon. It should be made clear that the serrated stress-strain curves presented in the following sections have been shifted by an appropriate amount of stress (MPa) so that they can be seen clearly.

4.1.2   Stress vs. Strain – Al-3%Mg, $\dot{\varepsilon} = 10^{-3}\,s^{-1}$

The stress vs. temperature curve obtained for Al-3%Mg vs. that for commercially pure Al

at $\dot{\varepsilon} = 10^{-3}\,s^{-1}$ is displayed in Figure 4.4.
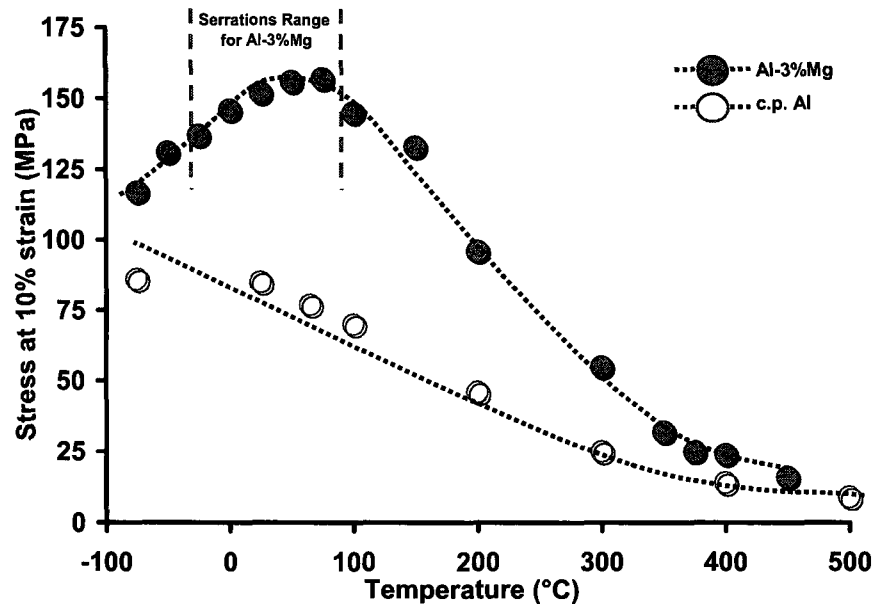
Figure 4.4.   Stress vs. temperature curve for Al-3%Mg at $\dot{\varepsilon} = 10^{-3}\,s^{-1}$.

The stress values plotted in the following figures were recorded at an engineering strain

of 0.1 to allow enough deformation to occur to ensure serration formation in the DSA regime. As

can be seen in Figure 4.4, a 'hump' occurs at lower temperatures, which reaches a peak at 50°C

and eventually decreases with increasing temperature.

Samples tested at temperatures within the DSA 'hump' exhibited serrations which

increased in intensity with increasing temperature. The lowest temperature tested was -75°C. It is

anticipated that tensile tests below -75°C would result in the stress increasing with decreasing

temperature, as in Figure 2.5. Moreover, it is seen that commercially pure aluminum decreases monotonically with increasing temperature, thus further emphasizing the 'hump' formed in the Al-3%Mg alloy. No serrations occur in the commercially pure Al. The actual stress vs. strain curves obtained for Al-3%Mg during the DSA regime at $\dot{\varepsilon} = 10^{-3}$ s^{-1} are presented in Figure 4.5.

Figure 4.5.   Stress vs. strain curves for Al-3%Mg at $\dot{\varepsilon} = 10^{-3}$ s^{-1}.

It is seen that at -75°C, the stress vs. strain curve is smooth with no indication of DSA serrations. Knowing that serrations occur at room temperature in Al-Mg alloys, it is anticipated that at -75°C, one is in the low temperature/'no serration' regime of Figure 2.12, just prior to the formation of the DSA 'hump' shown in Figure 2.15. The stress vs. strain curve at -50°C is also smooth with no indication of DSA serrations. It is possible that serrations form at this temperature but are delayed, i.e. the critical strain is greater than 10%. Likewise, it is possible

that serrations form at -75°C but are delayed beyond a strain of 10%. Moreover, -75°C lies at the beginning of the 'hump' formed in Figure 4.4. Keeping in mind that stress is being considered at 10% strain, delayed serrations (i.e. at $\varepsilon > 0.1$) will not be accounted for. It is expected that serrations occur in Al-Mg alloys at room temperature almost immediately after yielding.

Step-like serrations are noted to form at -25°C at $\varepsilon \sim 0.05$ and become more persistent at 0°C as well as begin to appear at a lower value of critical strain (~ 0.01). With still higher temperatures, such as 25°C, these serrations occur much more frequently and almost immediately after yielding. This is expected since DSA is known to occur in Al-Mg alloys at room temperature.

The serrations formed at 50°C and 75°C are seen to form almost immediately after yielding; moreover, the serration intensity increases with increasing temperature. With a still higher increase in temperature to 100°C, there is no indication of DSA serrations and the curve obtained is smooth. Note the occurrence of "traveling bands" [103] at 75°C from a strain of ~ 0.03 to ~ 0.06.

4.1.3   Stress vs. Strain – Al-3%Mg, $\dot{\varepsilon} = 10^{-2}$ s^{-1}

The stress vs. temperature curve obtained for Al-3%Mg vs. that for commercially pure Al at $\dot{\varepsilon} = 10^{-2}$ s^{-1} is displayed in Figure 4.6. As with the tensile tests performed at $\dot{\varepsilon} = 10^{-3}$ s^{-1}, the load-displacement information was converted into engineering stress vs. engineering strain. The stress values plotted in the following figures were recorded at a strain of 0.1 to allow enough deformation to occur to ensure serration formation in the DSA regime.
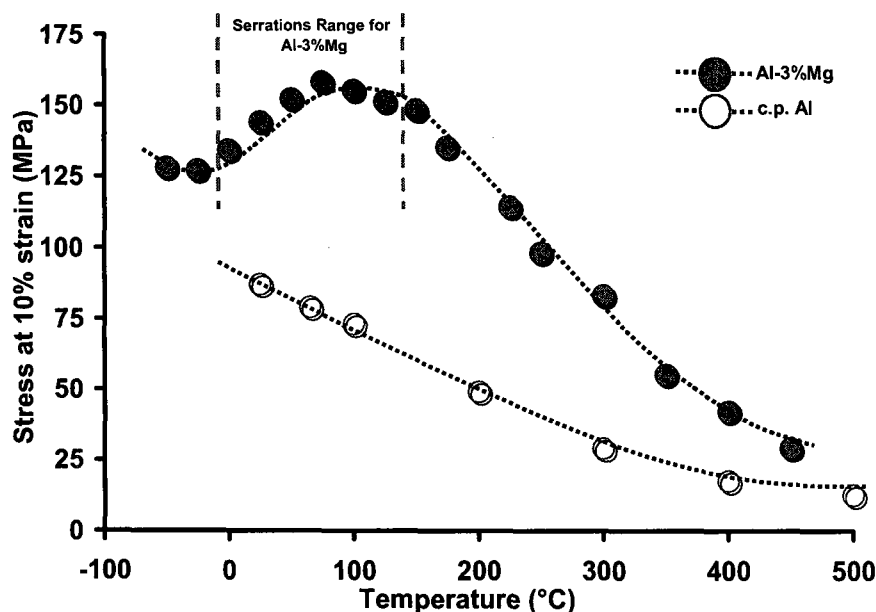
Figure 4.6.   Stress vs. temperature curve for Al-3%Mg at $\dot{\varepsilon} = 10^{-2}\ s^{-1}$.

As with Figure 4.4, Figure 4.6 also displays a 'hump' at lower temperatures, which reaches a peak at ~75°-100°C and then begins to decrease with increasing temperature. The 'hump' is better defined here than in Figure 4.4, demonstrating that the stress-temperature profile shifts to higher temperatures with increasing strain rate. As well, the "DSA-free" commercially pure Al shifts to higher temperatures with increasing strain rate.

Overlapping the curves of Figures 4.9 and 4.6 would result in a negative strain rate sensitivity region at lower temperatures and, more importantly, a region of abnormally high strain rate sensitivity at higher temperatures. It is again anticipated that tensile tests below -75°C would result in the stress increasing with decreasing temperature. Moreover, the curves corresponding to the temperature points tested within the DSA 'hump' exhibited serrations that increased in intensity with increase in the temperature of testing. The stress vs. strain curves obtained for Al-3%Mg during the DSA regime at $\dot{\varepsilon} = 10^{-2}\ s^{-1}$ are presented in Figure 4.7.
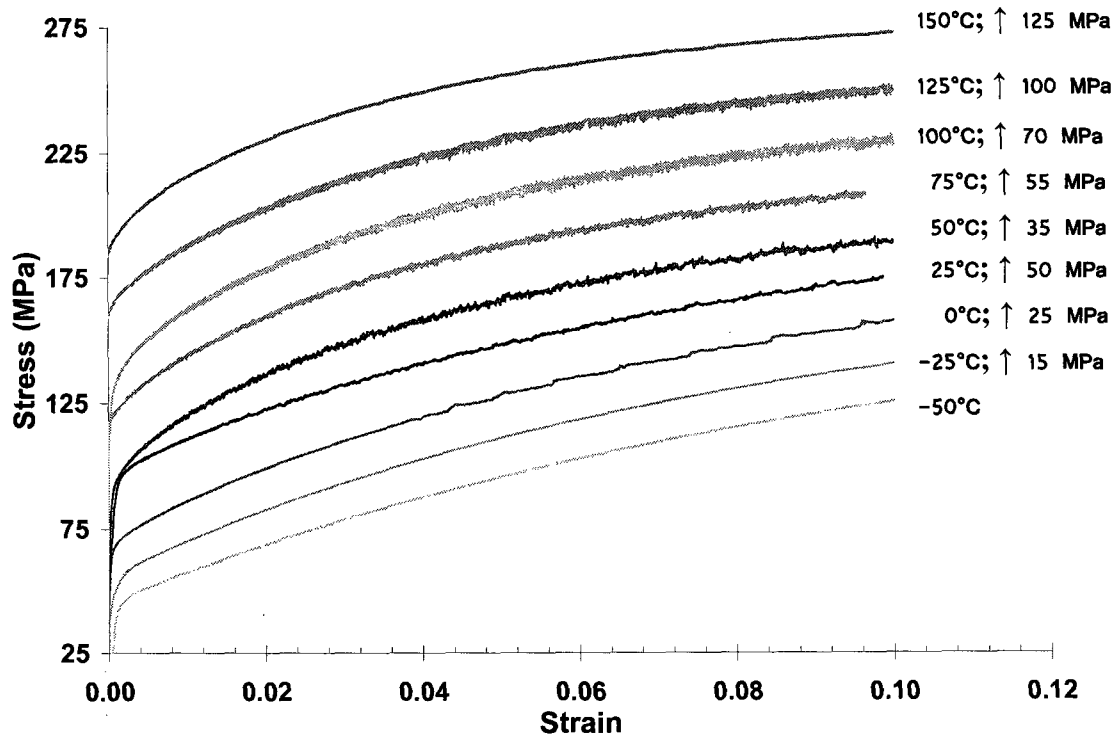
Figure 4.7. **Stress vs. strain curves for Al-3%Mg at** $\dot{\varepsilon} = 10^{-2}$ **s**$^{-1}$.

As can be seen, the curves taken at -50°C and -25°C are smooth with no indication of DSA serrations. This implies that one is in the low temperature/'no serration' regime, just prior to the formation of the DSA 'hump'. However, with increasing temperature, serrations slowly begin to manifest themselves.

The stress vs. strain curve at 0°C is characterized by step-like serrations, which are noted to form at $\varepsilon \sim 0.035$. These serrations become more persistent at higher temperatures and also begin at a lower value of critical strain (~ 0.014 at 25°C) and appear much more frequently. The serrations corresponding to the stress vs. strain curves at 50°C, 75°C, 100°C and 125°C are seen to form almost immediately after yielding. With increases in temperature to 75°C, 100°C and

125°C, the serration intensity is also seen to increase. With a still greater increase in temperature

to 150°C, there is no indication of DSA serrations and the curve obtained is smooth.

4.1.4   Stress vs. Strain – Al-3%Mg, $\dot{\varepsilon} = 10^{-1}\,\text{s}^{-1}$

The stress vs. temperature curve obtained for Al-3%Mg vs. that for commercially pure Al

at $\dot{\varepsilon} = 10^{-1}\,\text{s}^{-1}$ is shown in Figure 4.8.

Figure 4.8.   Stress vs. temperature curve for Al-3%Mg at $\dot{\varepsilon} = 10^{-1}\,\text{s}^{-1}$.

As with the behavior observed at $\dot{\varepsilon} = 10^{-1}\,\text{s}^{-3}$ and $\dot{\varepsilon} = 10^{-2}\,\text{s}^{-1}$, this curve also displays a

'hump', although at higher temperatures, given the increase in strain rate. The "DSA-free"

commercially pure Al is noted to simply soften with increasing temperature. Overlapping the

curves of Figures 4.4, 4.6 and 4.8 would again result in a negative strain rate sensitivity region at

lower temperatures, as well as a region of abnormally high strain rate sensitivity at higher

temperatures. The stress vs. strain curves obtained for Al-3%Mg during the DSA regime at $\dot{\varepsilon} =$ 10^{-1} s^{-1} are presented in Figure 4.9.

Figure 4.9.   Stress vs. strain curves for Al-3%Mg at $\dot{\varepsilon} = 10^{-1}$ s^{-1}.

The curves obtained at -50°C, -25°C and 0°C are smooth with no indication of DSA serrations. It should be noted that although serrations were observed at these temperatures at lower strain rates, it is expected that the DSA regime will shift to higher temperatures with increasing strain rates. Thus, the onset of serrations measured for 10% strain will also be delayed to higher temperatures. With no serrations observed, it is again anticipated that one is in the low temperature/'no serration' regime, just prior to the onset of the DSA 'hump'.

The stress vs. strain curve at 25°C features step-like serrations that are seen to begin at

$\varepsilon\sim0.036$. The serrations observed at 50°C, 75°C, 100°C, 125°C, 150°C and 175°C are observed

to form almost immediately after yielding. Although the serration intensity is seen to increase

until 150°C, it slowly begins to grow faint at 175°C. With a still higher increase in temperature

to 200°C, there is no indication of DSA serrations and the curve obtained is smooth.

4.1.5   Stress vs. Strain – Al-5%Mg, $\dot{\varepsilon} = 10^{-3}\ s^{-1}$

The stress vs. temperature curve obtained for Al-5%Mg vs. that for commercially pure Al

at $\dot{\varepsilon} = 10^{-3}\ s^{-1}$ is displayed in Figure 4.10.
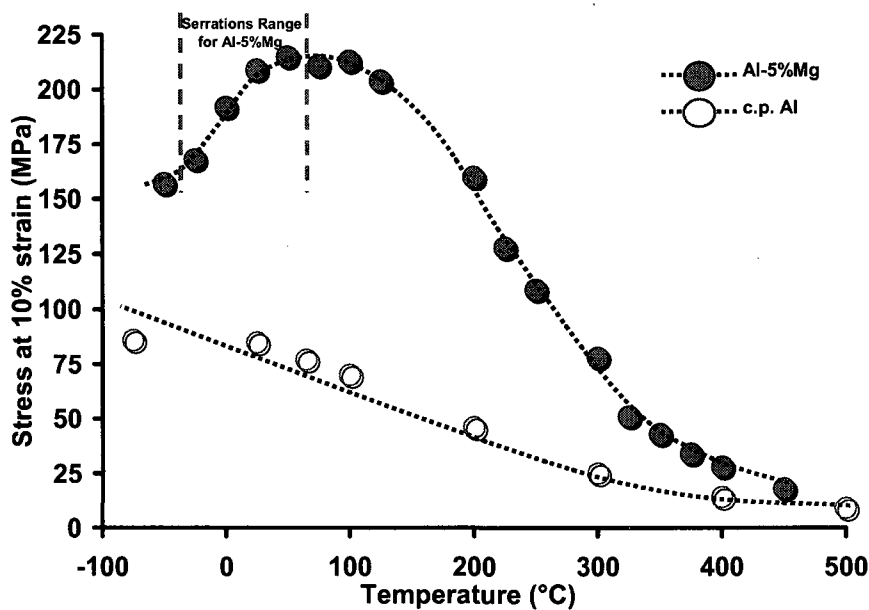
Figure 4.10.   Stress vs. temperature curve for Al-5%Mg at $\dot{\varepsilon} = 10^{-3}\ s^{-1}$.

The 'hump' that occurs for the Al-5%Mg in Figure 4.10 is more pronounced than in

Figure 4.4 for Al-3%Mg. As with Al-3%Mg, the stress vs. temperature curve reaches a peak at

~75°C and eventually decreases with increasing temperature. Furthermore, the temperature

points within the DSA 'hump' exhibit serrations that increase in intensity with increasing temperature. The stress vs. strain curves obtained for Al-5%Mg during the DSA regime at $\dot{\varepsilon}$ = 10^{-3} s^{-1} are given in Figure 4.11.
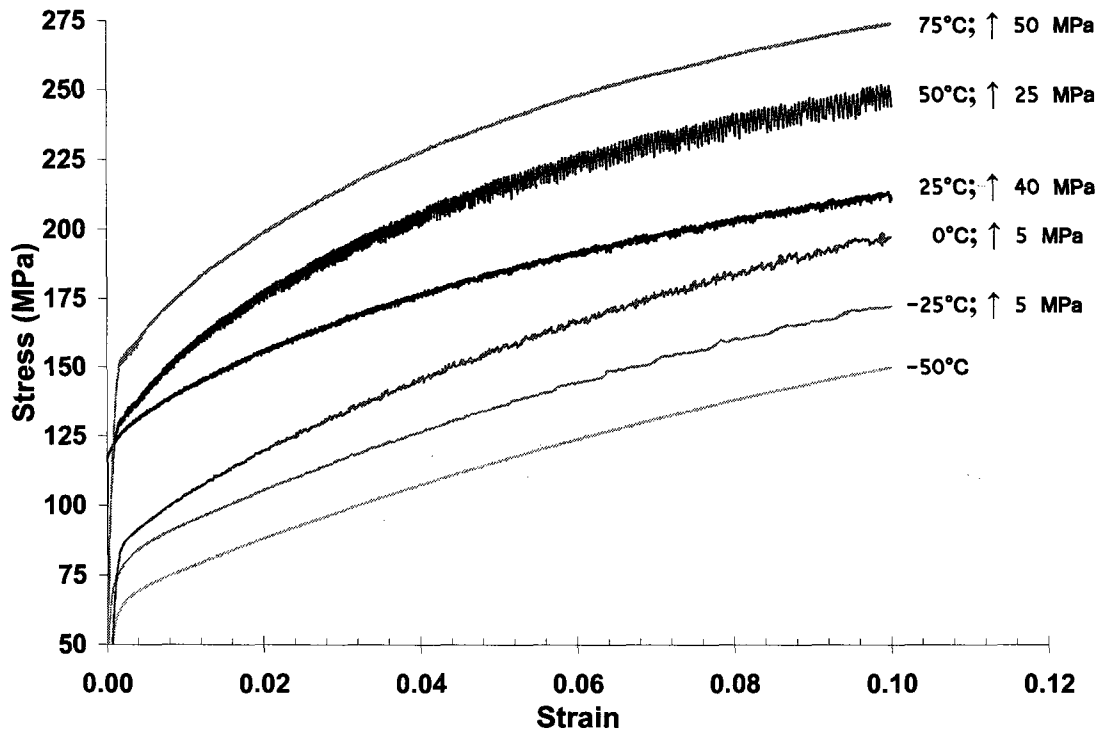
Figure 4.11.   Stress vs. strain curves for Al-5%Mg at $\dot{\varepsilon}$ = 10^{-3} s^{-1}.

As can be seen, the curve at -50°C is smooth with no indication of DSA serrations. Serrations are expected to occur with increasing temperature, provided they do not begin at higher strains for the given temperature. At -25°C, step-like serrations are noted to begin at $\varepsilon \sim 0.03$ and it is evident that these 'steps' are occurring much more frequently at 0°C. Similarly, the serrations taking place at 25°C closely resemble those at 0°C although they occur more frequently at 25°C, for the same 10% strain.

The serration intensity is seen to increase greatly from 25°C to 50°C. The serrations at

0°C, 25°C and 50°C occur almost immediately after yielding. With a still higher increase in

temperature to 75°C, there is no indication of DSA serrations and the curve obtained is smooth.

4.1.6   Stress vs. Strain – Al-5%Mg, $\dot{\varepsilon} = 10^{-2}\,s^{-1}$

The stress vs. temperature curve obtained for Al-5%Mg vs. that for commercially pure Al

at $\dot{\varepsilon} = 10^{-2}\,s^{-1}$ is displayed in Figure 4.12.
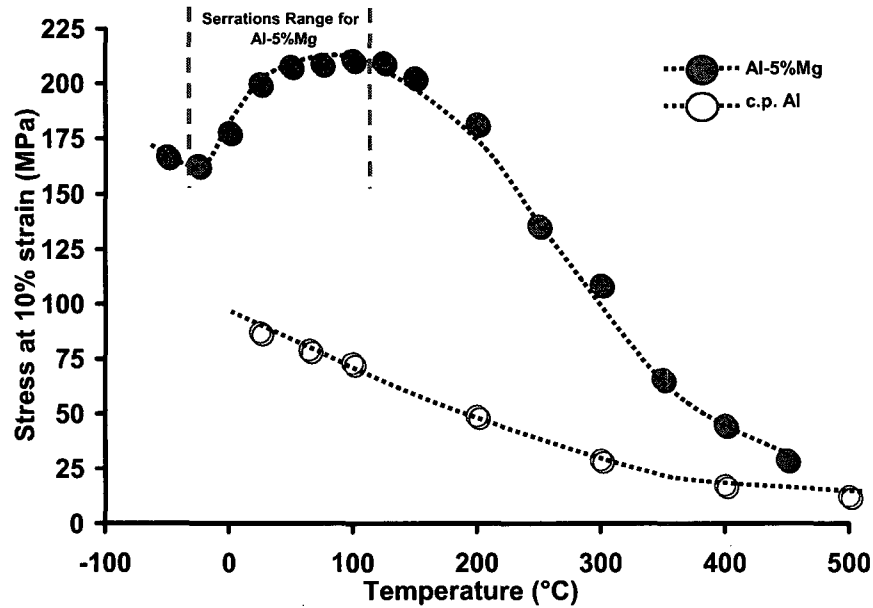
Figure 4.12.   Stress vs. temperature curve for Al-5%Mg at $\dot{\varepsilon} = 10^{-2}\,s^{-1}$.

The 'hump' observed in the Al-5%Mg is similar to that defined in Figure 4.10, although

shifted to higher temperatures. The initial descent in stress at low temperatures is also well

defined. It is anticipated that at still lower temperatures, the stress would continue to increase. As

with previous tests, the stress vs. strain curves in the DSA regime displayed serrations. The stress

vs. strain curves obtained for Al-5%Mg during the DSA regime at $\dot{\varepsilon} = 10^{-2}$ s^{-1} are presented in

Figure 4.13.
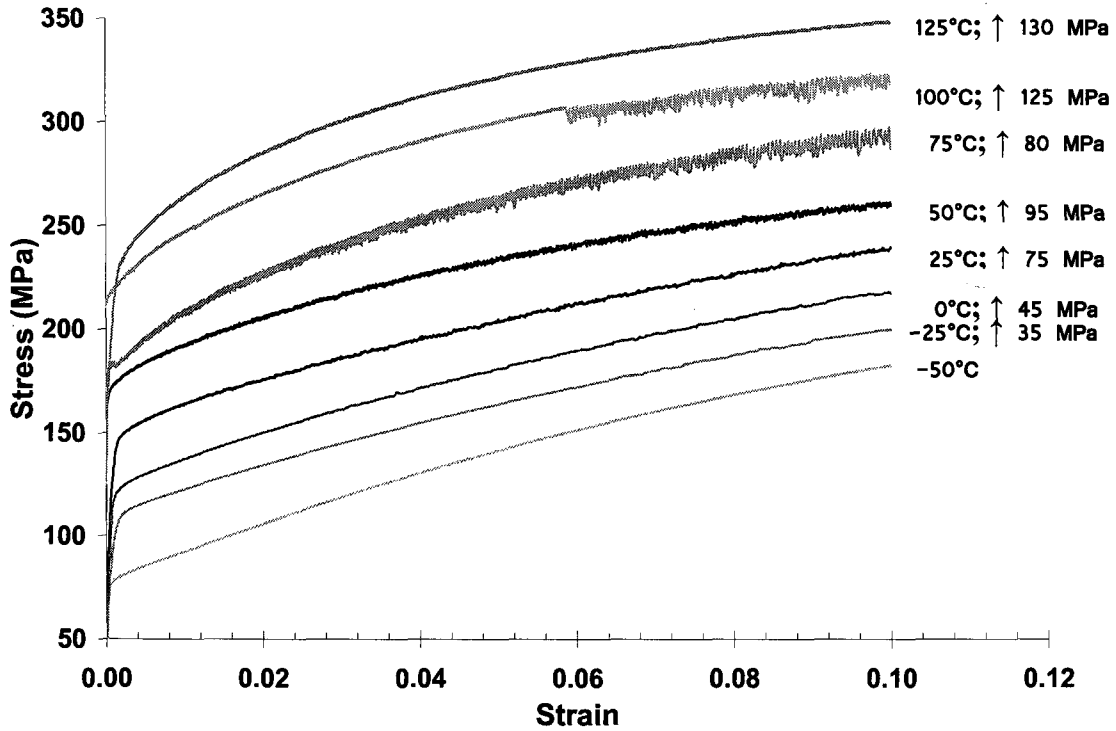
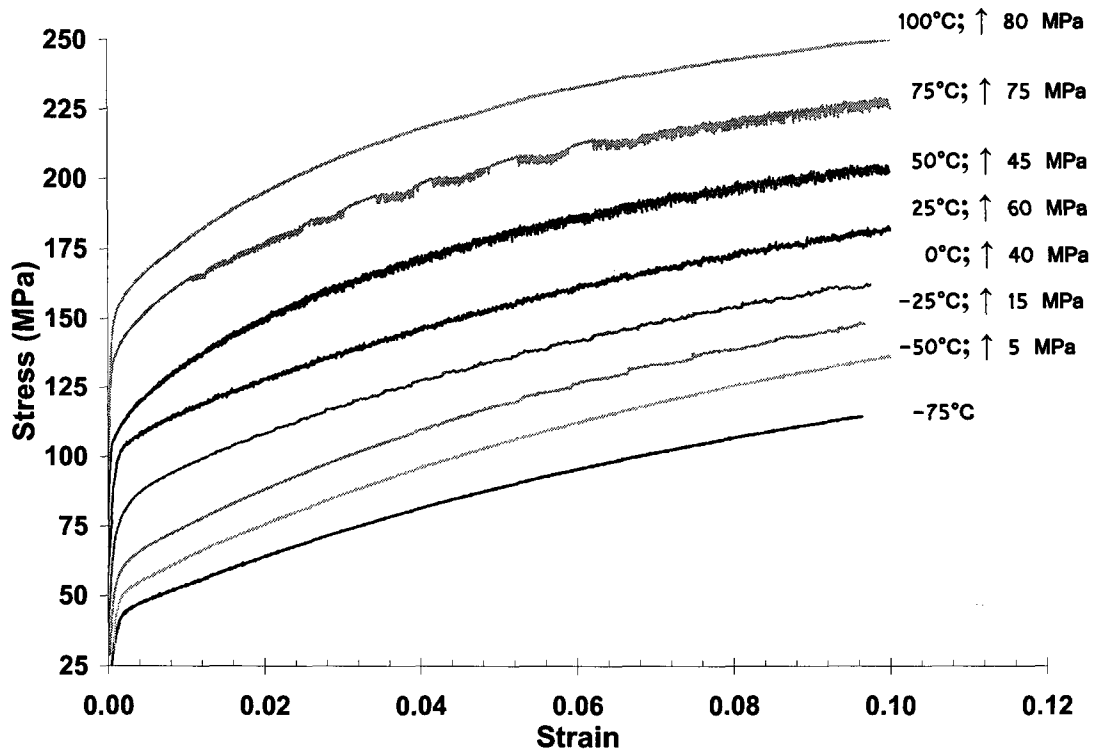**Figure 4.13. Stress vs. strain curves for Al-5%Mg at $\dot{\varepsilon} = 10^{-2}$ s^{-1}.**

The stress-strain curve obtained at -50°C is smooth with no indication of DSA serrations,

whereas the curve obtained at -25°C shows signs of faint serrations forming at ε~0.07. Faint

serrations similar to those at -25°C are also seen to occur at 0°C, although at a lower value of

critical strain (ε~0.03), as expected. At 25°C, the serrations are jagged in appearance and occur

much more frequently.

The stress-strain curves at 50°C to 100°C show increasing serration intensity, yet at

100°C, it is seen that serrations are delayed to a strain of ~0.06. This signals the end of the DSA

regime and it is anticipated that with higher temperatures, smooth stress-strain curves should be

observed. At a still higher temperature, 125°C, there is no indication of DSA serrations and the

curve obtained is smooth.

4.1.7   Stress vs. Strain – Al-5%Mg, $\dot{\varepsilon} = 10^{-1}\,\mathrm{s}^{-1}$

The stress vs. temperature curve obtained for Al-5%Mg vs. that for commercially pure Al

at $\dot{\varepsilon} = 10^{-1}\,\mathrm{s}^{-1}$ is displayed in Figure 4.14.
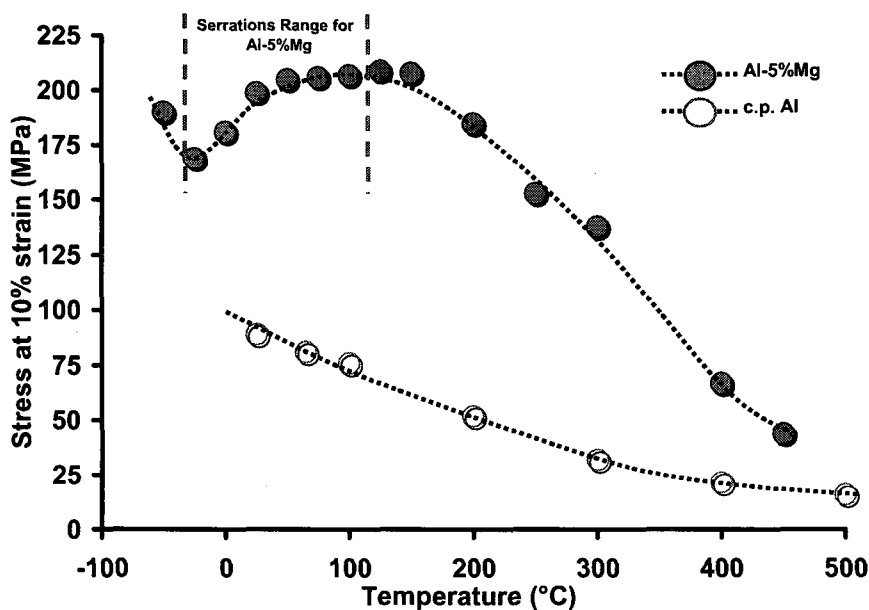
Figure 4.14.   Stress vs. temperature curve for Al-5%Mg at $\dot{\varepsilon} = 10^{-1}\,\mathrm{s}^{-1}$.

The 'hump' observed in the Al-5%Mg is similar to that defined in Figure 4.12 and is,

again, shifted to higher temperatures. The stress vs. strain curves obtained for Al-5%Mg during

the DSA regime at $\dot{\varepsilon} = 10^{-1}\,\mathrm{s}^{-1}$ are given in Figure 4.15.
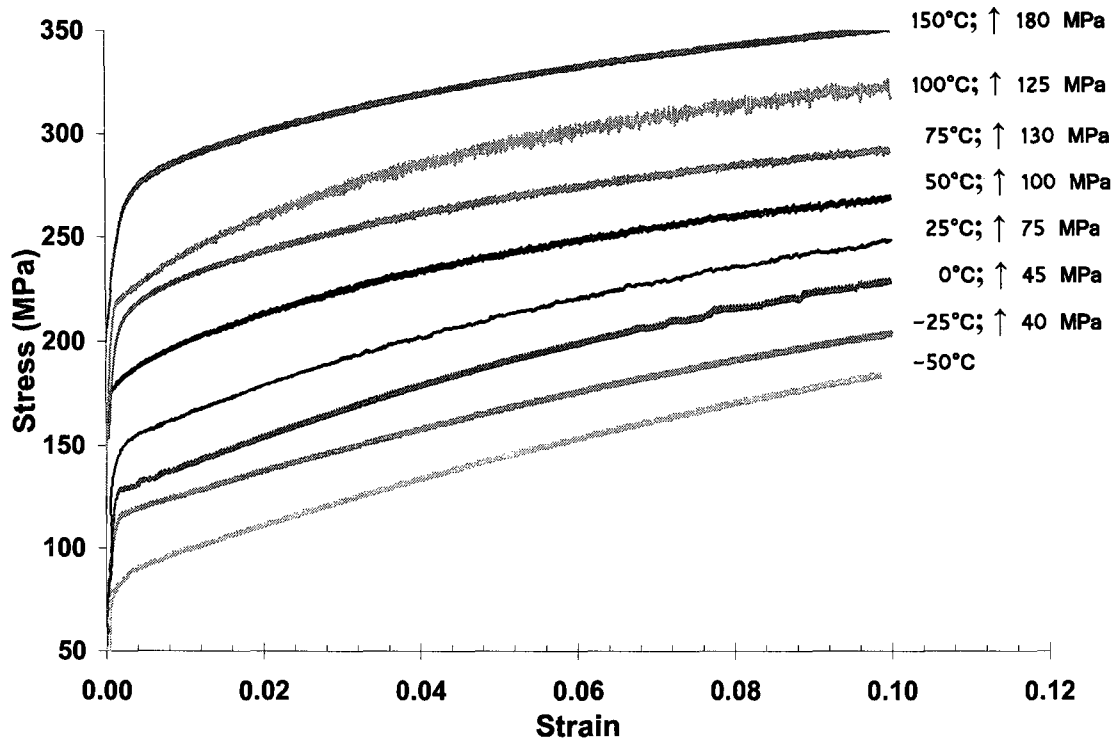
Figure 4.15.   Stress vs. strain curves for Al-5%Mg at $\dot{\varepsilon} = 10^{-1}\,s^{-1}$.

As can be seen, the stress-strain behavior at -50°C results in a smooth curve with no indication of DSA. At 0°C, step-like serrations begin to form at $\varepsilon{\sim}0.068$. The serrations observed at 25°C are more apparent after $\varepsilon{\sim}0.03$. It is expected that the critical strain for the onset of serrations will decrease with increasing temperature for a given strain rate.

The stress-strain curves at 50°C and 75°C show an increase in serration intensity from 25°C, yet these serrations are much more apparent at 100°C. Knowing that the DSA serration region will shift to higher temperatures with higher strain rates, it is expected that the serrations at $\dot{\varepsilon} = 10^{-1}\,s^{-1}$ will continue on to higher temperatures. It was found that serrations only disappeared when the temperature was raised to 150°C.

4.1.8   Stress vs. Strain – AA 5056, $\dot{\varepsilon} = 10^{-3}\,s^{-1}$

The stress vs. temperature curve obtained for AA 5056 vs. that for commercially pure Al at $\dot{\varepsilon} = 10^{-3}\,s^{-1}$ is displayed in Figure 4.16.
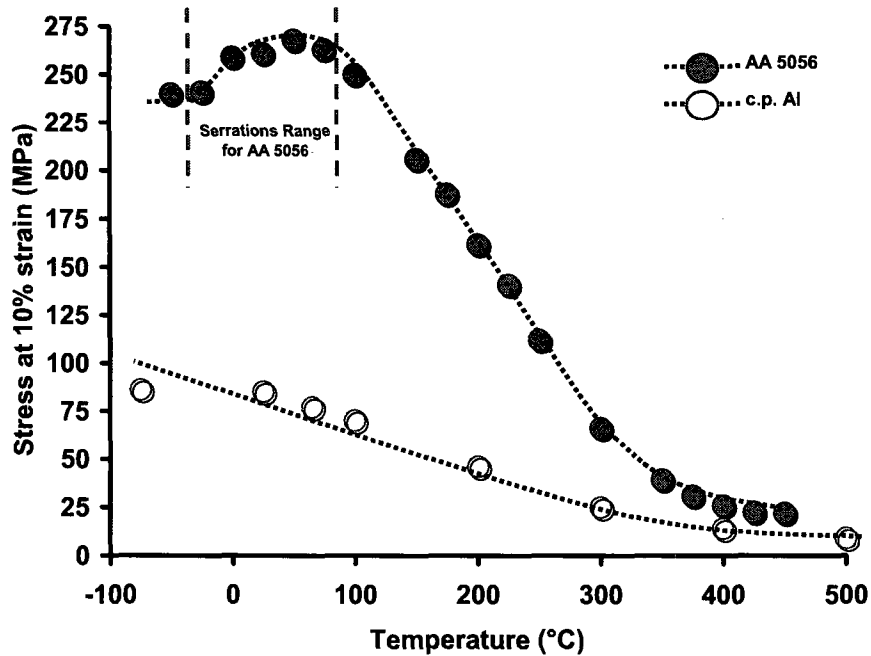
Figure 4.16.   Stress vs. temperature curve for AA 5056 at $\dot{\varepsilon} = 10^{-3}\,s^{-1}$.

The 'hump' formed in the AA 5056 alloy is well defined and similar to those found in the previous figures. Similarly, the stress vs. strain curves in the DSA regime displayed serrations.The stress vs. strain curves obtained for AA 5056 during the DSA regime at $\dot{\varepsilon} = 10^{-3}\,s^{-1}$ are presented in Figure 4.17. It is interesting to note the occurrence of yield point elongations (YPE) at all temperatures, although it is not as pronounced at 75°C.
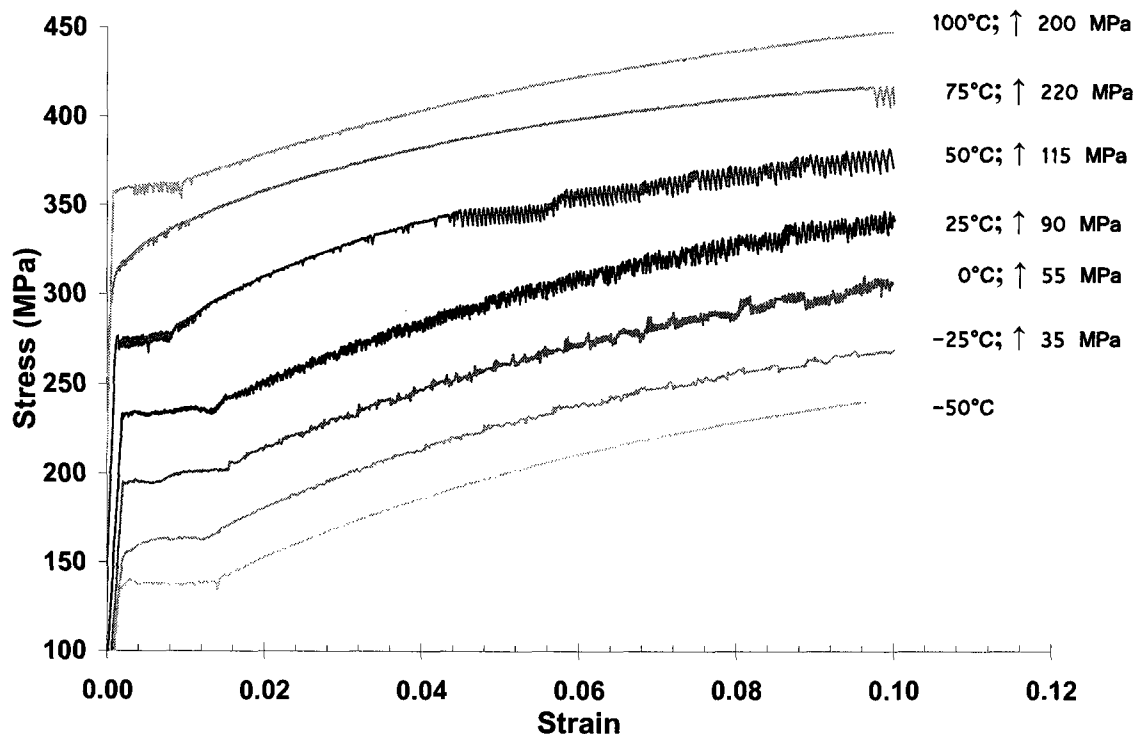
Figure 4.17.   Stress vs. strain curves for AA 5056 at $\dot{\varepsilon} = 10^{-3}\ s^{-1}$.

At -50°C, the stress vs. strain curve is smooth with a yield plateau, yet there is no indication of DSA serrations. The yield plateaus observed are associated with *static* as opposed to dynamic aging. Similar to the case of Al-3%Mg and Al-5%Mg, at this low a temperature, for the given strain rate, one is in the 'no serration' regime and increases in temperature (or decreases in strain rate if the temperature is held constant) are required in order for serrations to appear.

The stress vs. strain curves at -25°C and 0°C display faint serrations beginning at ε~0.025 at -25°C and increasing in intensity at 0°C. The serrations observed at 25°C are seen to occur much more frequently and follow a consistent pattern compared to those observed at 0°C. At 50°C and 75°C, serrations are delayed to ε~0.045 and ε~0.098, respectively. One should expect

that the 'no serration' regime is fast approaching. This is confirmed at 100°C, in which the stress vs. strain curve is smooth and there are no indications of DSA serrations.

4.1.9 Stress vs. Strain – AA 5056, $\dot{\varepsilon} = 10^{-2}$ s^{-1}

The stress vs. temperature curve obtained for AA 5056 vs. that for commercially pure Al at $\dot{\varepsilon} = 10^{-2}$ s^{-1} is displayed in Figure 4.18.
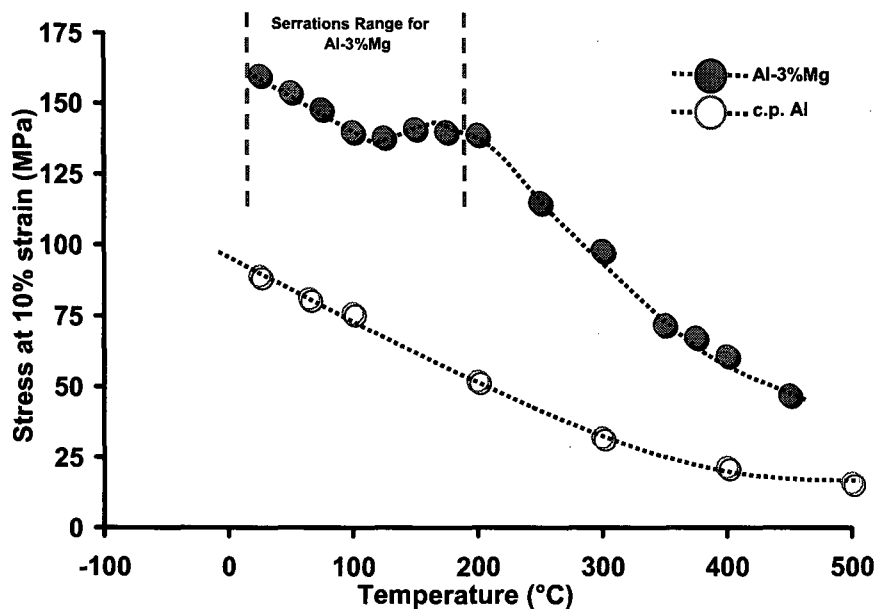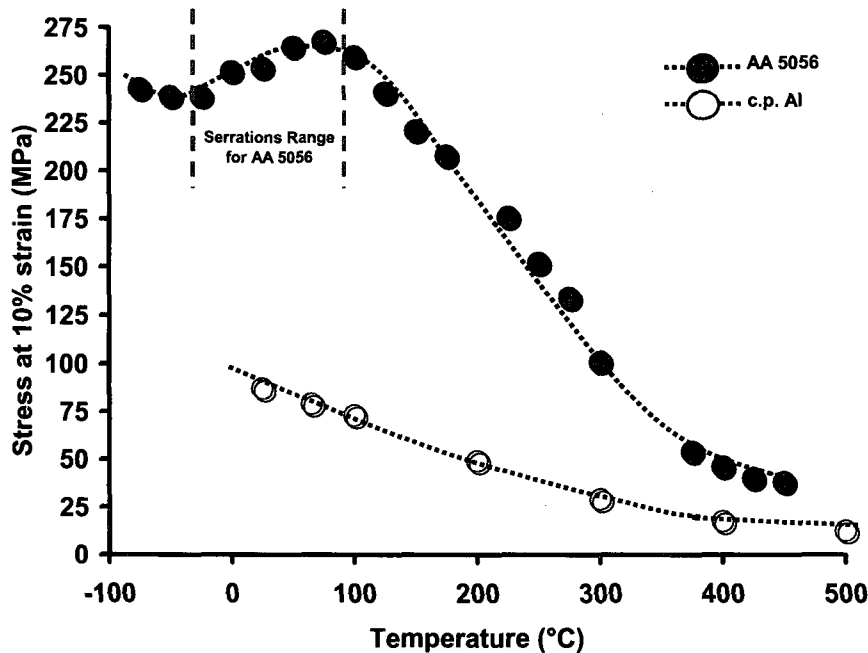

Figure 4.18. Stress vs. temperature curve for AA 5056 at $\dot{\varepsilon} = 10^{-2}$ s^{-1}.

This AA 5056 curve shown in Figure 4.18 is similar to the Al-5%Mg curve in Figure 4.16, except that the DSA 'hump' has now shifted to the right, i.e. to higher temperatures, given the increase in strain rate from 10^{-3} s^{-1} to 10^{-2} s^{-1}. Dynamic strain aging serrations are prevalent in the stress-strain curves along the 'hump'. The stress vs. strain curves for AA 5056 during the DSA regime at $\dot{\varepsilon} = 10^{-2}$ s^{-1} are presented in Figure 4.19.
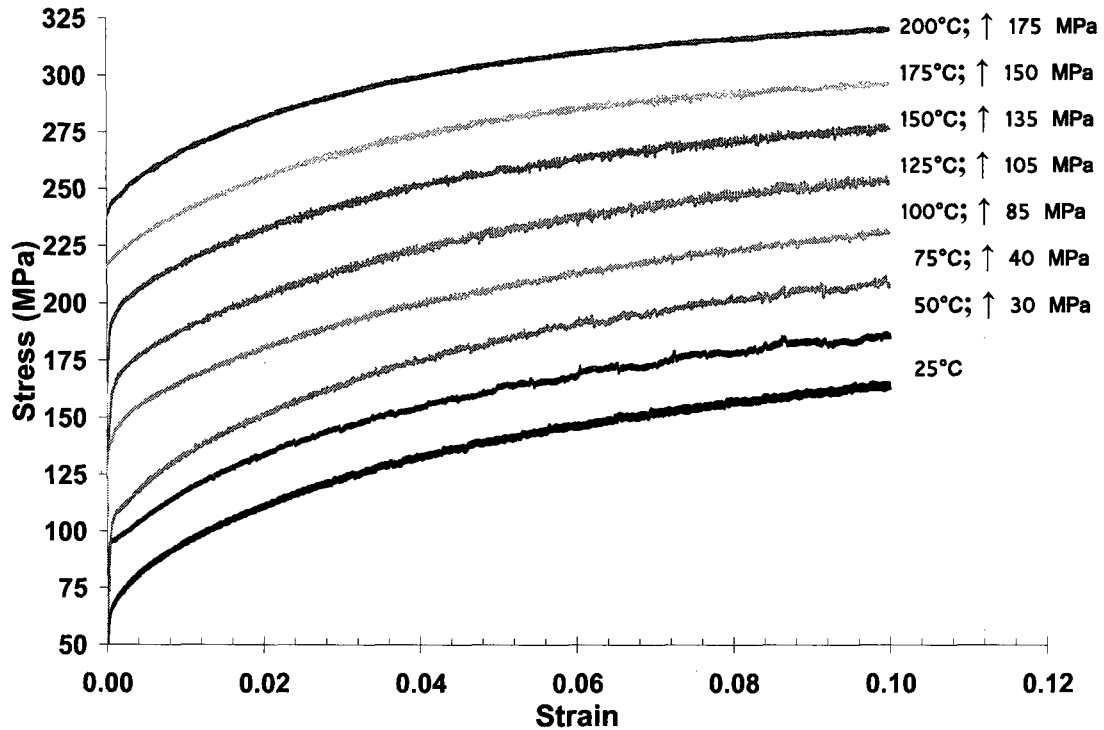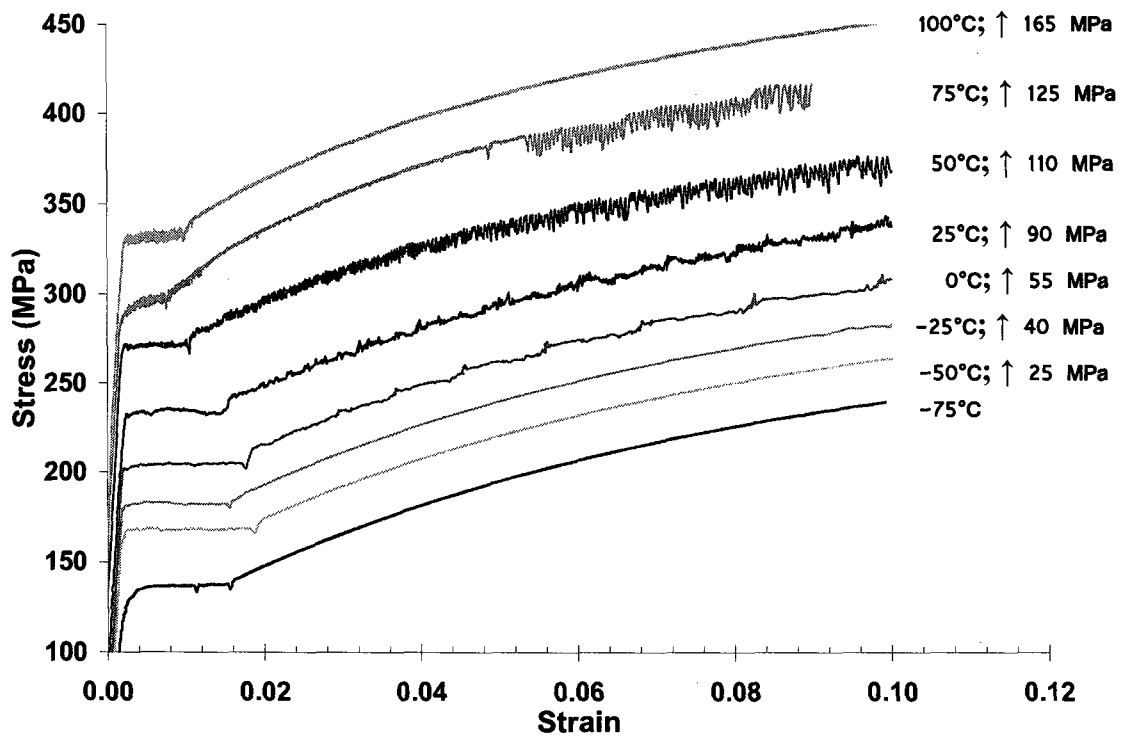
Figure 4.19. Stress vs. strain curves for AA 5056 at $\dot{\varepsilon} = 10^{-2}$ s^{-1}.

At -75°C and -50°C, the stress-strain curves are smooth with no indication of DSA serrations. At -25°C, faint serrations are seen to form at $\varepsilon\sim0.09$. More obvious step-like serrations are observed at 0°C, beginning at a lower value of strain than at -25°C, as expected.

With an increase in temperature to 25°C and 50°C, the serrations occur more frequently. The serration intensity at 50°C is also noticeably greater than at 25°C. These serrations continue until 75°C. Here, the critical strain is ~0.05. It is anticipated that with higher temperatures, one will exit the DSA serration range. This is shown at 100°C, where the stress-strain curve obtained is smooth. As with tensile tests performed at 10^{-3} s^{-1}, the results shown in Figure 4.19 display YPE's.

4.1.10   Stress vs. Strain – AA 5056, $\dot{\varepsilon} = 10^{-1}$ s^{-1}

The stress vs. temperature curve obtained for AA 5056 vs. that for commercially pure Al

at $\dot{\varepsilon} = 10^{-1}$ s^{-1} is displayed in Figure 4.20.
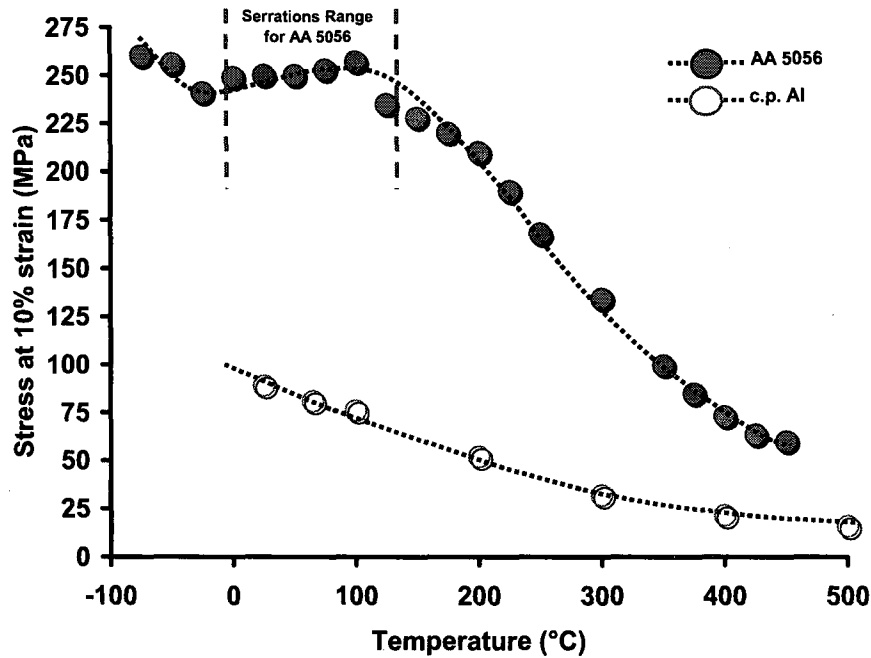
Figure 4.20.   Stress vs. temperature curve for AA 5056 at $\dot{\varepsilon} = 10^{-1}$ s^{-1}.

As expected, the DSA 'hump' in the AA 5056 has now shifted further to higher

temperatures, given the increase in strain rate from 10^{-3} s^{-1} to 10^{-2} s^{-1} to 10^{-1} s^{-1}. The stress vs.

strain curves obtained for AA 5056 during the DSA regime at $\dot{\varepsilon} = 10^{-1}$ s^{-1} are presented in

Figure 4.21. Again, as with tensile tests performed at 10^{-3} s^{-1} and 10^{-2} s^{-1}, the results shown in

Figure 4.21 display YPE's.
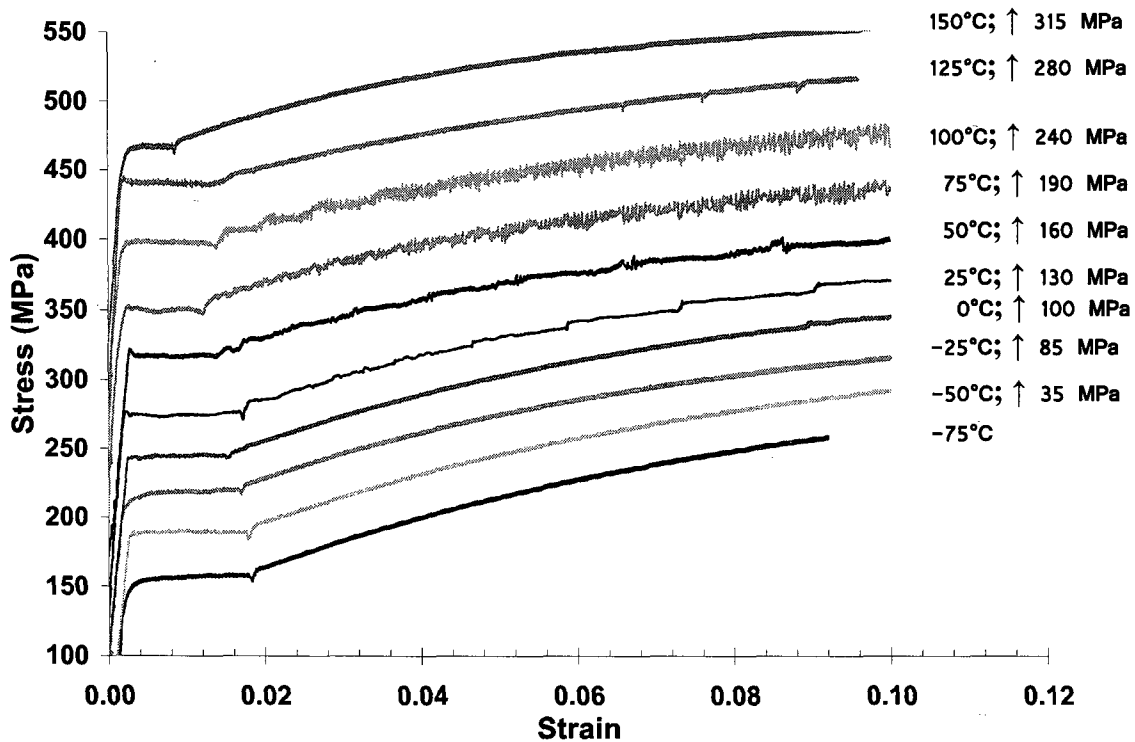
Figure 4.21.   Stress vs. strain curves for AA 5056 at $\dot{\varepsilon} = 10^{-1}$ s^{-1}.

The stress-strain curves obtained at -75°C, -50°C and -25°C are smooth with no indication of DSA serrations. At $\dot{\varepsilon} = 10^{-1}$ s^{-1}, it is expected that serrations will appear at temperatures higher than those observed at $\dot{\varepsilon} = 10^{-2}$ s^{-1} and $\dot{\varepsilon} = 10^{-3}$ s^{-1}. With an increase in temperature to 0°C, faint step-like serrations are seen to form at a strain of nearly 0.09. These steps are observed to become more pronounced when the temperature is increased to 25°C; moreover, the critical strain is reduced. Serrations resembling those at 25°C occur more frequently at 50°C. There is an increase in serration intensity at 75°C and 100°C, and serrations are seen to form after yielding. However, when the temperature is raised to 125°C and then, 150°C, the resulting curve is smooth with no indication of DSA serrations.

4.2   Stress vs. Temperature

The stress vs. temperature curves for the three alloys tested are summarized in Figures 4.22 to 4.24, in Sections 4.2.1 to 4.2.3. These curves display areas of negative strain rate sensitivity at low temperatures, as well as their respective high rate sensitivity regimes. It should be noted that the commercially pure Al used in this work was found to simply decrease monotonically in stress with increasing temperature and display no evidence of DSA. As always, the curves obtained were shifted to higher temperatures as the strain rate was increased.

4.2.1   Stress vs. Temperature – Al-3%Mg

The stress vs. temperature curves for Al-3%Mg at the prescribed strain rates (10^{-3} s^{-1}, 10^{-2} s^{-1} and 10^{-1} s^{-1}) are summarized in Figure 4.22.
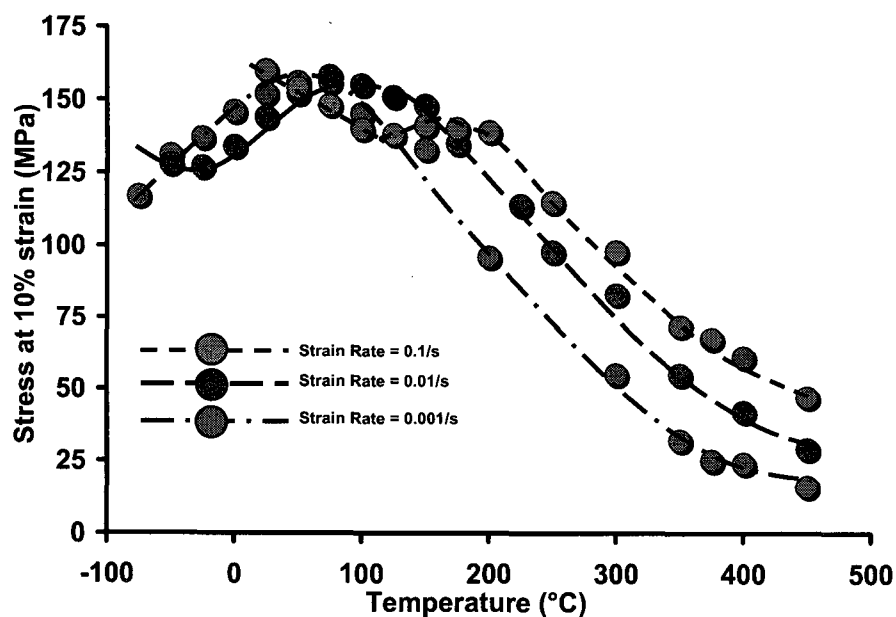
Figure 4.22.   Stress vs. temperature curves for Al-3%Mg for strain rates of 10^{-3} s^{-1}, 10^{-2} s^{-1} and 10^{-1} s^{-1}.

As can be seen, the DSA 'humps' that are formed are shifted to the right (i.e. to higher temperatures) with increased strain rates. As observed before in Figures 4.5, 4.7 and 4.9, the samples tested within the DSA 'humps' displayed serrations. These serrations began at critical strains that decreased with increasing temperature for a given strain rate. Under certain conditions, serrations were seen to form almost immediately after yielding or else were delayed to strains beyond the measured 10%.

4.2.2   Stress vs. Temperature – Al-5%Mg

The stress vs. temperature curves for Al-5%Mg at the prescribed strain rates (10^{-3} s^{-1}, 10^{-2} s^{-1} and 10^{-1} s^{-1}) are summarized in Figure 4.23.
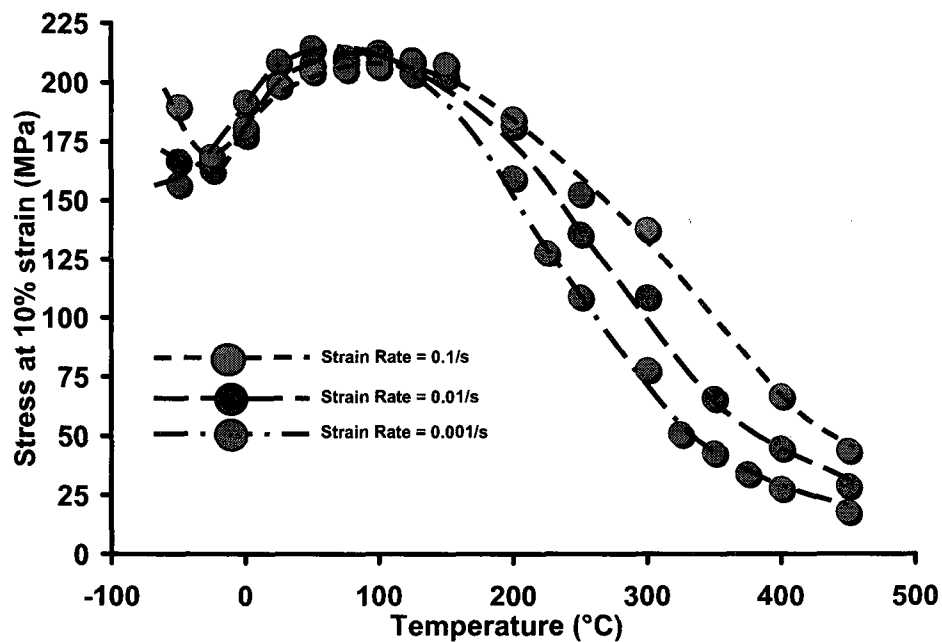
Figure 4.23. Stress vs. temperature curves for Al-5%Mg for strain rates of 10^{-3} s^{-1}, 10^{-2} s^{-1} and 10^{-1} s^{-1}.

As in the case of Al-3%Mg, the DSA 'humps' that are formed are shifted to higher temperatures with an increase in strain rate. Moreover, the samples tested within the DSA 'humps' displayed serrations, as was observed in Figures 4.11, 4.13 and 4.15. In this case also, these serrations began at critical strains that decreased with increasing temperature for a given strain rate and, under certain conditions, were seen to form almost immediately after yielding or were delayed to strains beyond the measured 10%.

4.2.3   Stress vs. Temperature – AA 5056

The stress vs. temperature curves for AA 5056 at the prescribed strain rates (10^{-3} s^{-1}, 10^{-2} s^{-1} and 10^{-1} s^{-1}) are summarized in Figure 4.24.
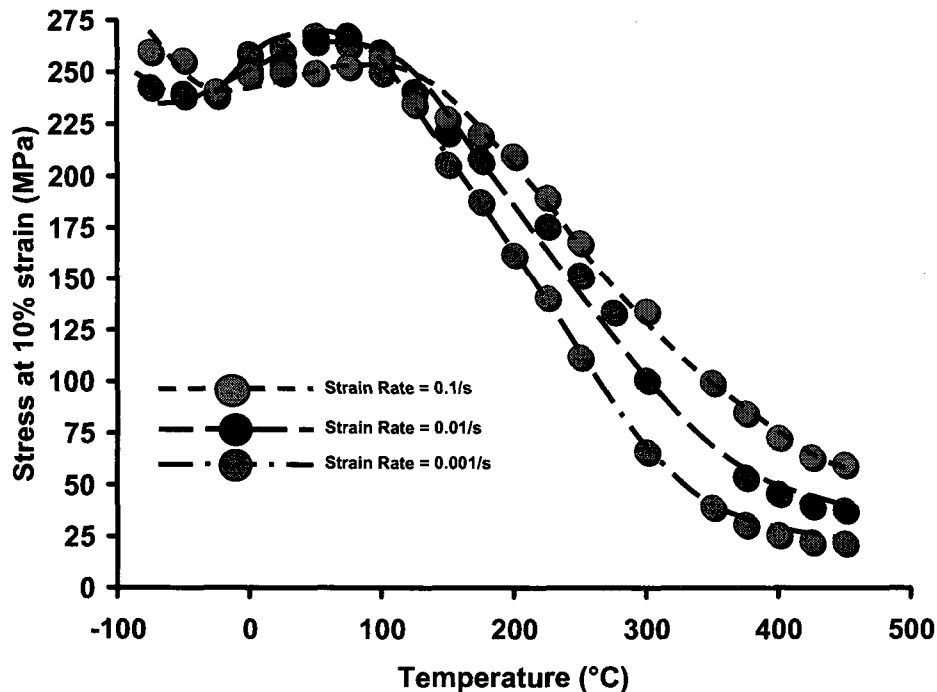
Figure 4.24.   Stress vs. temperature curve for AA 5056 for strain rates of 10^{-3} s^{-1}, 10^{-2} s^{-1} and 10^{-1} s^{-1}.

The samples tested within the DSA 'humps' showed serrations, as observed in Figures 4.17, 4.19 and 4.21. As before, these 'humps' are shifted to higher temperatures as the strain rate is increased. As with the other two alloys being studied, the serrations occurring in AA 5056 begin at critical strains that decrease with increasing temperature for a given strain rate. Under certain conditions, the serrations are seen to form almost immediately after a yield plateau (yield point elongation (YPE)) has formed. When the temperature is increased to beyond the serrations range, the curves show no yield plateau or indication of DSA serrations.

4.3   Enhanced Ductility Tensile Tests

Numerous tensile tests were carried out to failure to test for extended ductility. Several geometries were attempted seeing as how many authors use a geometry that is unique to their work and no one unified geometry has been mentioned in the literature. Given the publication of the ASTM E2448-06 standard for superplasticity tensile tests, reproducible tests were carried out for each alloy and are described in more detail in Chapter 5.

Since the aim of this portion of the work was to test for superplastic properties, the test temperature range was chosen to be such that the expected strain rate sensitivity behavior will be observed with the Mg still in solid solution. For these shortened samples, a solution heat treatment of 2 hours at 560°C was employed to maintain the Mg in solution (i.e. retain the material in the single phase α region). The resulting coarse Al-Mg grain sizes were approximately the same as reported on p. 37, i.e. ~130 μm, ~145 μm and ~15 μm for Al-3%Mg, Al-5%Mg and AA 5056 alloys, respectively. These are shown in Figures 4.25 and 4.26. The results of the enhanced ductility tensile tests are presented in Figures 4.27 to 4.29.
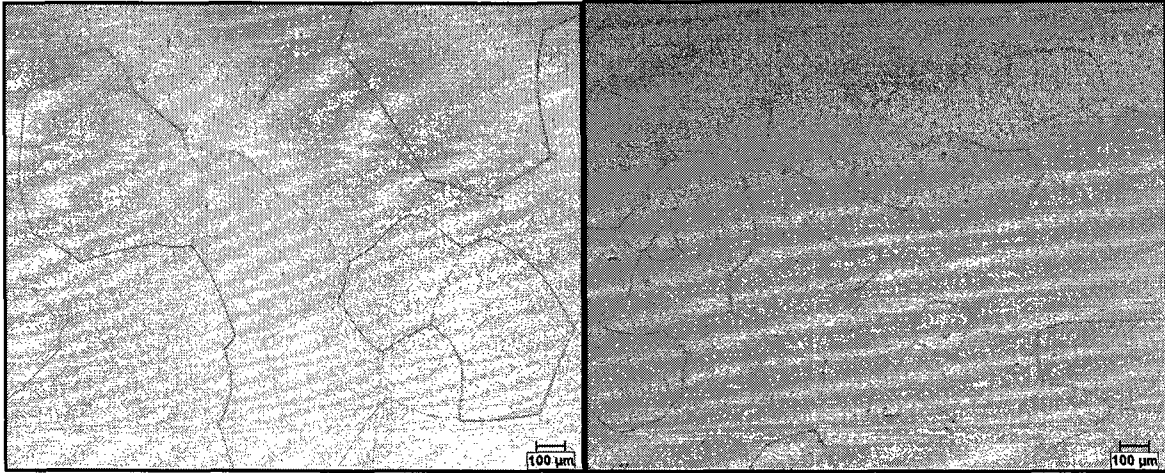
Figure 4.25. Grain sizes for Al-3%Mg (left) and Al-5%Mg (right) after a solution heat-treatment of 2 hours at 560°C (i.e. before testing), taken at 50X.
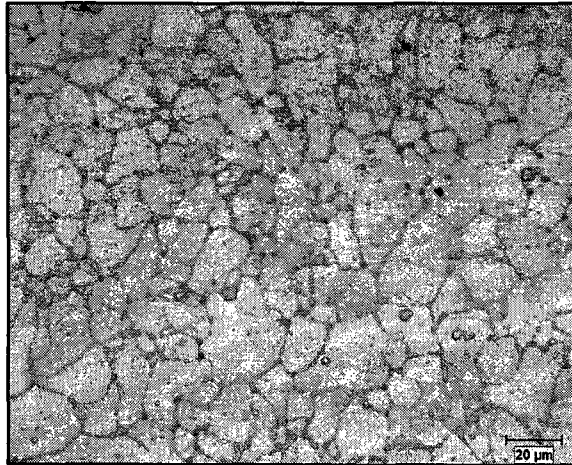
Figure 4.26. Grain size of AA 5056 after solution heat-treatment of 2 hours at 560°C (i.e. before testing), taken at 500X.
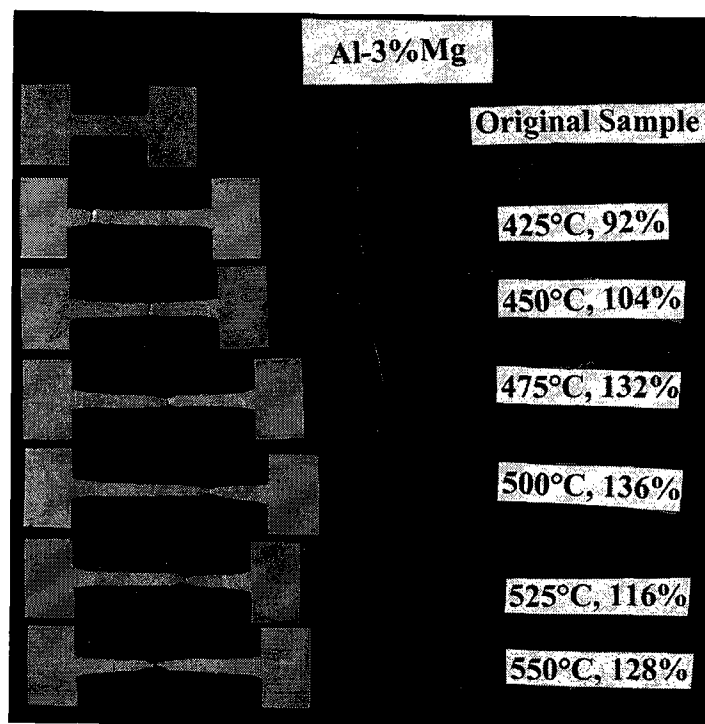
Figure 4.27. Al-3%Mg samples deformed at temperatures in the vicinity of the high strain rate sensitivity peak at a strain rate of 5×10^{-3} s^{-1}.
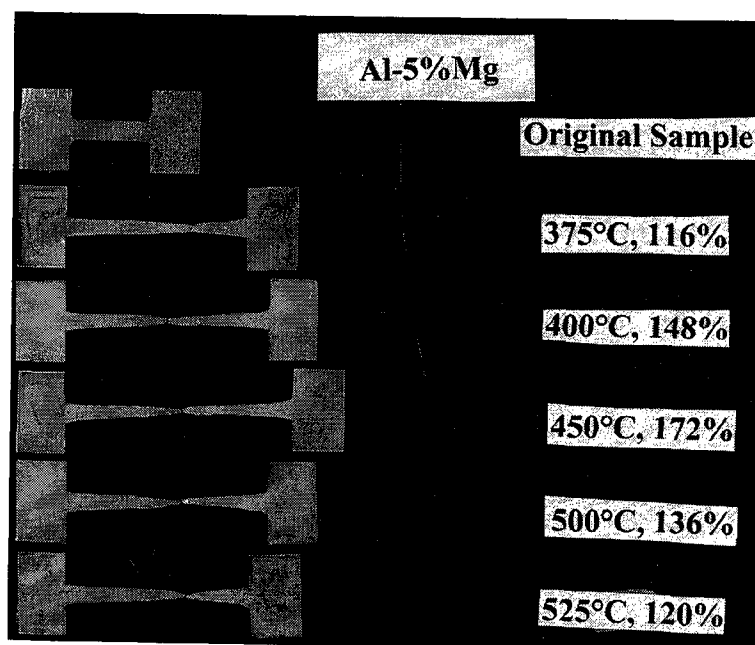
Figure 4.28. Al-5%Mg samples deformed at temperatures in the vicinity of the high strain rate sensitivity peak at a strain rate of 5×10^{-3} s^{-1}.
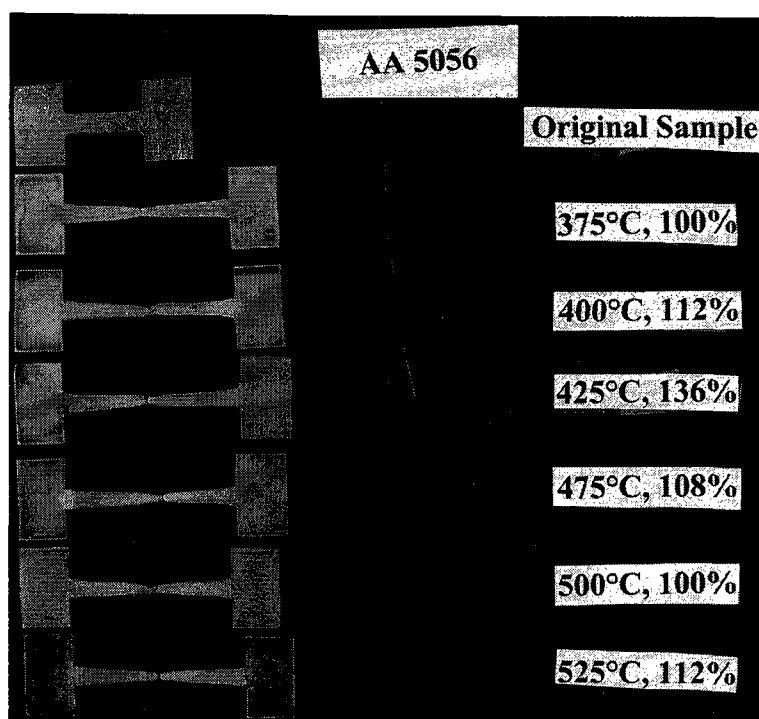
**Figure 4.29.   AA 5056 samples deformed at temperatures in the vicinity of the high strain
rate sensitivity peak at a strain rate of 5x10^{-3} s^{-1}.**

It is evident from Figures 4.27 to 4.29 that the ductility reaches a local maximum at a
temperature well below the maximum test temperature, as predicted by the flow stress vs.
temperature behavior observed in the standard tensile tests. Moreover, there is a steady increase
in percent elongation of the alloys are tested at increasing temperatures until the point of
maximum ductility is reached. Following this point, the amount of ductility observed decreases,
somewhat unexpectedly. This coincides with the behavior predicted by the strain rate sensitivity
vs. temperature curves. In conventional materials, the strain rate sensitivity increases
continuously with temperature, so that the elongation increases monotonically as well. This
expectation applies particularly to materials in which solute drag is the rate-controlling
mechanism.

Earlier attempts at high temperature tensile tests to failure (Figures 4.30 to 4.32) showed

potential in terms of achieving enhanced ductility, yet the results shown above follow the

anticipated 'unexpected' DSA behavior, i.e. where a material could reach a high level of ductility

before reaching its maximum test temperature.
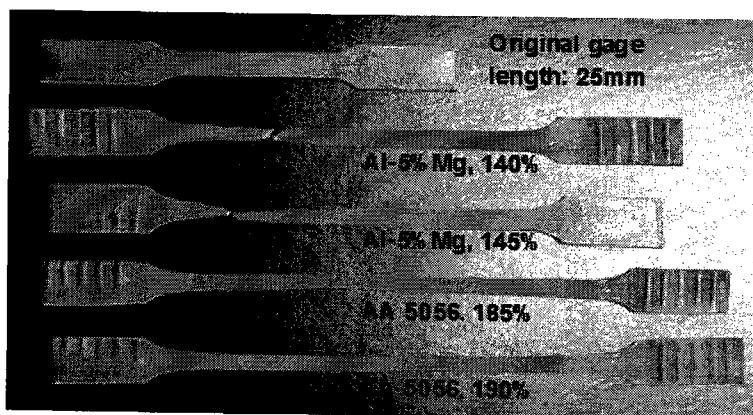
**Figure 4.30.   Early attempt at enhanced elongation in Al-5%Mg and AA 5056 using
ASTM tensile samples at a 425°C and a strain rate of 10^{-4} s^{-1}.**
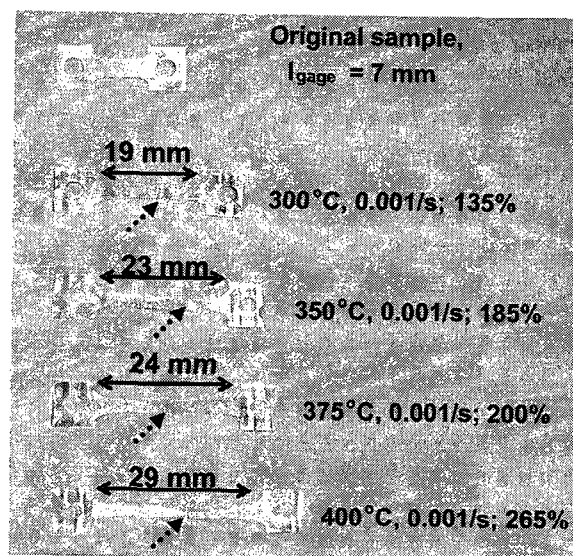
**Figure 4.31.   Early attempt at enhanced elongation in Al-3%Mg using very short samples
at a strain rate of 10^{-3} s^{-1}.**
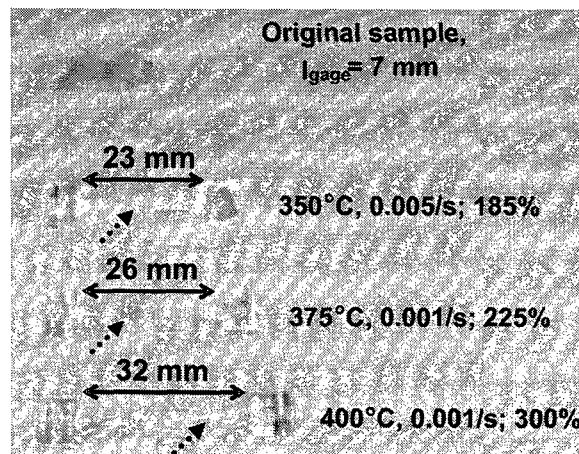
Figure 4.32. **Early attempt at enhanced elongation in Al-5%Mg using very short samples at a strain rate of 10^{-3} s^{-1}.**

As can be seen from Figure 4.30, the commercial alloy AA 5056 shows an increase in ductility of nearly 50% compared to that of the binary Al-5%Mg alloy. Standard tensile samples were used to obtain an estimate of the elongations possible, prior to using shorter gage lengths. One attempt at enhanced ductility using shorter gage lengths is given in Figures 4.31 and 4.32, where peak ductilities of 265% and 300% were obtained at 400°C and $\dot{\varepsilon} = 10^{-3}$ s^{-1} in the Al-3%Mg and Al-5%Mg, respectively. Although the alloys seem to increase in ductility with temperature, this nonetheless demonstrated that high values of ductility were possible in these coarse-grained alloys. The next step was to affirm that this trend followed that shown in Figures 2.16 and 2.18.

CHAPTER 5

DISCUSSION

This chapter is divided into four main sections, each of which will discuss specific aspects of the results presented in Chapter 4. The first section will analyze the serrated stress vs. strain as well as the stress vs. temperature behavior exhibited by the three alloys investigated in this study. The second section will address the strain rate vs. inverse temperature behavior of the alloys, in distinguishing the 'serration' vs. 'no serration' regimes as well as the activation energies for the appearance and disappearance of the serrations for each alloy. The third section will cover the strain rate sensitivity behavior, illustrating the negative strain rate sensitivity regime associated with the dynamic strain aging phenomenon and the corresponding region of abnormally high strain rate sensitivity. Finally, the fourth section will elaborate upon the enhanced ductility test results obtained in this study.

5.1   Stress vs. Temperature and Stress vs. Strain Behavior

5.1.1   Introduction

The dynamic strain aging phenomenon is primarily dependent on temperature and strain rate. Given that the Portevin-LeChatelier serrations are a direct indication of the occurrence of DSA, then these serrations are also strongly dependent on temperature and strain rate. When

testing in the negative strain rate sensitivity regime, the temperature dependence of the flow stress is the reverse of what is normally observed. This was depicted in Figures 2.5 and 2.7.

Dynamic strain aging is also dependent on the chemical constituents of the alloy in question in terms of the diffusivity of the solute species during deformation, which produce the solute atmospheres. In Figure 2.17, it was seen that low carbon steel yields a 'humped' stress-temperature curve and that the location of this 'hump' depends of the specific chemical addition, i.e. Cr, B or Ti. Consequently, the resulting strain rate sensitivity vs. temperature curves are also affected, as shown in Figure 2.18. The basic idea for selecting two super-pure binary Al-Mg alloys in this study was to ensure that Mg is the main reactant responsible for the DSA phenomenon. Thus, it was expected that the extra 2 wt% of Mg between the Al-3%Mg and Al-5%Mg alloys would affect the ensuing serrations.

As mentioned previously, the stresses experienced by DSA-prone alloys are high at low temperatures and decrease monotonically with increasing temperature in the normal way. However, at a temperature where solute diffusion is rapid enough to initiate DSA activity at a given test strain rate (which is assumed to be fixed), solute-dislocation clouds begin to form. In other words, diffusion of the solute atoms at this DSA peak temperature is such that their velocity is comparable to that of the mobile dislocations. At this point - as depicted by 'A' in Figure 2.5 - the stresses observed begin to *increase* with increasing temperature as larger applied forces are required during deformation in order for the dislocations to break free from their solute clouds.

The increase in stress reaches a peak, after which it decreases. At this peak, solute-dislocation clouds are forming much more frequently than at other temperatures, for the given strain rate. At temperatures beyond this DSA peak temperature, the solute atoms move too quickly to effectively pin the mobile dislocations. An extension of the work presented in Figure 2.5 is given in Figure 5.1, where the peaks in curves 2 to 5 show increasing degrees of DSA, and curve 1 shows the 'baseline' pure metal behaviour (i.e no DSA).
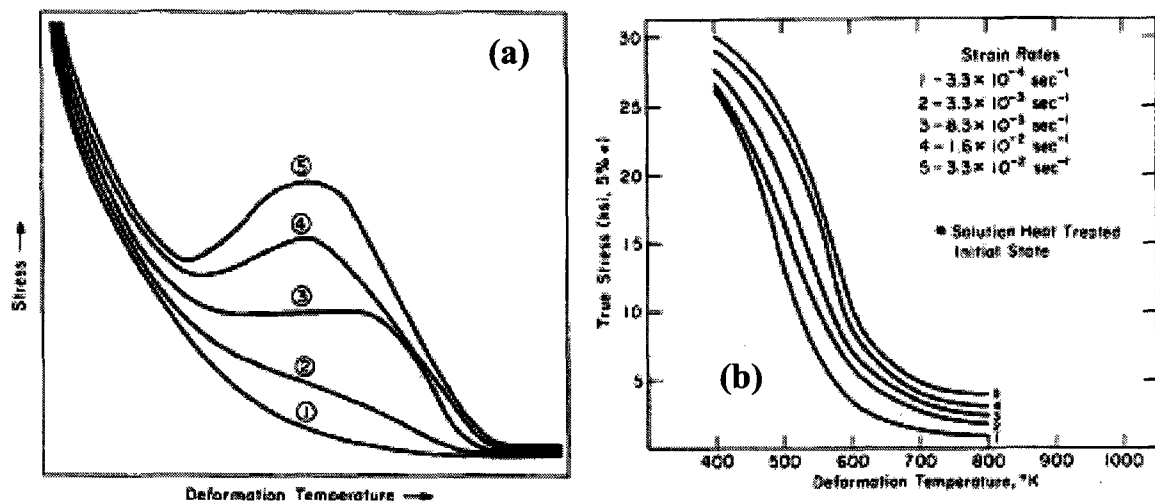
Figure 5.1. **Flow stress vs. temperature curves for (a) a DSA-prone Al alloy and (b) 5086 Al alloys at hot working tempertures [43].**

As can be seen, the 'hump' formed in Figure 5.1(a) changes with the degree of DSA taking place in the material during deformation. Also, at high temperatures and very low strain rates (Figure 5.1(b)), the DSA regime has been crossed and the resulting family of curves is smooth.

Finally, the 'humped' stress vs. temperature curve for a material that is prone to DSA will shift to higher/lower temperatures with an increase/decrease in strain rate. This is shown in

Figure 5.2. As the strain rate is increased (e.g. $\dot{\varepsilon}_1$ to $\dot{\varepsilon}_2$ or $\dot{\varepsilon}_1$ to $\dot{\varepsilon}_3$) or decreased (e.g. $\dot{\varepsilon}_3$ to $\dot{\varepsilon}_1$ or $\dot{\varepsilon}_2$ to $\dot{\varepsilon}_1$), there is a resulting change in the negative rate sensitivity regime, coupled with a change in the higher-than-normal rate sensitivity peak. Although the actual values of 'm' depend on the logarithm of the stresses observed, plotting the rate sensitivity as a function of temperature would yield a family of curves similar to those shown in Figure 2.19(a)-(c), but shifted either to the left/right of the temperature scale as a function of decreasing/increasing the strain rate.
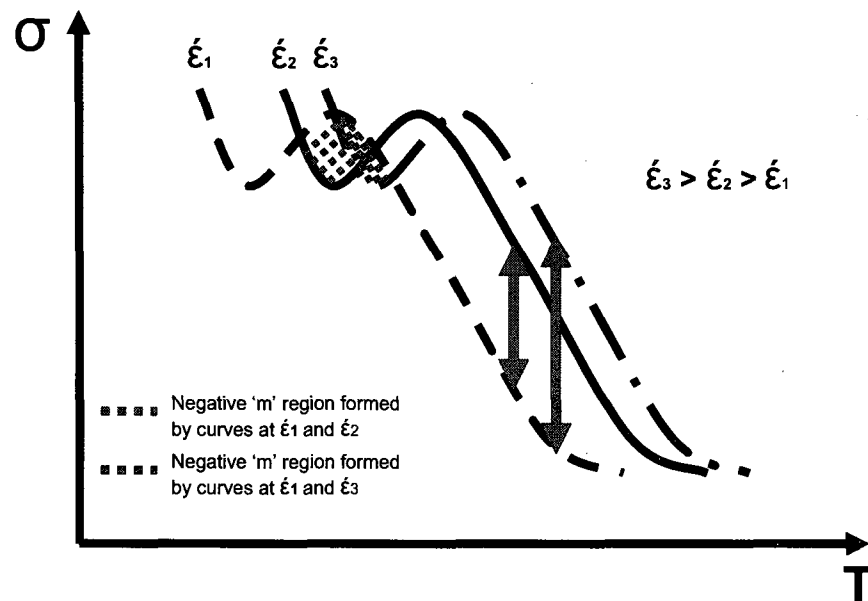
Figure 5.2.   **Schematic of the shift in the flow stress vs. temperature curves with changing strain rates and the resulting change in the negative rate sensitivity and higher-than-normal rate sensitivity areas.**

5.1.2   Serrations in the Present Study

In the present study, the temperature was varied in each alloy for a given strain rate. Therefore, the Mg content and strain rate parameters may be considered as 'fixed' and the

resulting DSA-prone stress-strain curves are then directly related to the change in temperature across the DSA regime. As could be seen from Figures 4.5, 4.7, 4.9, 4.11, 4.13, 4.15, 4.17, 4.19 and 4.21, the serrations observed in the alloys varied greatly as the temperature was increased for a given strain rate. The serration types observed in Chapter 4 are given in Table 5.1.

Table 5.1   Serration Types Observed in the Present Study

Alloy	Strain Rate (s^{-1})	Serration Typed Observed
Al-3%Mg	$10^{-3}\,s^{-1}$	Steps at -25°C (i.e. Type D or A) with Type E at higher strain; Type A at 0°C with Types B and C at higher temperatures
Al-3%Mg	$10^{-2}\,s^{-1}$	Steps at lower temperatures (i.e. Type A or D), Type A at 50°C and Types B and C at higher temperatures
Al-3%Mg	$10^{-1}\,s^{-1}$	Type A at 50°C; Types B and C at higher temperatures
Al-5%Mg	$10^{-3}\,s^{-1}$	Steps at -25°C (i.e. Type A or D), Type A at 0°C, Type B at 25°C and Type C at 50°C
Al-5%Mg	$10^{-2}\,s^{-1}$	Type E at -25°C, Type A at 25°C, Type B at 50°C and Type C at 75°C and 100°C
Al-5%Mg	$10^{-1}\,s^{-1}$	Steps at lower temperatures (i.e. Type A or D); Type A at 25°C, Type B at 50°C and 75°C, and Type C at 100°C
AA 5056	$10^{-3}\,s^{-1}$	Type A at -25°C and 0°C; Type C at 25°C and 50°C
AA 5056	$10^{-2}\,s^{-1}$	Type A at 0°C ('steps'), Type A at 25°C and Type C at 50°C and 75°C
AA 5056	$10^{-1}\,s^{-1}$	Steps at 25°C (i.e. Type A or D), Type A at 50°C with some Type B, Type C at 75°C and 100°C (4 steps at start of curve)

It should be noted that the stress-temperature curves for Al-3%Mg, Al-5%Mg and AA 5056 shown in Chapter 4 were plotted to stresses (at 10% strain) of 175, 225 and 275 MPa, respectively. This is because the peak strengths obtained varied with the alloy tested. Changing the stress scales emphasizes the 'hump's that are formed in the stress-temperature curves of the respective alloy.

Knowing that a certain number of dislocations are generated at the strain rate being applied, an increase in temperature in the DSA regime will increase the diffusivity of the solute

atoms, and in this way enable them to form solute-dislocation clouds more easily. Once the peak in serration activity has occurred, however, as in Figure 4.11 for Al-5%Mg at 50°C and a strain rate of 10^{-3} s^{-1}, any further increase in temperature will make the diffusing solute atoms too mobile to effectively pin the moving dislocations. As a result, with respect to Figure 4.11, the resulting stress-strain curves at all temperatures beyond 50°C will be smooth. Similarly, at too low a temperature, the solute atoms will be too slow to catch up with the moving dislocations during deformation. Therefore, serration activity in terms of the observed stress drops will increase with temperature for a given strain rate.

Moreover, stress drops will increase with strain at a given temperature and strain rate. This has been studied by many; an illustration is given in Figure 5.3, and an example of this in the present work for Al-5%Mg is presented in Figure 5.4.
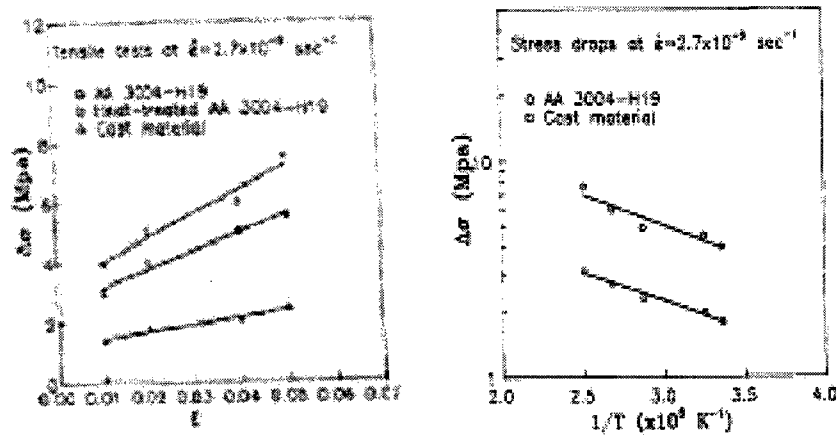
Figure 5.3. (a) Strain dependence and (b) temperature dependence of stress drops in a 3004 Al alloy at a strain rate of 2.7×10^{-5} s^{-1} [112].
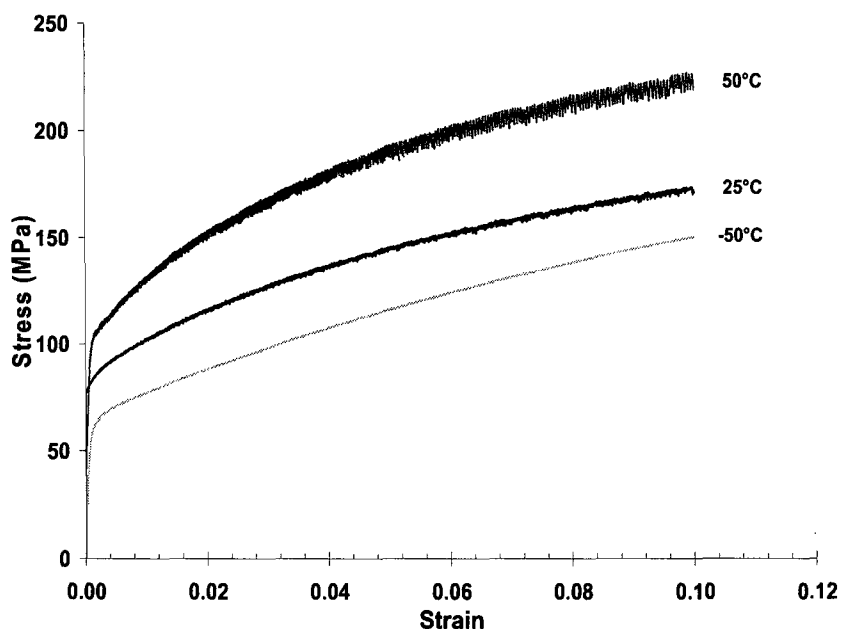
Figure 5.4.   Increase in amplitude of stress drops in Al-5%Mg with temperature and strain, at a strain rate of 10^{-3} s^{-1}.

As can be seen, the amplitude of the DSA stress drops increases with strain. This is most evident at 50°C. The intensity of the serrations in terms of stress drops visibly increases with temperature from -50°C to 25°C to 50°C.

As the strain rate is being increased, more and more dislocations are being formed during deformation. That is to say, for the same amount of strain required in a tensile test - in this case, 10% - the deformation occurs at a quicker rate and the peak stress observed will be greater than observed at a lower strain rate. However, within the DSA regime, the stresses experienced at a given temperature are *higher* at a lower strain rate. In other words, this is the opposite of what is normally expected. The reason for this is that, at lower strain rates, the diffusing solutes have more time to pin the dislocations that are formed as the material is strained. The consequence of this is a region of negative strain rate sensitivity.

This was evident in Figures 4.11 and 4.13, for example, where it could be seen that at 50°C, the stress drops are much larger at 10^{-3} s^{-1} than at 10^{-2} s^{-1}. Larger stress fluctuations indicate that higher applied stresses are required for the trapped dislocations to break free. Thus, stresses felt at a given temperature in the DSA regime are greater at lower strain rates than at higher strain rates (at a fixed temperature), resulting in a region of negative strain rate sensitivity.

5.1.2.1 Parasite Serrations

It was observed in the tensile test work of Thevenet *et al.* [113] and Abbadi *et al.* [114] that 'parasite' serrations/load drops can occur in the uniform deformation portion of a stress-strain curve for a material that is out of the DSA regime or prior to the onset of serrations (provided, these serrations do not begin immediately after yielding). These serrations are not related to DSA, but rather, the outcome of a rough sample surface following the rolling of the metal to its final sheet form. This, in turn, can result in the possible nucleation of deformation bands [114]. These fluctuations in the otherwise smooth stress-strain behavior can be misinterpreted as Type C ("unlocking") serrations. A comparison of the behaviours of a polished to an unpolished sample, as given in Figure 5.5, reveals that these serrations are indeed not the result of DSA.
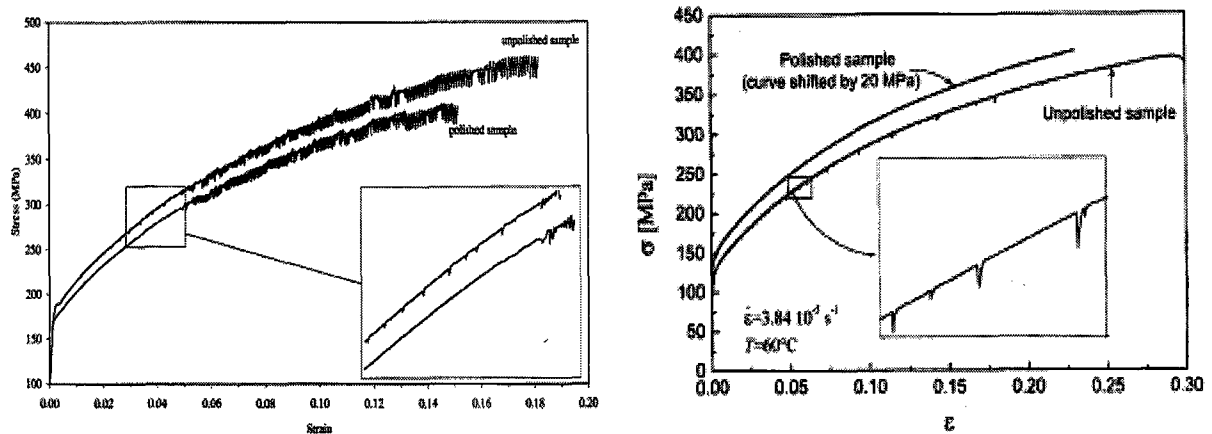
Figure 5.5. (a) Stress-strain curves for polished and unpolished Al-Zn-Mg-Cu alloy samples (the unpolished sample is shifted up by 15 MPa) [113] and (b) stress-strain curves for polished and unpolished 5182 Al alloy samples (the unpolished sample is shifted up by 20 MPa) [114].

It can be seen that, with the exception of the presence of the parasite serrations in the unpolished sample, the two serrated stress-strain curves in Figures 5.5(a) and 5.5(b) are otherwise identical in appearance. It is interesting to note that, regardless of the sample surface, the DSA serrations that form in Figure 5.5(a) are still more pronounced when they occur at the critical strain. However, the exact determination of the critical strain may be biased by the presence of such parasite serrations. The situation presented above is more evident in stress-strain curves where serrations may be delayed to a strain beyond that being recorded or in cases where the curves are out of the DSA regime. In the latter case (as shown in Figure 5.5(b)), an otherwise smooth curve shows load drops that may in turn be misinterpreted as Type C DSA serrations. Parasite serrations have been observed in the present work in the AA 5056 alloy. An example of this occurs at 50°C and a strain rate of 10^{-3} s^{-1} and is shown in Figure 5.6.
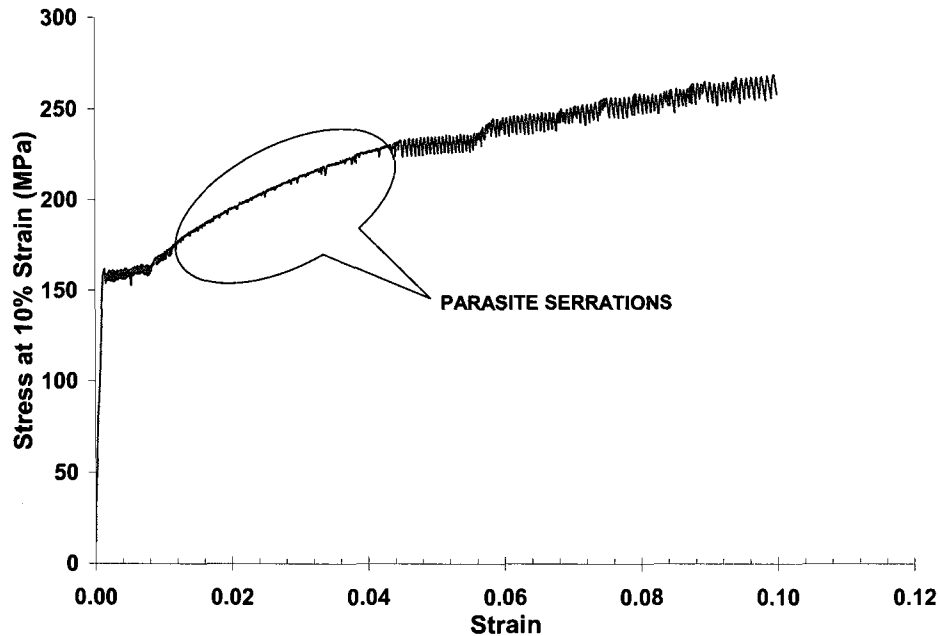
Figure 5.6. Stress-strain curve for AA 5056 at 50°C and a strain rate of 10^{-3} s^{-1} demonstrating the occurrence of parasite serrations.

It should be noted that the standard tensile and superplasticity tensile samples were fine-ground using 800 and 1200 grit grinding paper to remove surface scratches. Nevertheless, the serrations due to DSA in Figure 5.6 are more pronounced than the parasite serrations preceding the onset of the true DSA serrations.

5.1.3   Negative Strain Rate Sensitivity in Al-3%Mg

Consider the Al-3%Mg alloy shown in Figures 5.7 and 5.8, where the 'humped' curves corresponding to each of the three strain rates used are distinct and the areas of negative strain rate sensitivity are visible. In Figure 5.7, stresses in the negative strain rate sensitivity region are higher at 10^{-3} s^{-1} than at 10^{-2} s^{-1}. Similarly, in Figure 5.8, stresses in the negative strain rate sensitivity region are higher at 10^{-2} s^{-1} than at 10^{-1} s^{-1}.
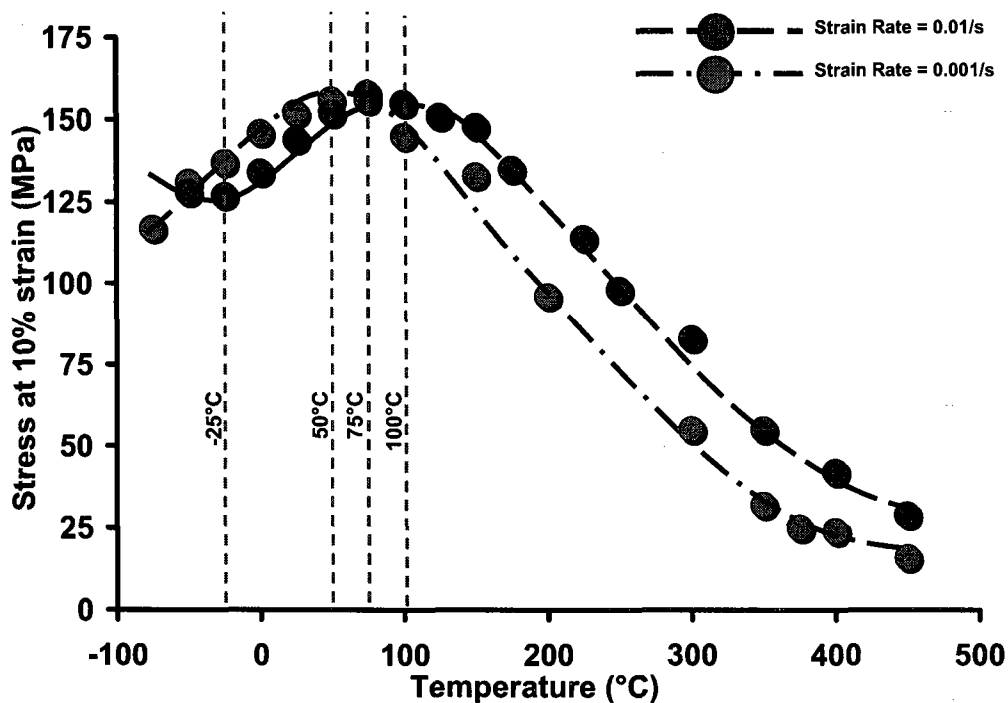
Figure 5.7.   Stress vs. temperature curves for Al-3%Mg for strain rates of 10^{-3} s^{-1} and 10^{-2} s^{-1}.
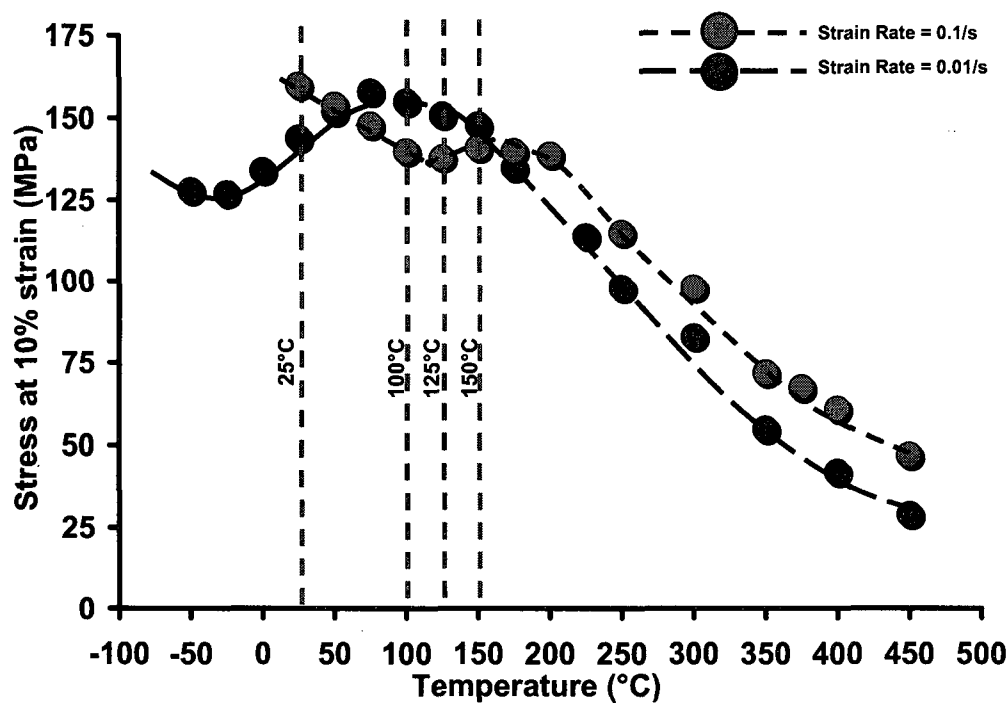
Figure 5.8.   Stress vs. temperature curves for Al-3%Mg for strain rates of 10^{-2} s^{-1} and 10^{-1} s^{-1}.

By selecting temperatures for comparison within and external to the negative strain rate

sensitivity regime, it can be seen that the stresses measured in the DSA regime are *higher* at the

lower strain rates. This is further illustrated in Figures 5.9 and 5.10, in which the actual serrations

observed at selected temperatures are given.
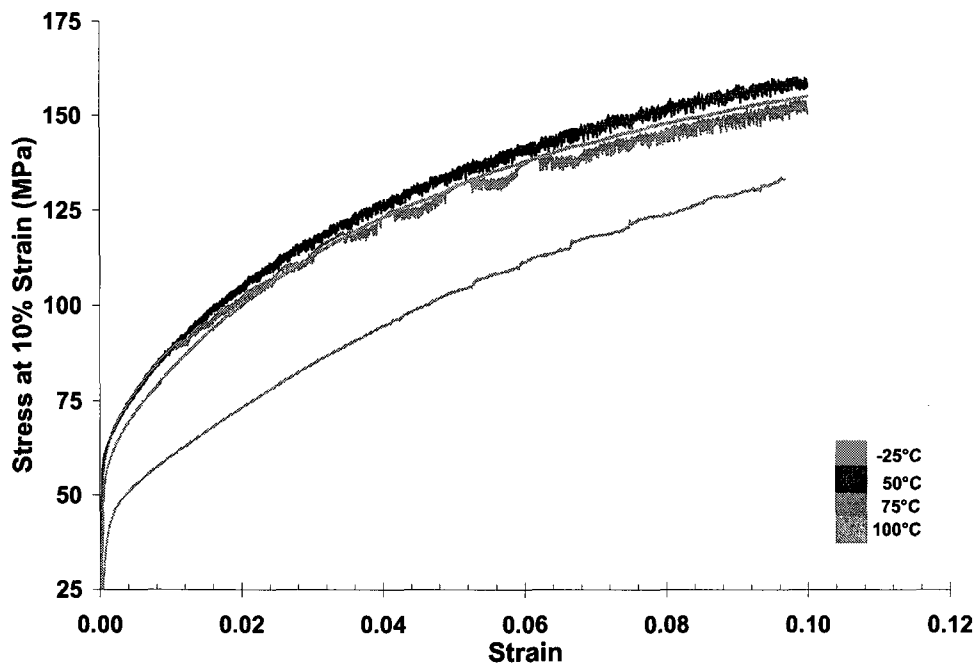
Figure 5.9.   **Stress vs. strain curves for selected temperatures for Al-3%Mg determined at a strain rate of 10^{-3} s^{-1}. The temperatures are those identified by vertical lines in Figure 5.7.**
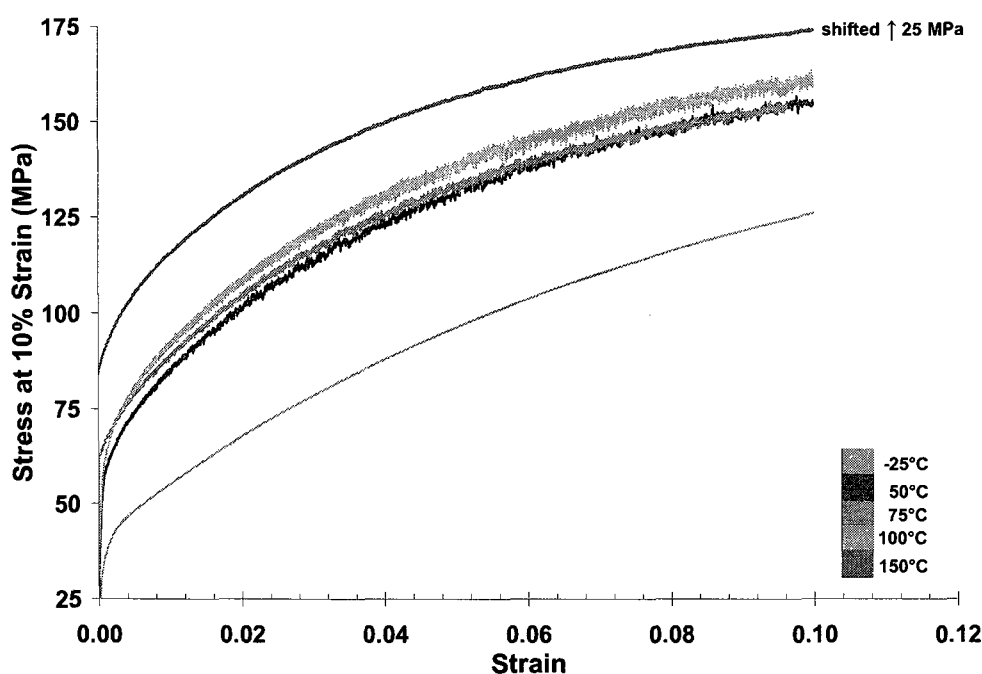
Figure 5.10. **Stress vs. strain curves for selected temperatures for Al-3%Mg determined at a strain rate of 10^{-2} s^{-1}. The temperatures are those identified by vertical lines in Figure 5.7.**

As was seen in Figure 5.7, the measured stresses at -25°C and 50°C were higher at 10^{-3} s^{-1} than at 10^{-2} s^{-1}. In support of this, the -25°C curve in Figure 5.9 exhibits step-like serrations at a critical strain of about 0.05. However, in Figure 5.10, the stress-strain curve at -25°C and 10^{-2} s^{-1} is smooth. Thus, serrations at the higher strain rate do not appear until a temperature higher than -25°C is reached. Moreover, the stresses at 75°C in Figure 5.7 are comparable at 10^{-3} s^{-1} and 10^{-2} s^{-1}, indicating that the end of the negative strain rate sensitivity regime defined by these two strain rates is being approached. However, it can be expected that the serration intensity will be greater at the lower strain rate. Consequently, the stress-strain curves corresponding to 75°C in Figures 5.9 and 5.10 show larger fluctuations at 10^{-3} s^{-1} than at 10^{-2} s^{-1}.

At 100°C, the stresses shown in Figure 5.7 are now greater at 10^{-2} s^{-1} rather than at 10^{-3} s^{-1}. Moreover, the data point in Figure 5.7 corresponding to 100°C and 10^{-3} s^{-1} occurs *after* the DSA peak. Thus, as expected, the corresponding curve in Figure 5.9 is smooth, with no indication of DSA serrations, while that at 100°C and 10^{-2} s^{-1} in Figure 5.10 displays very large fluctuations. It should be pointed out that both the stress-strain curve for 50°C at 10^{-3} s^{-1} in Figure 5.9 as well as the curve for 100°C at 10^{-2} s^{-1} in Figure 5.10 correspond to the DSA peaks (i.e. the serrations are at their maxima for the given strain rate) at 10^{-3} s^{-1} and 10^{-2} s^{-1}, respectively. Further comparison within and external to the negative strain rate sensitivity regime, at strain rates of 10^{-2} s^{-1} and 10^{-1} s^{-1}, and corresponding to the vertical temperature lines in Figure 5.8 can be found in Figures 5.11 and 5.12.
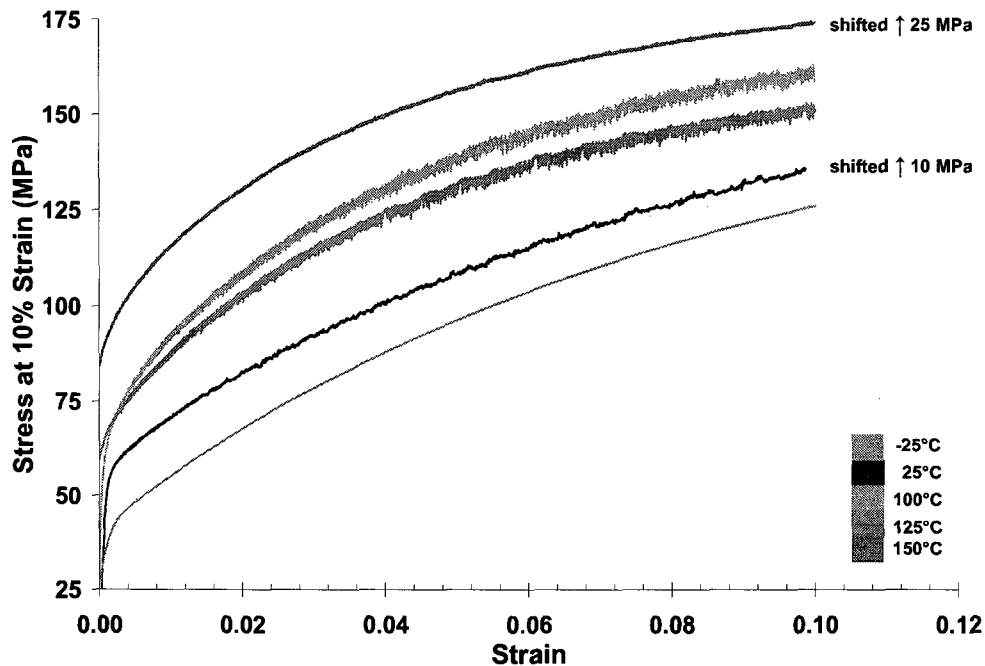
Figure 5.11.   Stress vs. strain curves for selected temperatures for Al-3%Mg determined at a strain rate of 10^{-2} s^{-1}. The temperatures are those identified by vertical lines in Figure 5.8.
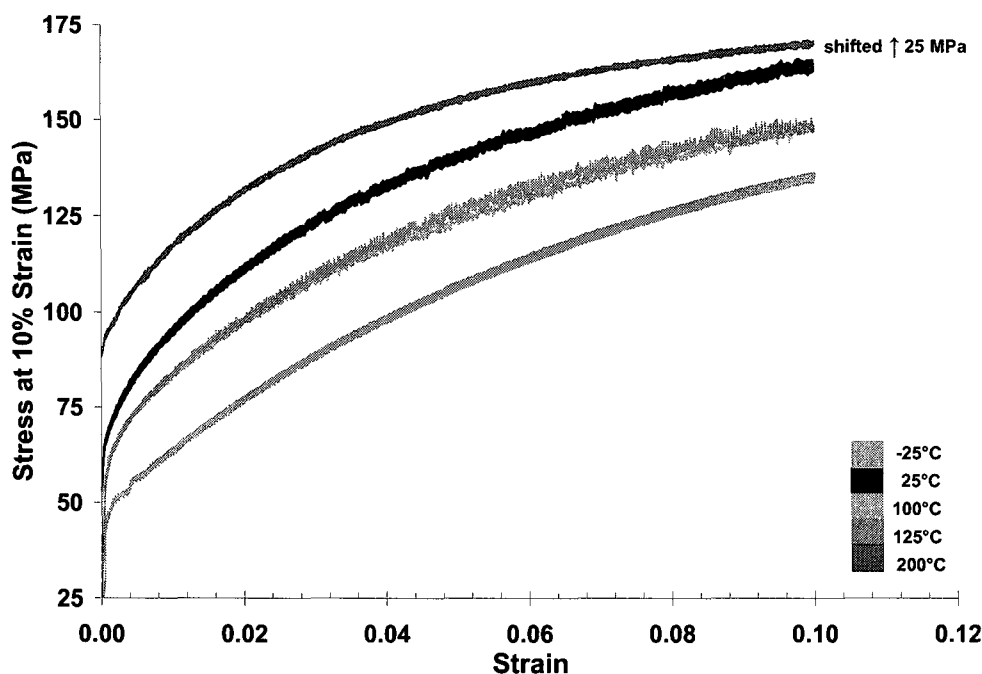
Figure 5.12. **Stress vs. strain curves for selected temperatures for Al-3%Mg determined at a strain rate of 10^{-1} s^{-1}. The temperatures are those identified by vertical lines in Figure 5.8.**

As can be seen from Figure 5.8, the stress-temperature curves for 100°C and 125°C at 10^{-2} s^{-1} are *higher* in stress than at 10^{-1} s^{-1}. At 100°C, the curve presented in Figure 5.11 exhibits larger stress fluctuations than those observed in Figure 5.12 and a higher recorded stress value at 10% strain. At 125°C, the curve presented in Figure 5.11 exhibits stress drops that are comparable to those shown in Figure 5.12 as well as a higher recorded stress value at 10% strain. At 25°C, the stress at 10^{-1} s^{-1} is higher than at 10^{-2} s^{-1}, as shown in Figures 5.8 and 5.12.

5.1.4   Negative Strain Rate Sensitivity in Al-5%Mg and AA 5056

The stress vs. temperature curves given in Figures 4.23 and 4.24 for Al-5%Mg and AA 5056, respectively, have negative strain rate sensitivity regimes that are not as distinct as in the

case of Al-3%Mg. Nevertheless, serrations were also observed in these two alloys and the

presence of the 'humps' in Figures 4.23 and 4.24 and their characteristics demonstrate that the

curves do shift to higher temperatures as the strain rate is increased. The negative strain rate

sensitivity behaviors of the Al-5%Mg and AA 5056 alloys are shown in Figures 5.13 and 5.14,

respectively, in the form of stress vs. strain rate curves.
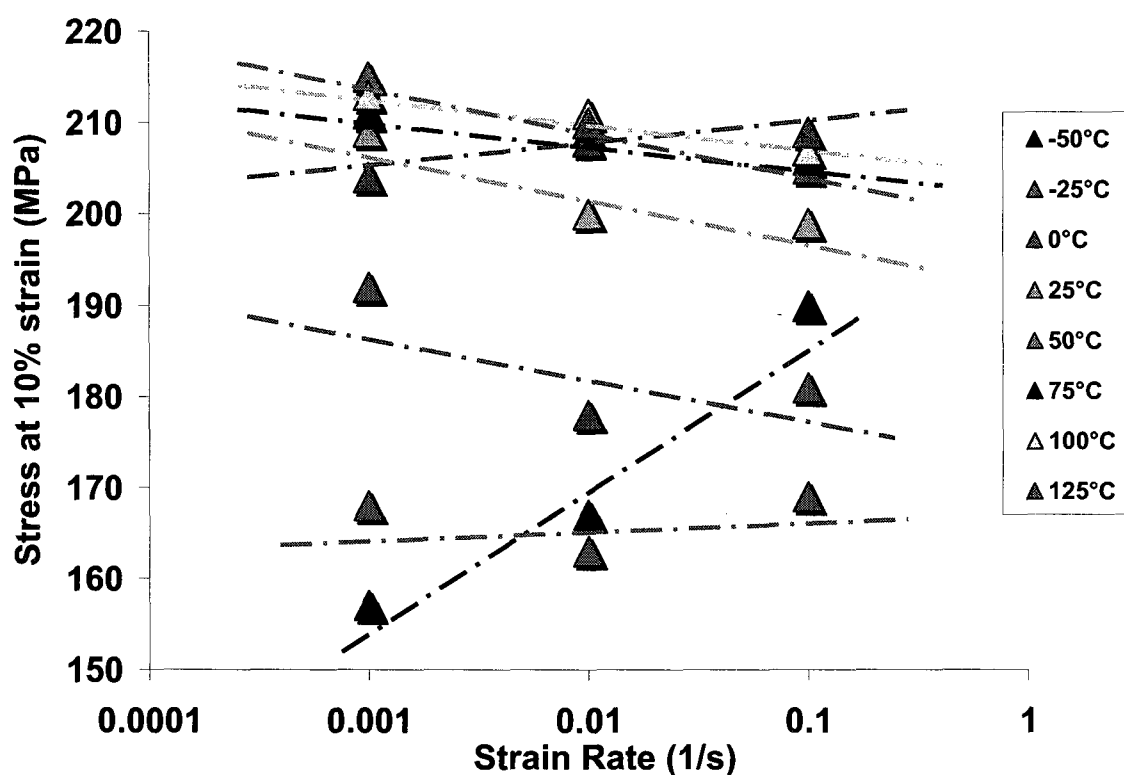
Figure 5.13. **Stress vs. strain rate curves for Al-5%Mg at selected temperatures surrounding the DSA regime.**
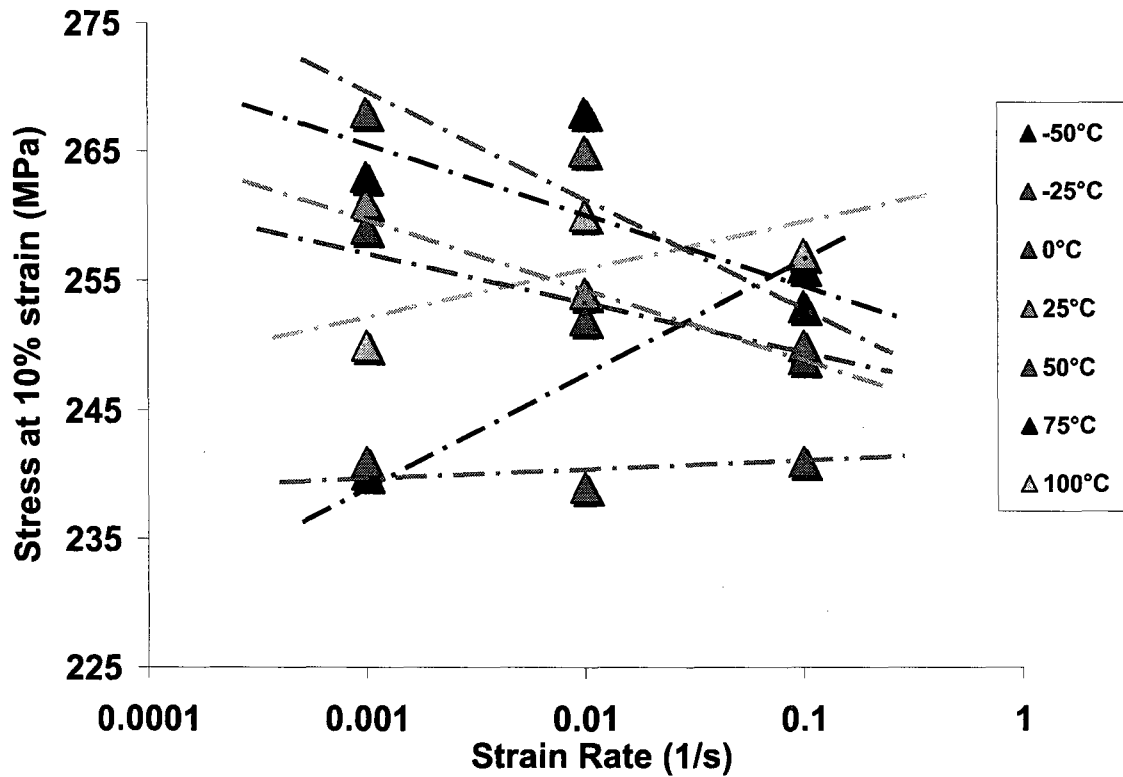
Figure 5.14. Stress vs. strain rate curves for AA 5056 at selected temperatures surrounding the DSA regime.

In Figure 5.13, the data series given at -50°C and 125°C have positive slopes for their best-fit lines. This means that the stress increases with the strain rate, which makes sense since these two temperatures are outside the DSA regime. However, at all intermediate temperatures, i.e. *within* the DSA regime, the slopes for the remaining best-fit lines are negative. Likewise, in Figure 5.14, the data series pertaining to -50°C and 100°C have positive slopes for their best-fit lines. Consequently, the stresses at these temperatures increase with strain rate, seeing as how these temperatures are again outside the DSA regime. At all intermediate temperatures, i.e. *within* the DSA regime, the slopes for the remaining best-fit lines are negative.

The serration intensity is greater in the AA 5056 than in the Al-5%Mg alloy. In other words, the fluctuations are greater in the commercial alloy than in the super-pure binary Al-5%Mg alloy. This may be attributed to the extra alloy additions and residuals present in the commercial alloy, which apparently contribute to dislocation locking during the negative strain rate sensitivity regime. Given that the two alloys contain the same amount of Mg and that this solute is the primary reactant in the solute-dislocation interaction during dynamic strain aging, it seems reasonable to conclude that the other alloying and impurity elements are also playing a role in producing the serrated stress-strain curves observed.

In his tensile tests, Morris [31] compared the behavior of a binary Al-5%Mg alloy with that of a ternary alloy containing 0.4 wt% Mn. He found that the ternary alloy displayed an increase in the intensity of the DSA serrations, along with added strength. Similarly, in the work of Fujita and Tabata [95], the serration intensity was greater in alloys of finer grain size and higher Mg content. Therefore, it appears likely that the difference in grain size between the AA 5056 and Al-5%Mg, along with the added alloying elements in the commercial AA 5056 alloy, result in the AA 5056 having more pronounced serrations than either the Al-3%Mg or the Al-5%Mg. Moreover, the higher Mg content in the AA 5056 will alone ensure that the serrations are more prominent when compared to the Al-3%Mg. According to Chinh *et al.* [115], as little as 0.62 wt% Mg is enough for DSA serrations to appear in binary Al-Mg alloys at room temperature.

Thomas [84] examined the tensile deformation behavior of Al-Mg alloys subject to DSA and plotted the critical stress required for dislocation breakaway from a solute cloud as a

function of grain size. The critical stress was found to decrease with increasing grain size. Therefore, although both the Al-5%Mg and AA 5056 alloys contain a nominal Mg concentration of 5 wt%, the difference in grain size, along with the added elements in the AA 5056, result in the Al-5%Mg having smaller stress fluctuations than the AA 5056. Brindley and Worthington [116] and others [117-119] have reported that there is an increase in critical strain to the onset of serrations with increasing grain size. Nevertheless, Mukherjee et al. [120] have contradicted this finding in their work.

As mentioned previously, the work of Humphreys et al. [53] shows that the flow stress vs. temperature curves change for an alloy when elemental additions are made. However, the overall profile of the 'hump' is similar from alloy to alloy. This was shown in Figure 2.17 in Chapter 2, where it was seen that the 'humped' stress-temperature curve observed in low carbon steel is modified when additions of Cr, B and Ti are made. In the four steels tested, the 'hump' observed in each alloy was maintained across nearly the same width of temperature.

In the present study, the 'humped' curves formed in the Al-5%Mg and AA 5056 alloys were noted to be similar in shape at all three test strain rates, as shown in Figures 4.23 and 4.24. The negative rate sensitivity regimes were also similar in that they extended across nearly the same temperature range. The serration intensity in the Al-5%Mg and AA 5056 alloys is presented in Figures 5.15 to 5.20 for the prescribed strain rates, at selected temperatures. The serration behaviors in the Al-5%Mg and AA 5056 alloys at a strain rate of 10^{-3} s^{-1} is given in Figures 5.15 and 5.16, respectively. Yield point elongations were observed in Figure 5.16 for the AA 5056 alloy.
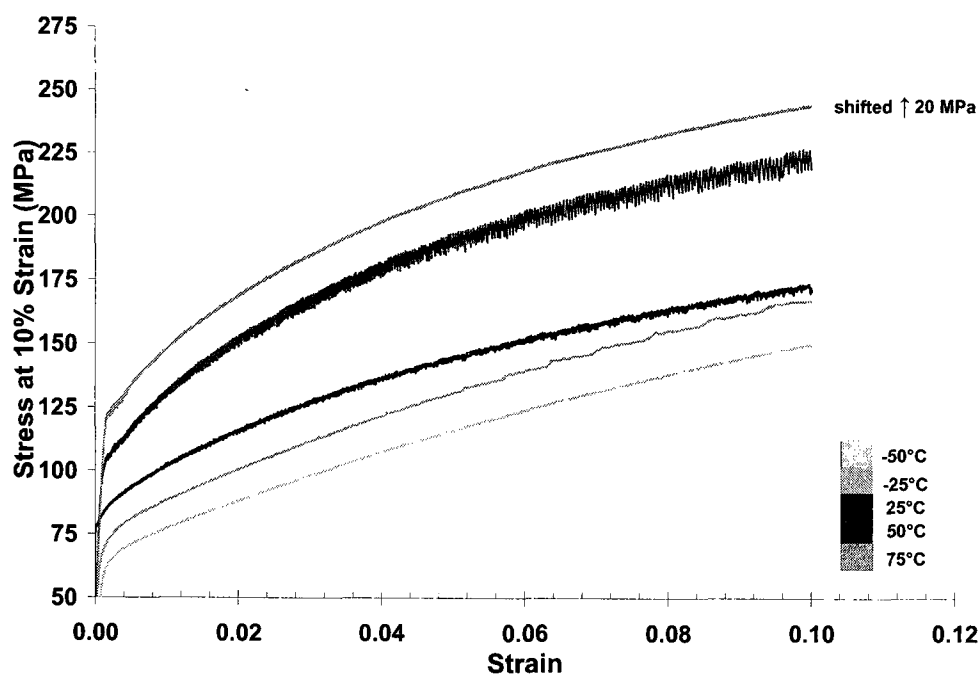
Figure 5.15. Stress vs. strain curves for Al-5%Mg determined at a strain rate of 10^{-3} s^{-1} and selected temperatures.
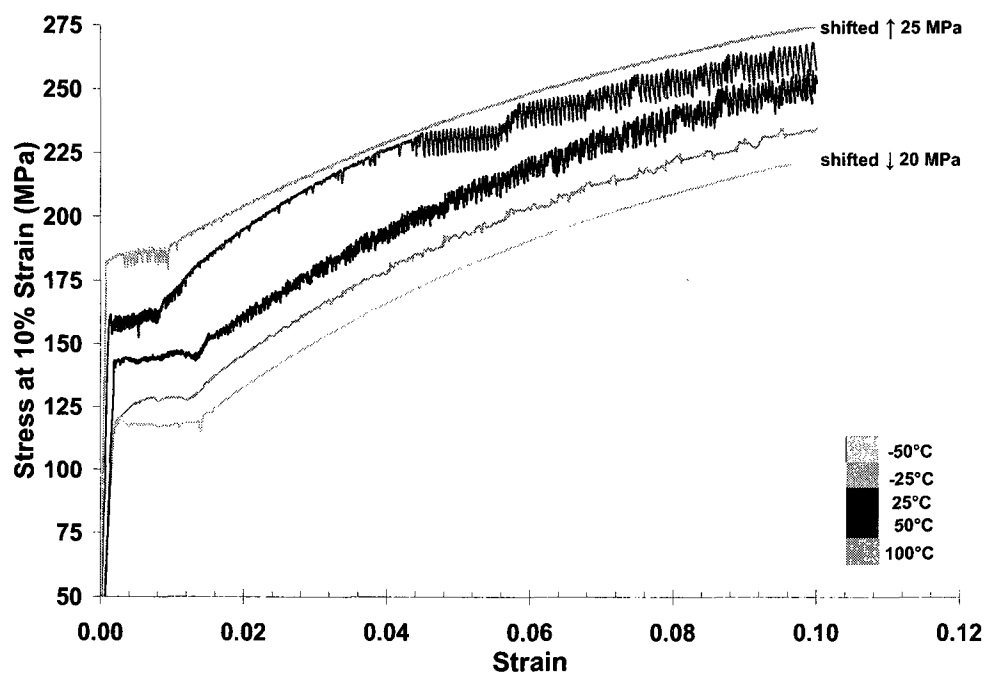
Figure 5.16. Stress vs. strain curves for AA 5056 determined at a strain rate of 10^{-3} s^{-1} and selected temperatures.

As can be seen from Figures 5.15 and 5.16, no serrations form at -50°C in either material. At -25°C, serrations begin to form as steps in the Al-5%Mg alloy, yet appear at a lower critical strain in the AA 5056 alloy. Moreover, the strain interval for each step is much smaller in the AA 5056 than in the Al-5%Mg, meaning that the serrations are produced at a higher rate.

The stress fluctuations exhibit much larger amplitudes at 25°C in the AA 5056 alloy, as is evident from Figure 5.16. This trend continues to 50°C, even though the stress fluctuations in the AA 5056 compared to the Al-5%Mg are not as marked as at 25°C.

Although the stress-strain curves for these two alloys are smooth at 75°C (Figures 4.11 and 4.17), the serration intensity in the AA 5056 is greater than in the Al-5%Mg in the negative rate sensitivity regime. The latter is defined by the appearance of the curves in Figures 5.15 and 5.16.

The serration behaviors in the Al-5%Mg and AA 5056 alloys at a strain rate of 10^{-2} s^{-1} is given in Figure 5.17.
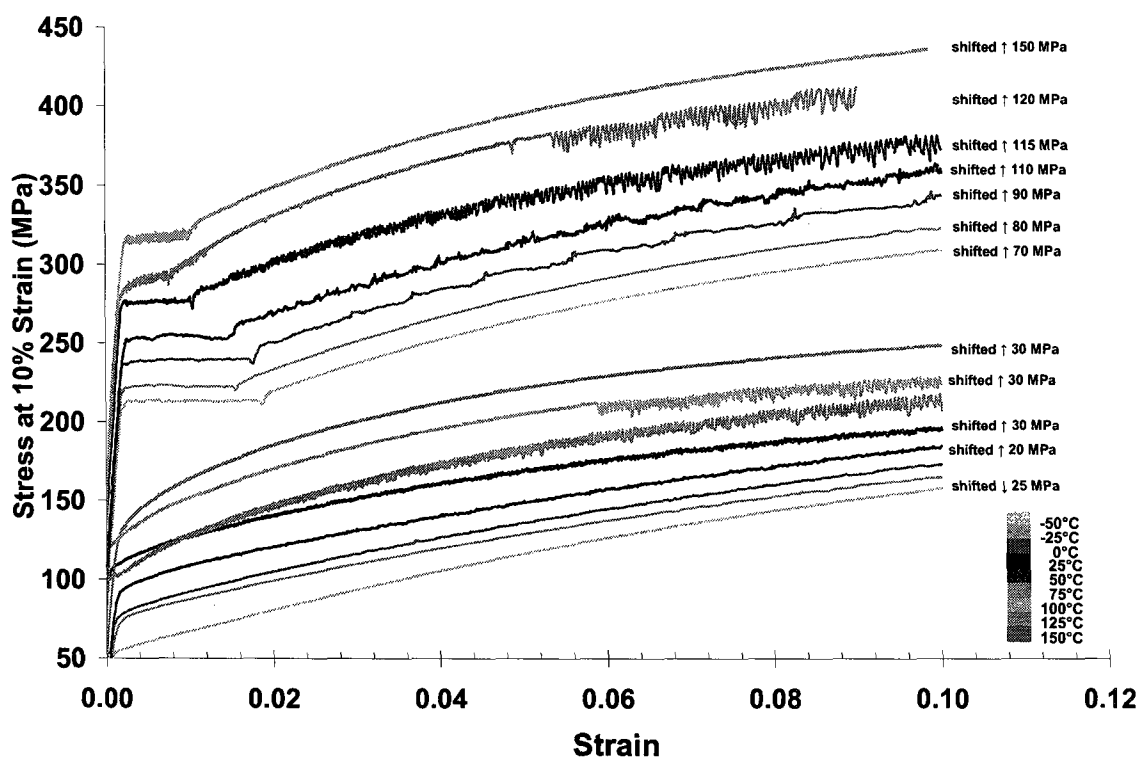
Figure 5.17.   Stress vs. strain curves for Al-5%Mg (bottom) and AA 5056 (top) determined at a strain rate of 10^{-2} s^{-1} and selected temperatures.

As can be seen from Figure 5.17, there are no serrations at -50°C and very few and faint serrations at -25°C in either alloy. Serrations in the Al-5%Mg alloy are also faint at 0°C, yet they begin to form as marked steps in the AA 5056 alloy, where the initial increase in stress for the formation of each subsequent step becomes more and more pronounced with strain.

The frequency at which serrations form as well as their magnitude are both greater in the AA 5056 than in the Al-5%Mg at 25°C, 50°C and 75°C. Although serrations do not occur at 100°C at 10^{-2} s^{-1} in AA 5056, and are delayed to a critical strain of nearly 0.06 in Al-5%Mg, nevertheless it is safe to conclude that the negative rate sensitivity regime has reached its end. Therefore, one may say that the serration intensity in the AA 5056 is greater than in the Al-

5%Mg in the negative rate sensitivity regime defined by the curves presented in Figure 5.17. As

with the case at 10^{-3} s^{-1} (Figure 5.16), yield point elongations were observed in Figure 5.17 for

the AA 5056 alloy.

The serration behaviors in the Al-5%Mg and AA 5056 alloys at a strain rate of 10^{-1} s^{-1} is

given in Figure 5.18.
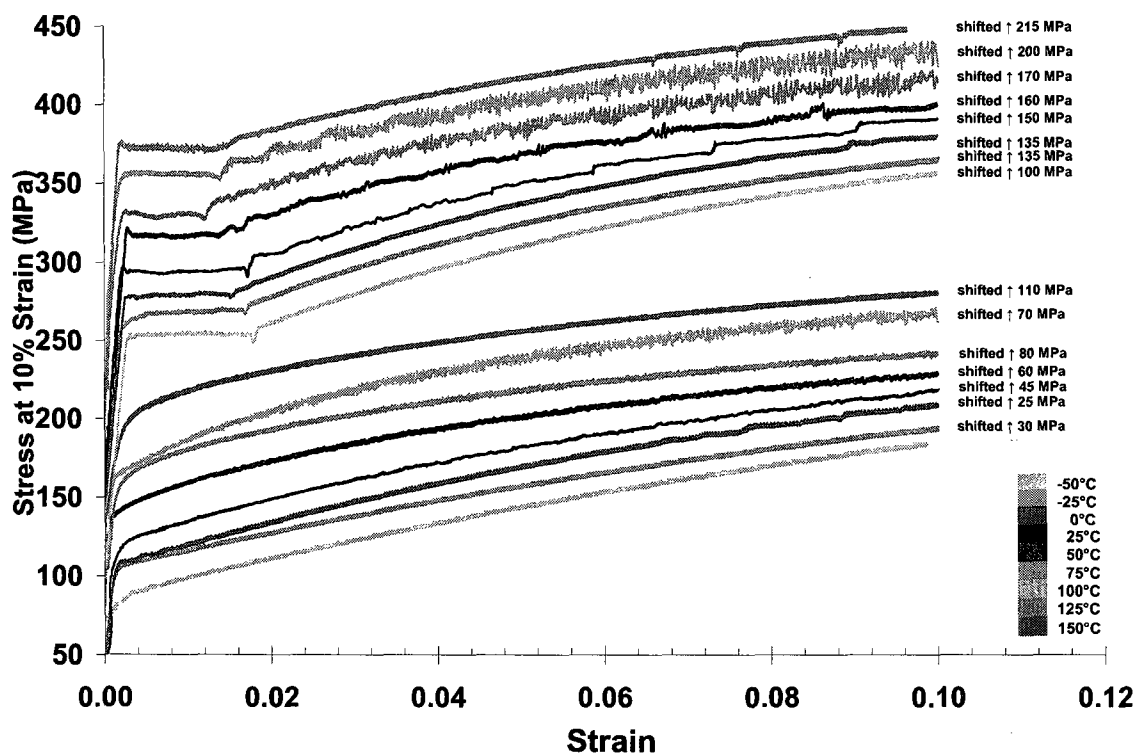
**Figure 5.18. Stress vs. strain curves for Al-5%Mg (bottom) and AA 5056 (top) determined
at a strain rate of 10^{-1} s^{-1} and selected temperatures.**

As can be seen from Figure 5.18, there are no serrations at -50°C or -25°C in either alloy.

The serration intensity in the Al-5%Mg alloy is noted to increase from 25°C to 50°C and 75°C.

The stress fluctuations are largest at 100°C. The serrations at 25°C and 50°C appear as marked

steps in the AA 5056 alloy, where, again, it is seen that the initial increase in stress for the

formation of each subsequent step becomes more and more pronounced with strain.

The frequencies at which the serrations form as well as their magnitudes at 75°C and

100°C are both greater in the AA 5056 than in the Al-5%Mg. Unless serrations occur at 125°C in

the Al-5%Mg alloy with comparable stress drops as at 100°C at 10^{-1} s^{-1}, it is reasonable to

assume that the negative rate sensitivity regime has reached its end. Thus the serration intensity

in the AA 5056 is greater than in the Al-5%Mg in the negative rate sensitivity regime, where the

latter is defined by the shapes of the curves in Figure 5.18. As with the AA 5056 curves shown at

10^{-3} s^{-1} (Figure 5.16) and 10^{-2} s^{-1} (Figure 5.17), yield point elongations were observed in Figure

5.18 for the AA 5056 alloy. These yield plateaus will be explored more closely in the following

section.

5.1.4.1   Yield Point Elongations in AA 5056

As could be seen in Figures 5.16 to 5.18, the AA 5056 alloy exhibited a yield point

elongation (YPE) region prior to the onset of work hardening. It therefore appears that static

strain ageing had occurred prior to plastic deformation and that the dislocations had become

locked. Contrary to the yield point phenomena occurring in interstitial alloy systems, larger

amounts (in wt%) of solute are required in substitutional alloys to develop a pronounced yield

drop effect [98]. Moreover, the interaction energy between solute atoms and dislocations is much

less for substitutional atoms (e.g. the Mg, Cr, Fe, Mn and Si in the AA 5056) than for interstitial

atoms (e.g. C and N in iron) [121]. However, in the commercial AA 5056 alloy, with its

additional alloying elements, it appears that dislocation locking had occurred prior to plastic deformation.

According to Brindley and Worthington [98], the critical parameters affecting the formation of YPE's are temperature, strain rate, composition and grain size. From the work of Inagaki et al. [122] on the influence of temperature, strain rate and grain size on YPE's in Al-Mg alloys, it was found that the YPE's decreased with increasing temperature and grain size and increased with Mg content. Moreover, they increased linearly with strain rate. This agrees with the earlier findings of Brindley and Worthington.

At very large grain sizes, most of the grains in the material have deformed by the time the upper yield point is reached; moreover, no macroscopic yield drop occurs and it becomes very difficult to detect any difference between the upper and lower yield points [98, 123]. As can be seen from Figures 4.17, 4.19 and 4.21, the YPE's occurring in AA 5056 are flat plateaux with no distinct upper yield point. At a sufficiently coarse grain size, the YPE effect disappears. Consequently, the stress-strain curves for the coarse-grained binary Al-3%Mg and Al-5%Mg in Chapter 4 display no visible YPE's. Inagaki et al. [122] observed the disappearance of YPE's in Al-Mg alloys beyond a grain size of ~150 μm. Similarly, no YPE's were observed in the work of Fujita and Tabata [95] on DSA in binary Al-Mg alloys in the temperature range -196°C (77 K) to 20°C (293 K).

In the present work, YPE's were observed at all strain rates in the AA 5056 DSA range and it is known that the grain size in AA 5056 was much finer than in either the Al-3%Mg or Al-

5%Mg. At all strain rates, the YPE's are relatively constant in 'length' at the lower temperatures, yet eventually decrease with increasing temperature. This is evident at strain rates of 10^{-3} s^{-1} (Figures 4.17 and 5.16) and 10^{-2} s^{-1} (Figures 4.19 and 5.17). At a strain rate of 10^{-1} s^{-1} (Figures 4.21 and 5.18), the YPE's observed are relatively constant, yet there is a clear decrease at 150°C. It is also interesting to note that at 150°C and 10^{-1} s^{-1}, there are no DSA serrations, but a YPE is still present. Also, the YPE's at 75°C and 10^{-3} s^{-1} and 10^{-2} s^{-1} are not as evident as at 10^{-1} s^{-1}.

Another point of interest raised by Thomas [84] is that slow cooling from an elevated solution treatment temperature develops an "extra region of uneven yielding", in reference to the YPE that precedes the work hardening portion of the stress-strain curve in the DSA regime. It is possible that a time delay between the removal of the AA 5056 samples and the start of the water quench resulted in the occurrence of static strain aging. Given the absence of other alloying elements and the much larger grain sizes in the binary Al-3%Mg and Al-5%Mg alloys, such a time delay would not result in any noticeable YPE's on a stress-strain curve. Moreover, Thomas [84] observed that YPE's are independent of the occurrence of jerky flow afterward. An example of this is shown in Figure 4.17 at 100°C, where the stress-strain curve following the YPE is smooth.

In the work of Lloyd et al. [124] on AA 5182 alloy, it was observed that a water quench from a solution heat treatment temperature of 500°C resulted in the lower curve of Figure 5.19. However, a quench in air from 500°C, or either in air or water from a temperature below 500°C, gave rise to the upper curve. Moreover, Robinson and Shaw [125] observed YPE's in the stress-strain curves of AA 5182 after annealing at 300°C for 0.5 hours. This is an interesting point,

considering the solution heat treatment temperature used for the standard tensile test samples was

450°C, followed by a water quench.
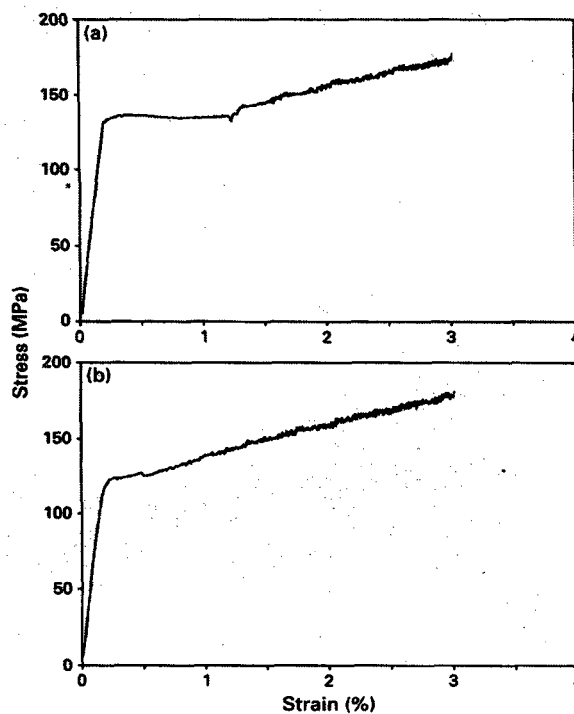
Figure 5.19. Stress vs. strain curves for AA 5182 after being quenched in air (top) and water (bottom) from a solution heat treatment temperature of 500°C [124].

Lloyd *et al.* [124] also observed that the extent of Lüdering was dependent on the grain

size (decreasing with increasing grain size), but that it was also dependent on the processing

route used to generate that grain size. It has been suggested that YPE's can occur from prior

deformation [126]; however, this was not the case in this work.

Finally, the additional alloying elements found in the AA 5056 alloy (Cr (0.13 wt%), Fe

(0.042 wt%), Mn (0.091 wt%) and Si (0.037 wt%)) may also have contributed to the static strain

aging just as they can to dynamic strain aging. These alloying elements have solubility limits at

450°C (the solution temperature) above the levels that are present in the AA 5056 (except perhaps for the Fe). Accordingly, after quenching, they can diffuse through the lattice and pin the dislocations [127]. These additional elements are not found in either of the binary alloys, so they may well have contributed to the static aging.

5.1.5   Stress vs. Strain Behavior in Al-3%Mg vs. Al-5%Mg

As previously mentioned, it was to be expected that the additional 2wt% Mg would play a role in enhancing the DSA behavior. The serration intensities of the Al-3%Mg and Al-5%Mg alloys are compared in Figures 5.20 to 5.25.
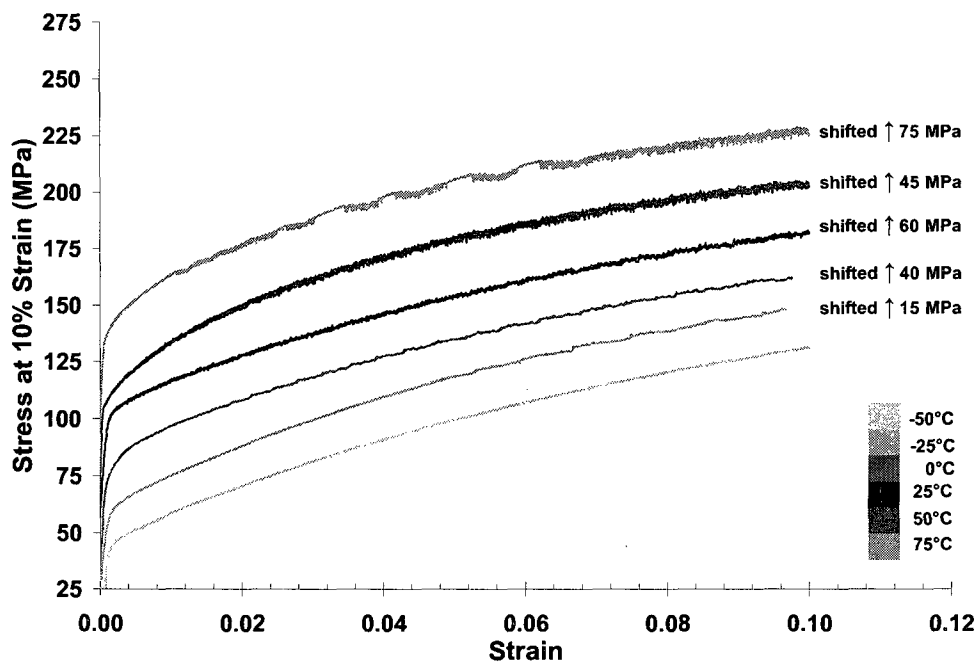
Figure 5.20.   Stress vs. strain curves for selected temperatures for Al-3%Mg determined at a strain rate of 10^{-3} s^{-1} (taken from Figure 4.5).
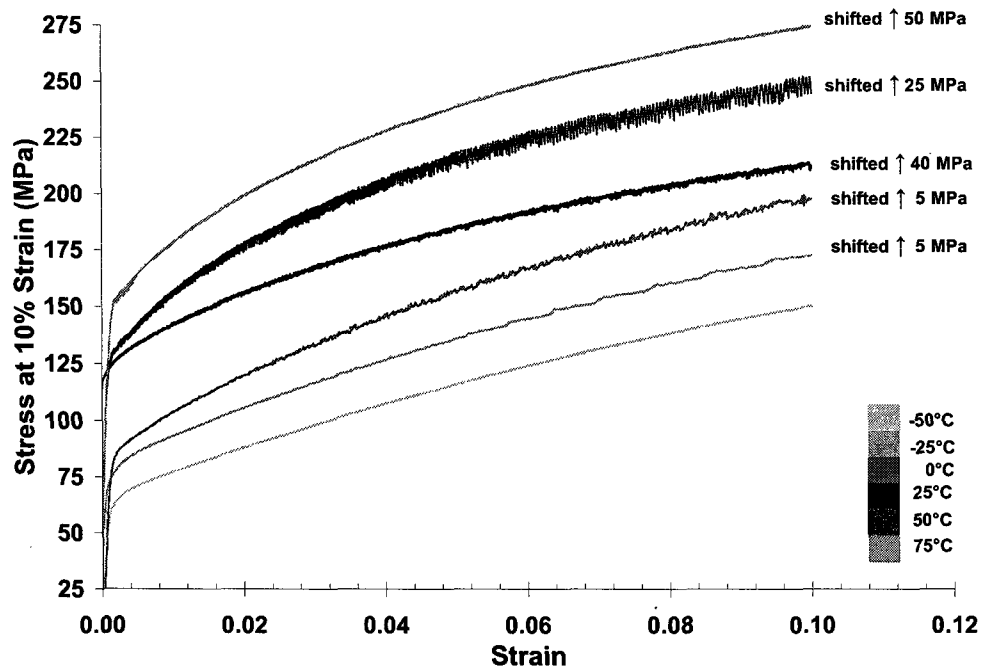
Figure 5.21.   Stress vs. strain curves for selected temperatures for Al-5%Mg determined at a strain rate of 10^{-3} s^{-1} (taken from Figure 4.11).
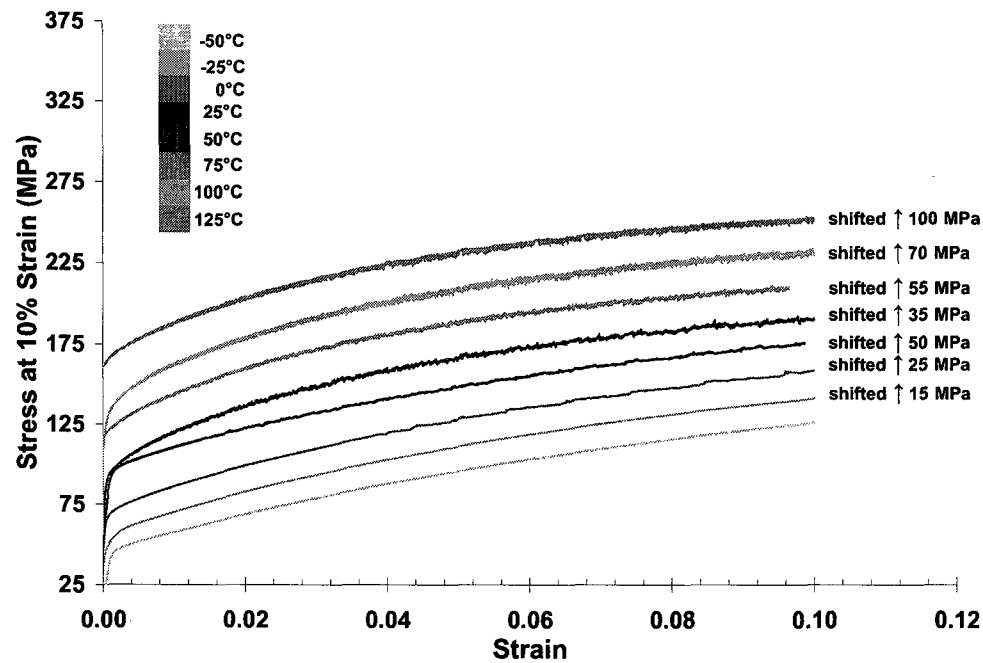
Figure 5.22.   Stress vs. strain curves for select temperatures for Al-3%Mg at a strain rate of 10^{-2} s^{-1} (taken from Figure 4.7).
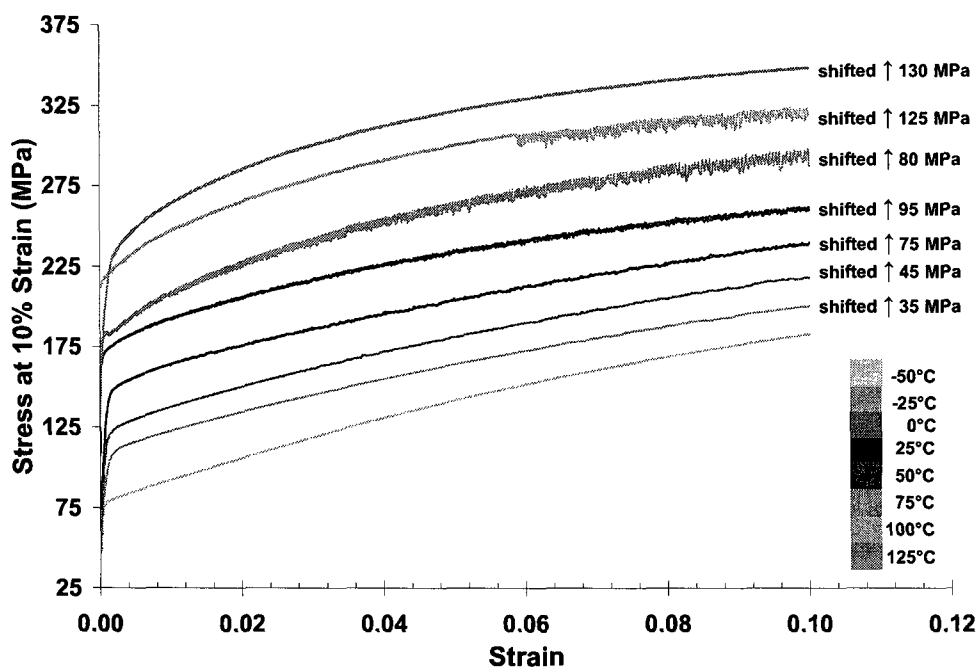
Figure 5.23.   Stress vs. strain curves for selected temperatures for Al-5%Mg determined
at a strain rate of 10^{-2} s^{-1} (taken from Figure 4.13).
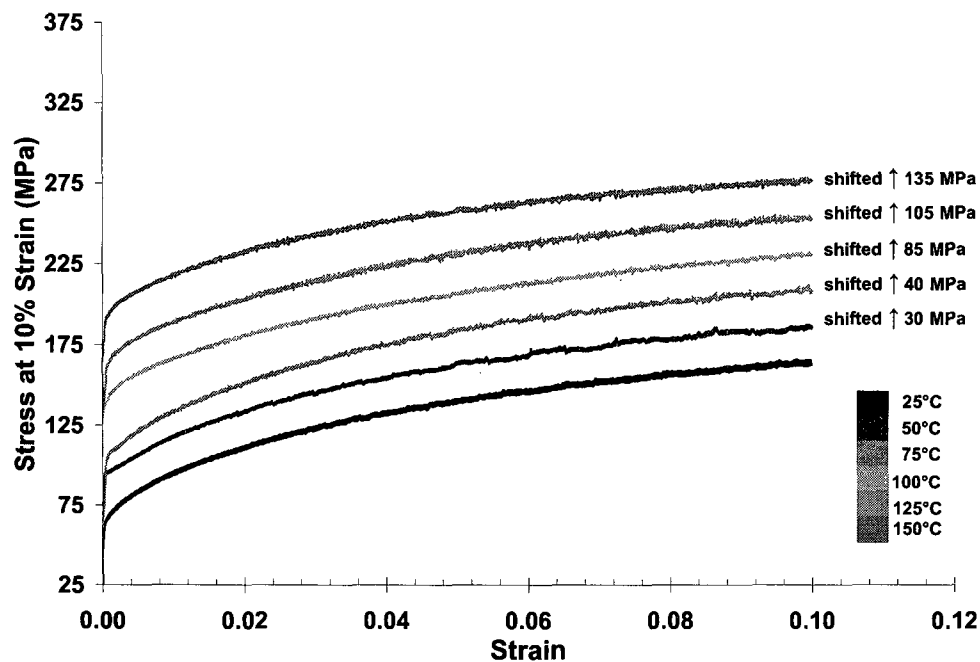
Figure 5.24.   Stress vs. strain curves for selected temperatures for Al-3%Mg determined
at a strain rate of 10^{-1} s^{-1} (taken from Figure 4.9).
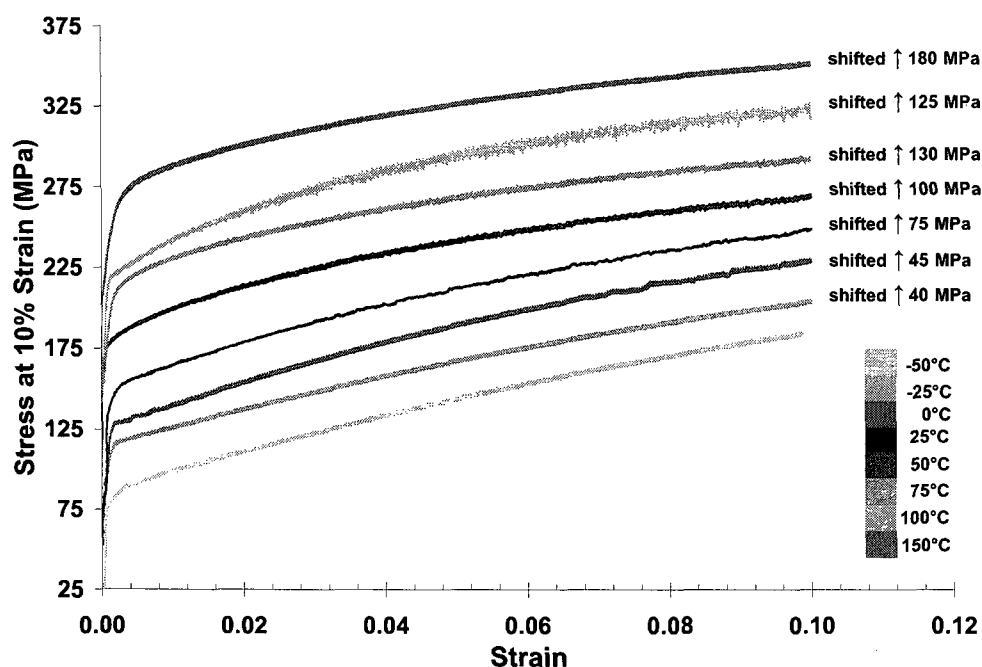
Figure 5.25. Stress vs. strain curves for selected temperatures for Al-5%Mg determined at a strain rate of 10^{-1} s^{-1} (taken from Figure 4.15).

In terms of serration amplitude, it can be seen from the figures that they are comparable in the two alloys at lower temperatures in the DSA regimes (i.e. at each of the three test strain rates). However, with increasing temperature, the stress fluctuations occurring in the Al-5%Mg alloy are larger than in the Al-3%Mg alloy. For example, the stress-strain curve at 50°C in Figure 5.21 exhibits stress drops that are far more pronounced than at 50°C in Figure 5.20. With increases in strain rate, the serration amplitude at a given temperature decreases, as the DSA phenomenon is more prominent at lower strain rates. However, the Al-5%Mg alloy still displays larger fluctuations than the Al-3%Mg alloy.

One point of interest to consider from Figures 5.20 to 5.25 is that, although the Al-5%Mg exhibits larger fluctuations, the serrations in the Al-3%Mg persist to higher temperatures. This

might be attributable to a greater excess of vacancies in the latter material. Given the lower Mg content, the solute atoms may still be able to interact with the dislocations. As these tests were carried out following a solution heat treatment of the test samples, it is possible that an excess of vacancies was introduced during quenching [104, 128] following the solution heat treatment. Another possibility is that fewer solute-vacancy complexes were formed in the Al-3%Mg alloy.

5.2 Strain Rate vs. Inverse Temperature Behavior

The strain rate vs. inverse temperature data for Al-3%Mg, Al-5%Mg and AA 5056 are summarized in Figures 5.26 to 5.28, respectively. These plots resemble those shown in Figure 2.12 for steel, where the diffusing species is C (an *interstitial*) in a bcc (not fcc) matrix. Each diagram is divided into three distinct segments. The two straight line boundaries separating the 'no serrations' regions from the 'serrations' region represent the loci for the appearance (on the lefthand side) and disappearance (on the righthand side) of the DSA serrations, respectively, in the given alloy.

The straight line to the right (i.e. at the lower temperatures) represents the activation energy for the *appearance* of serrations (when the temperature is being increased) while the straight line to the left (i.e. at the higher temperatures) represents the activation energy for the *disappearance* of the serrations. The slope of the line corresponding to the appearance of serrations is expected to yield an activation energy comparable to that of diffusion of the solute species in the lattice. The steeper slope of the line corresponding to the disappearance of the serrations has been proposed to include the binding energy of the solute atoms to the dislocation cores, in addition to the energy associated with the diffusion of the solute species [109].

The activation energy values corresponding to the appearance and disappearance of the DSA serrations can be found using the well-known Arrhenius equation given in Chapter 2:

$$\dot{\varepsilon} = A_f \exp[-Q/RT]$$

As mentioned previously, A_f is a frequency factor and Q is the activation energy for either the onset or disappearance of the serrations. The natural logarithm of the above expression gives the equation of a straight line, with the slope of each 'serration'-'no serration' line equalling '-Q/R'. Knowing that 'R' is a constant, the following values of activation energy were tabulated for the slopes of the DSA regime boundaries for the three alloys in this study. These values are presented in Table 5.2.
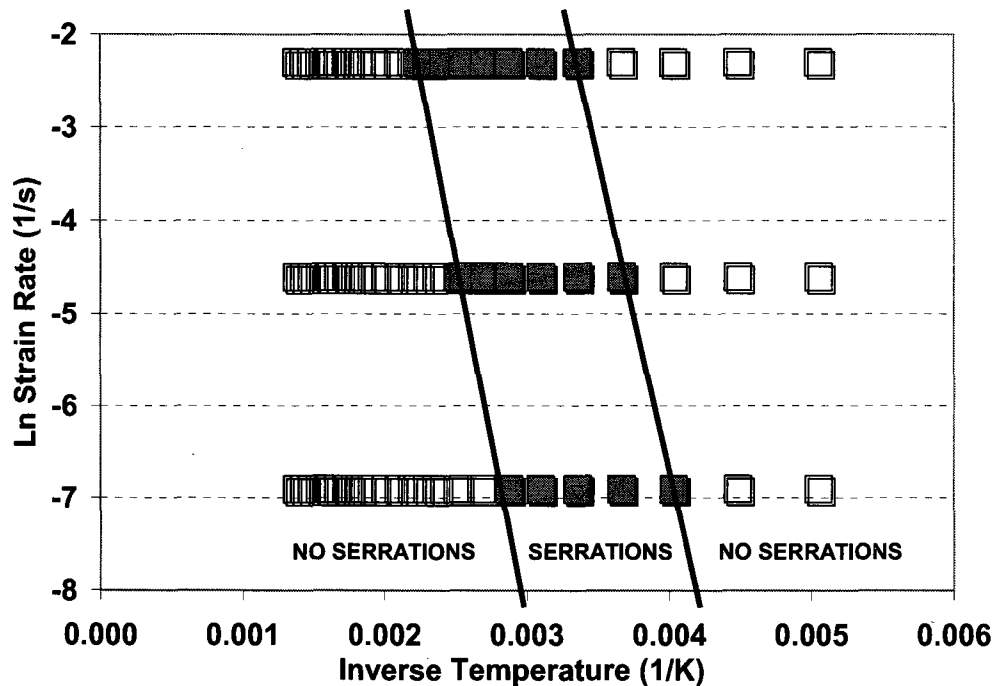
Figure 5.26. Natural logarithm of strain rate vs. inverse absolute temperature plot separating the three ranges of behavior for Al-3%Mg.
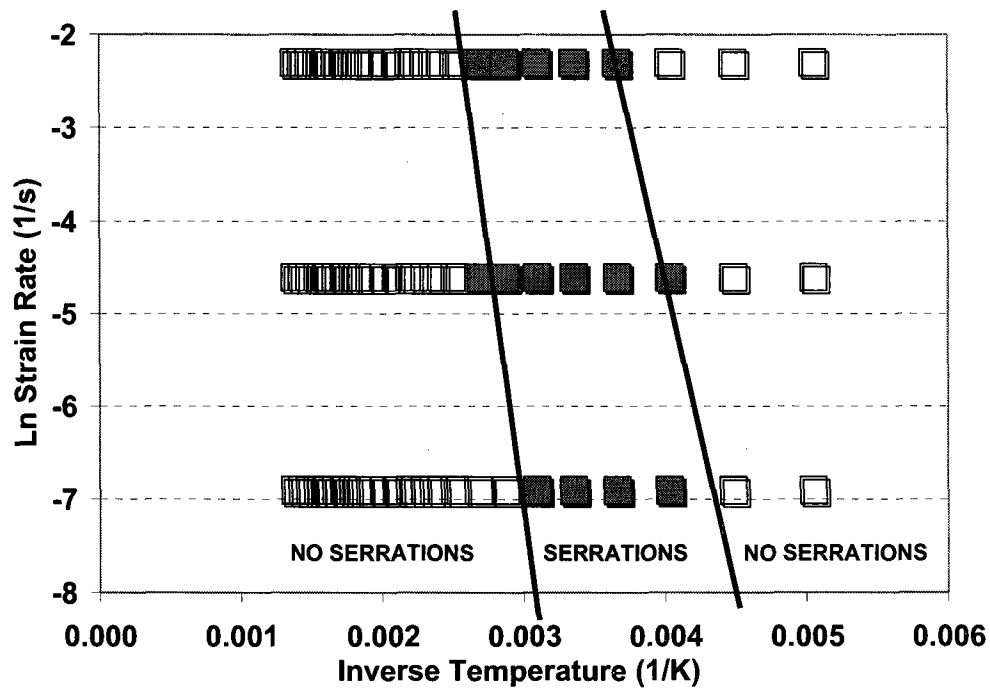
Figure 5.27. Natural logarithm of strain rate vs. inverse absolute temperature plot separating the three ranges of behavior for Al-5%Mg.
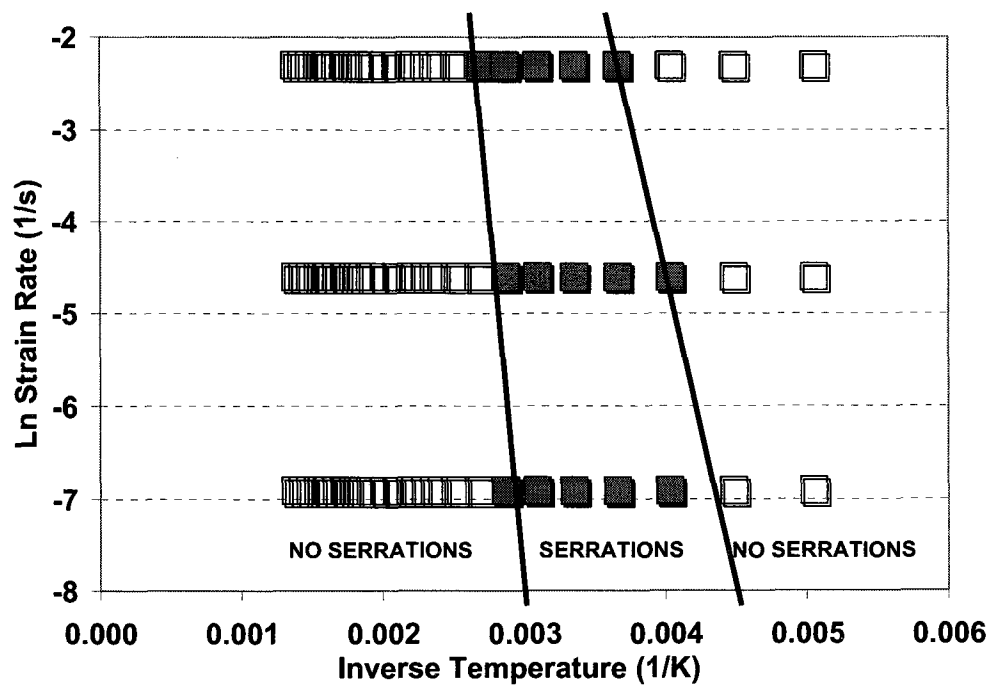
Figure 5.28. Natural logarithm of strain rate vs. inverse absolute temperature plot separating the three ranges of behavior for AA 5056.

As can be seen in Table 5.2, the values for the appearance of serrations are similar (as expected since this value relates to the diffusion of Mg in Al). By contrast, those for the disappearance of the serrations vary from ~0.68 to ~1.36 eV.

Table 5.2   Activation Energies for the Appearance and Disappearance of Serrations

Alloy	Q appearance (kJ/mol)	Q disappearance (kJ/mol)	Q appearance (eV)	Q disappearance (eV)
Al-3%Mg	56	66	0.58	0.68
Al-5%Mg	57	92	0.59	0.95
AA 5056	58	131	0.6	1.36

Brindley and Worthington's work in Al-3%Mg [116] yielded a value of 0.55eV for the onset of serrations, which is also the activation energy for the movement of an Mg atom in Al. Work done by Pink and Grinberg [94] on Al-5%Mg alloys gave values of 0.46 eV and 0.8 eV for the appearance and disappearance of serrations, respectively. Picu *et al.* [103] obtained activation energy values of 0.86 eV and 1.09 eV for the appearance and disappearance of serrations, respectively, in a commercial AA 5182 alloy. McCormick [32] determined an activation energy value of 0.64eV for the onset of serrations in an Al-Mg-Si alloy.

Brindley and Worthington also derived an activation energy value for the disappearance of serrations, as ~0.75eV, provided that a binding energy of 0.2eV existed between a vacancy and an Mg atom. This finding was supported by Fujita and Tabata [95]. Finally, Thomas [84] derived an activation energy value of ~0.35eV for the onset of serrations, based on the earlier work of Westwood and Broom [121], whose Q values lay in the range of 0.27-0.47 eV. Therefore, the activation energy values obtained in this study for the onset and disappearance of DSA serrations are in good agreement with those found in the literature.

5.3   Strain Rate Sensitivity vs. Temperature Behavior

The temperature-dependent flow stress behavior of the alloys tested gave rise to the temperature-dependent strain rate sensitivity behavior that was anticipated. All strain rate sensitivity vs. temperature curves presented in this work were obtained by using equation (6), where the stress 'σ' is the average of 3-5 tensile tests carried out at the given temperature and strain rate. Thus, the rate sensitivity curves obtained reflect an average behavior as well. These curves were plotted for mean strain rates of 5×10^{-3} s^{-1}, 10^{-2} s^{-1} and 5×10^{-2} s^{-1}. They strain rate sensitivity vs. temperature curves for the three alloys were also compared to curves determined on commercially pure aluminum. The rate sensitivity curves for the commercially pure Al are given in Figure 5.29.

Figure 5.29.   Strain rate sensitivity vs. temperature curves for commercially pure Al for mean strain rates of 5×10^{-3} s^{-1}, 10^{-2} s^{-1} and 5×10^{-2} s^{-1}.

As mentioned previously, it was observed that the negative strain rate sensitivity regions in each alloy were coupled with a region of higher than normal strain rate sensitivity. As expected, no indication of DSA behavior was found in the Al and the curves displayed a simple monotonic increase in rate sensitivity. In this way, the negative and abnormally high strain rate sensitivity regimes observed in the alloys are further emphasized. There is much literature on negative strain rate sensitivity in alloys but far less concerning the higher than normal rate sensitivity, although it can be argued that the one implies the existence of the other.

5.3.1   Strain Rate Sensitivity vs. Temperature Behavior in Al-3%Mg

The strain rate sensitivity vs. temperature curves for Al-3%Mg are given in Figure 5.30.
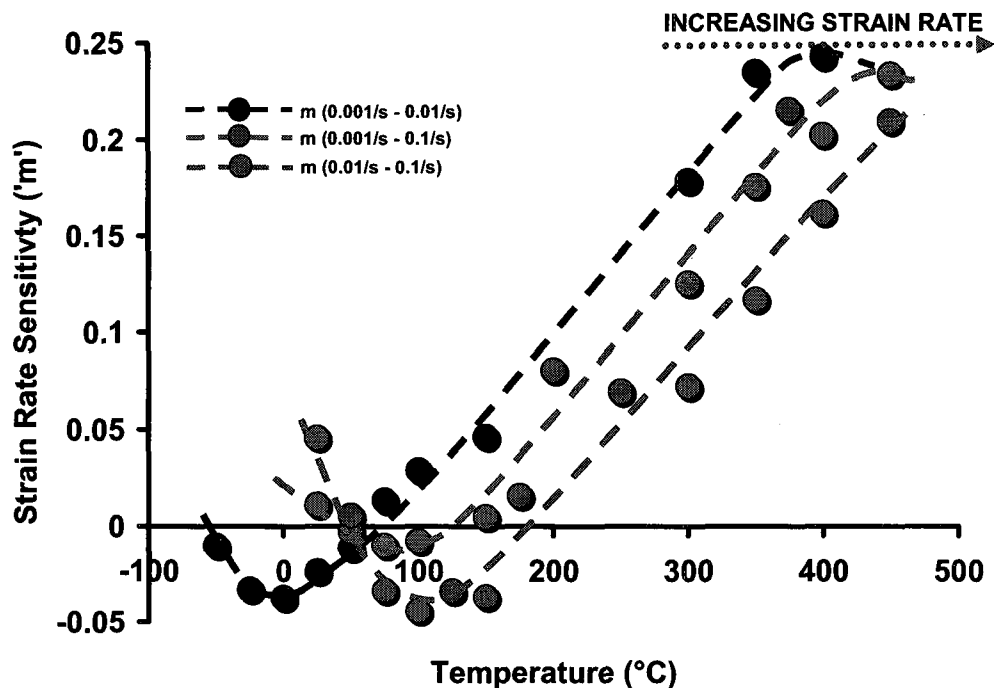
Figure 5.30.   Strain rate sensitivity vs. temperature curves for Al-3%Mg for mean strain rates of 5×10^{-3} s^{-1}, 10^{-2} s^{-1} and 5×10^{-2} s^{-1}.

It was observed that the rate sensitivity in Figure 5.30 has small and positive values below room temperature, i.e. at temperatures *below* the negative rate sensitivity range. It then becomes negative over a small range of temperature as the temperature is increased and finally increases to an unusually high value before decreasing again.

The high strain rate sensitivity region (m~0.2-0.25) is necessarily coupled with the negative strain rate sensitivity region; the latter was seen to coincide with the occurrence of the DSA serrations, as expected. As can be seen, the rate sensitivity curves were shifted to higher temperatures at increased mean strain rates. In turn, the local rate sensitivity peaks are seen to shift to higher temperatures as the mean strain rate is increased.

At the lowest mean strain rate, the rate sensitivity curve is seen to reach a peak, whereas at the highest mean strain rate, the curve is still climbing with temperature. It is anticipated that a peak will be reached at higher test temperatures. Likewise, tests carried out at lower strain rates would shift the given curves to the left, i.e. to lower temperatures. It is important to note that the maximum values of rate sensitivity, and in turn of the elongation, are found at temperatures *below* the maximum test temperature.

The strain rate sensitivity vs. temperature curves for Al-3%Mg compared to the data obtained for the c.p. Al are given in Figure 5.31.
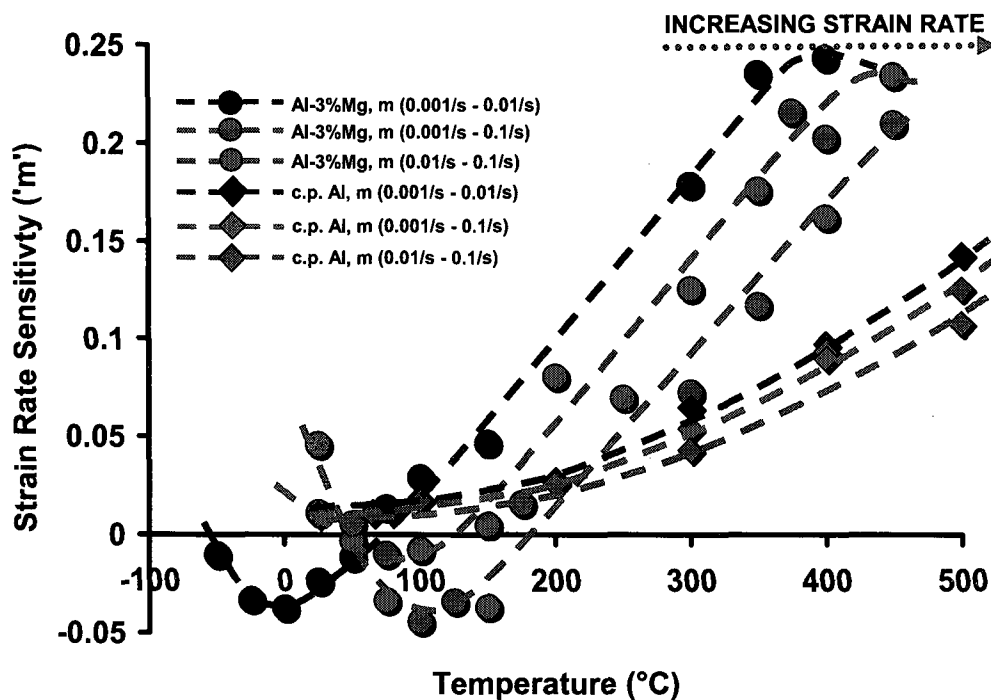
Figure 5.31. Strain rate sensitivity vs. temperature curves for Al-3%Mg and c.p. Al for mean strain rates of 5×10^{-3} s^{-1}, 10^{-2} s^{-1} and 5×10^{-2} s^{-1}.

As can be seen, the rate sensitivity curves for the c.p. Al reach a maximum rate sensitivity of m~0.1-0.15 and are anticipated to continue to climb in value with increasing temperature. At lower temperatures, the c.p. Al curves maintain a small and positive value of 'm', whereas the Al-3%Mg alloy exhibits negative values of 'm', characteristic of DSA-prone alloys. The superposition of the Al-3%Mg and c.p. Al rate sensitivity curves further emphasizes the local higher-than-normal rate sensitivity peaks observed in the Al-3%Mg alloy.

5.3.2   Strain Rate Sensitivity vs. Temperature Behavior in Al-5%Mg

The strain rate sensitivity vs. temperature curves for Al-5%Mg are given in Figure 5.32.
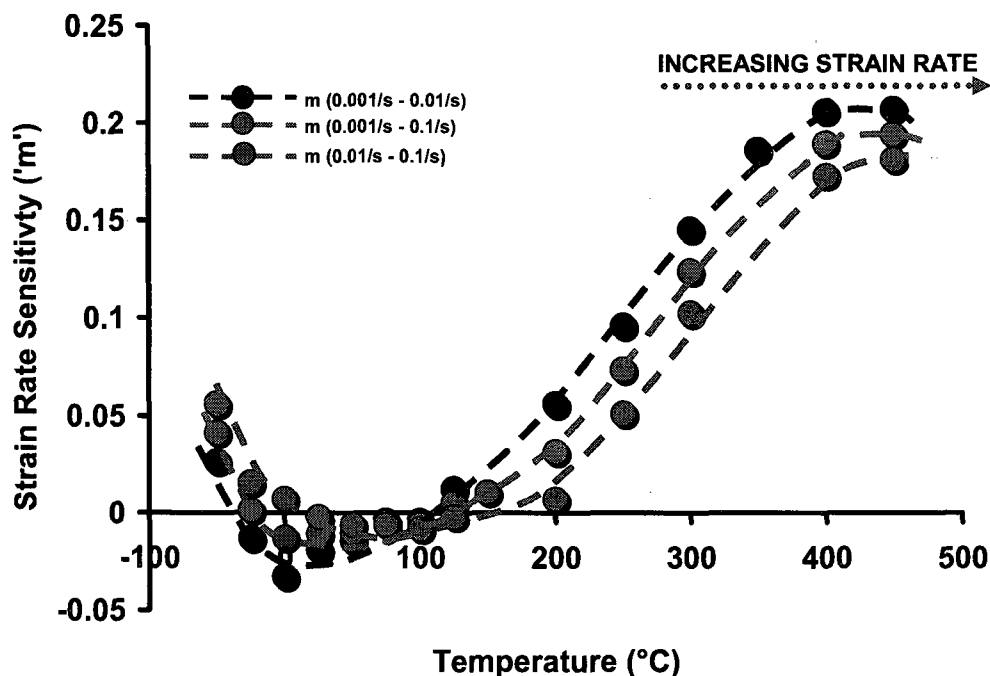
Figure 5.32. Strain rate sensitivity vs. temperature curves for Al-5%Mg for mean strain rates of $5x10^{-3}$ s^{-1}, 10^{-2} s^{-1} and $5x10^{-2}$ s^{-1}.

Once again, at low (sub-ambient) temperatures, the alloy exhibits small positive values of rate sensitivity, as before. It then goes negative on increasing the temperature before reaching an abnormally high local peak (m~0.2). Moreover, the curves are seen to shift to higher temperatures when the mean strain rate is increased. The negative rate sensitivity area was seen to coincide with the occurrence of the DSA serrations, as expected. As well, the local rate sensitivity peaks are located at temperatures lower than the maximum test temperature and are also seen to shift to higher temperatures at increased mean strain rates.

The superposition of the Al-5%Mg and c.p. Al rate sensitivity curves further emphasizes the local higher-than-normal rate sensitivity peaks observed in the Al-5%Mg alloy, as shown in Figure 5.33. The c.p. Al curves, however, simply increase monotonically in 'm' with temperature.
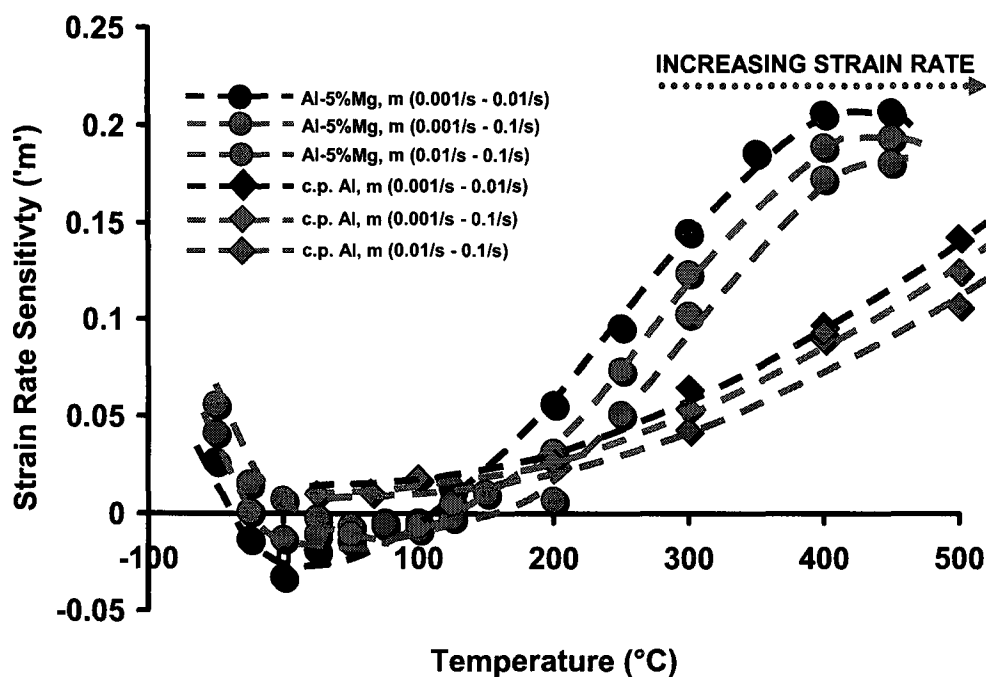
Figure 5.33. Strain rate sensitivity vs. temperature curves for Al-5%Mg and c.p. Al for mean strain rates of 5×10^{-3} s^{-1}, 10^{-2} s^{-1} and 5×10^{-2} s^{-1}.

5.3.3   Strain Rate Sensitivity vs. Temperature Behavior in AA 5056

The strain rate sensitivity vs. temperature curves for AA 5056 are given in Figure 5.34.

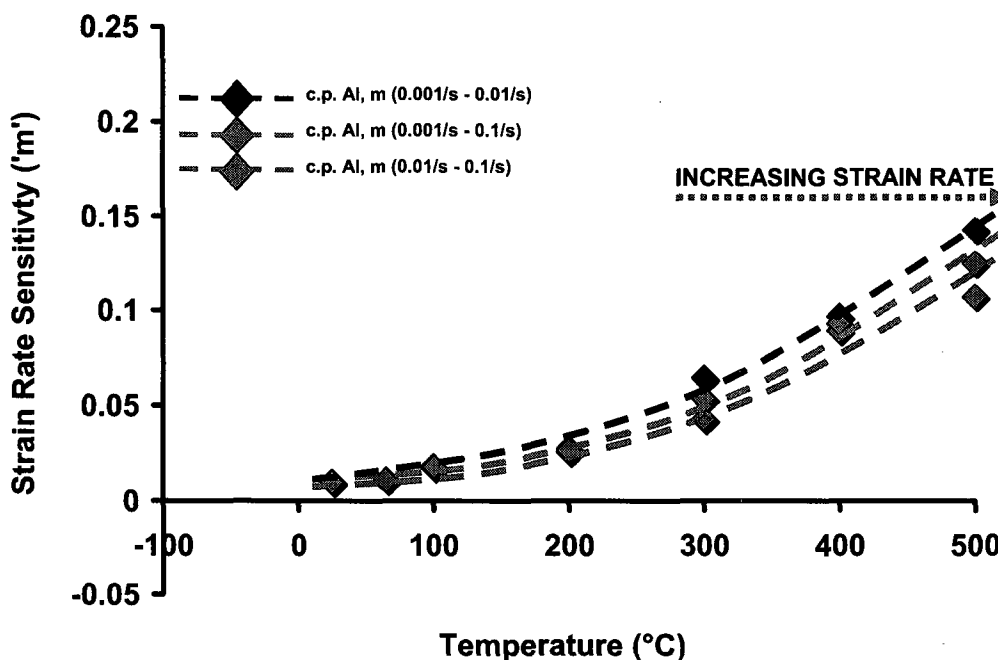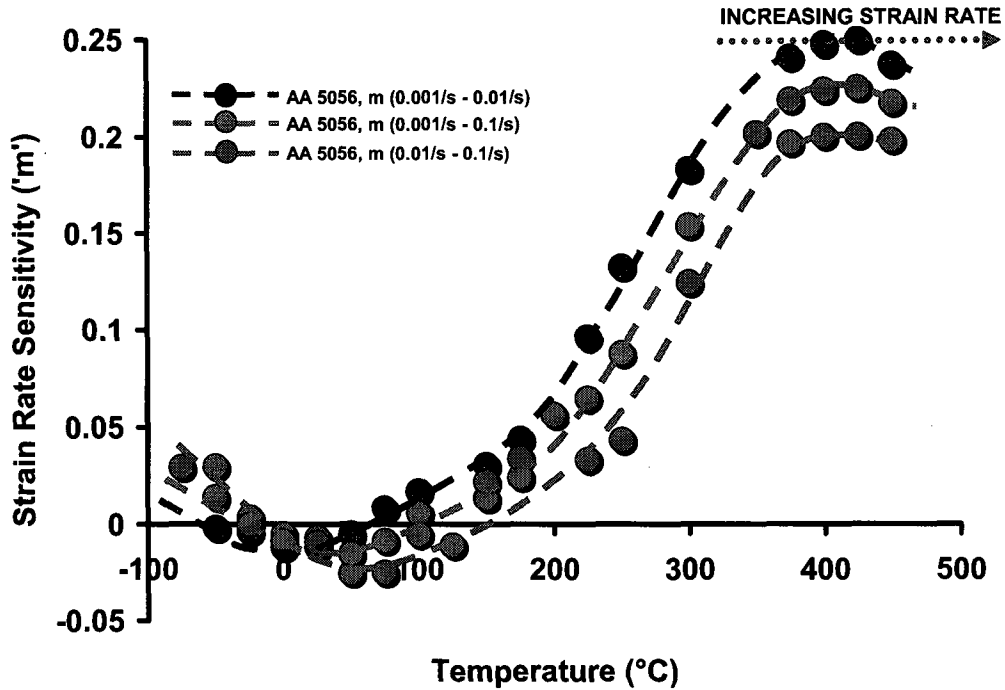**Figure 5.34. Strain rate sensitivity vs. temperature curves for AA 5056 for mean strain rates of 5×10^{-3} s^{-1}, 10^{-2} s^{-1} and 5×10^{-2} s^{-1}.**

As with the two binary Al-Mg alloys shown in Figures 5.30 to 5.33, the AA 5056 alloy exhibits small positive values of rate sensitivity at very low temperatures before turning negative as the temperature is raised. On further increases in temperature, a high local rate sensitivity peak is reached (m~0.2-0.25). These curves are seen to shift to higher temperatures with increased mean strain rates and, once again, the negative rate sensitivity area was noted to coincide with the occurrence of the DSA serrations.

As with the Al-3%Mg and Al-5%Mg alloys, the superposition of the AA 5056 and c.p. Al rate sensitivity curves (Figure 5.35) further emphasizes the local higher-than-normal rate sensitivity peaks observed in the AA 5056 alloy, whereas the c.p. Al curves simply increase monotonically in 'm' with temperature.
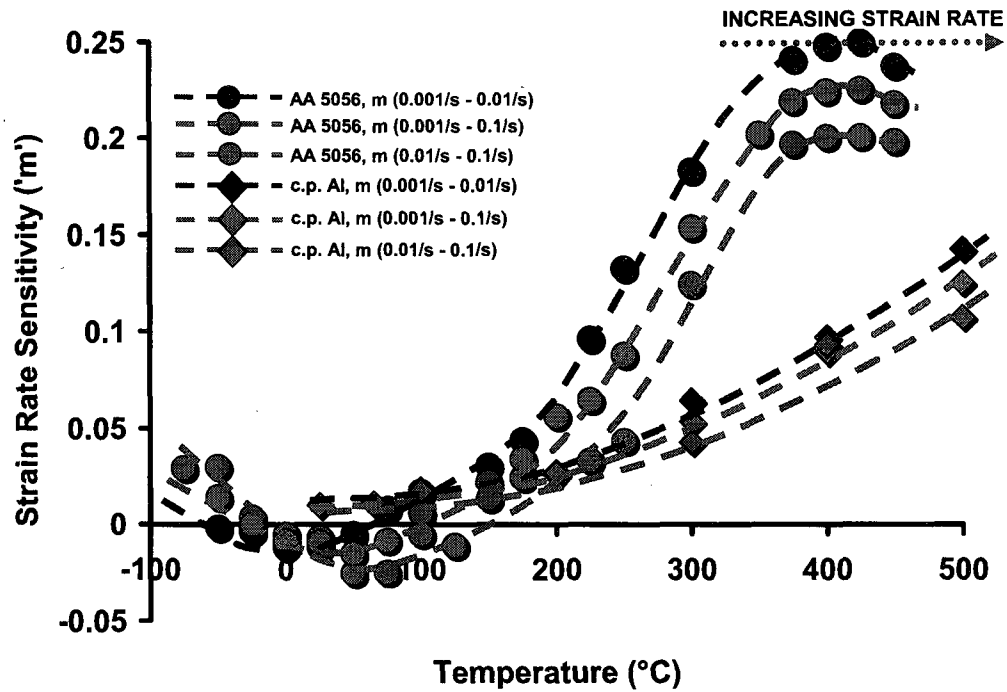
Figure 5.35. Strain rate sensitivity vs. temperature curves for AA 5056 and c.p. Al for mean strain rates of $5x10^{-3}$ s^{-1}, 10^{-2} s^{-1} and $5x10^{-2}$ s^{-1}.

As can be seen from Figures 5.30 to 5.35, the strain rate sensitivity curves experience higher-than-normal local rate sensitivity peaks. Moreover, these curves shift to higher temperatures with increased mean strain rates.

At temperatures where the strain rate sensitivity would be negative in any alloy, the c.p. Al retains a small positive value of strain rate sensitivity (Figure 5.29). With increasing

temperature, the 'm' values for the c.p. Al simply increase monotonically, while the alloys exhibit the 'unexpected' DSA behavior [51-55, 109].

In the results reported for 304 stainless steel by Stewart [109], a definite decrease in 'm' was observed following the local maximum. It can therefore be expected that the 'm' values in this work would also decrease were the samples to be tested at higher temperatures.

Given that the solution temperature used was 450°C for 8 hours, enough time was allowed for Mg to form a solid solution with Al. Under these conditions, the DSA serrations are readily visible at lower temperatures. Nevertheless, the 'm' values did not always decrease after reaching a maximum of m~0.2-0.25 in the three alloys. For example, in Figure 5.30, the rate sensitivity curve for Al-3%Mg at the highest mean strain rate only increases monotonically, although, at lower mean strain rates, it is seen that the two curves do indeed display peaks. Therefore, it is expected that a peak would also have been reached at the highest mean strain rate, provided that a higher test temperature had been used. On the other hand, the c.p. Al reaches m~0.1 when the alloys reach their peak.

5.4   Enhanced Ductility Tensile Tests

Seeing that the present alloys exhibit a region of high strain rate sensitivity, their potential for superplasticity or enhanced ductility behavior was investigated in terms of the dependence of the flow stress and strain rate sensitivity on temperature. First, the information obtained from the flow stress vs. temperature behavior was used to derive the dependence of strain rate sensitivity on temperature, as described above.

Numerous tensile tests were carried out to failure to test for the existence of extended ductility; these yielded values of elongation of up to 170% in the ASTM E2448-06 samples, for example, in the vicinity of the strain rate sensitivity peak. These samples were deformed at temperatures of up to 550°C and the ductility was measured using scribed gage marks.

From the work of Verma *et al.* [4] on the superplasticity of 5083 Al alloy, it was suggested that the maximum testing temperature for an Al alloy having a nominal Mg content of 5wt% was ~575°C. Therefore, the above-mentioned samples were solution heat treated at 560°C (for 2 hours, then water-quenched) and the maximum test temperatures used was 550°C.

The results of the enhanced ductility tests were presented in Figures 4.27 to 4.29. The tests carried out on the ASTM E2448-06 samples were reproducible and followed the anticipated trend in rate sensitivity with temperature as given in the previous section.

These results are presented here as elongation vs. temperature plots in Figures 5.36 to 5.42 in Sections 5.4.1, 5.4.2 and 5.4.3 for Al-3%Mg, Al-5%Mg and AA 5056, respectively. The blue filled circles in these diagrams represent actual tests performed and the red empty squares represent averages of individual tests.

Moreover, these curves are also superimposed on data from some c.p. Al tests that were carried out in the vicinity of the 'humps' observed in the three alloys. The behaviors of the present three materials will now examined in more detail.

5.4.1   Enhanced Ductility in Al-3%Mg

The elongation vs. temperature curve for Al-3%Mg is given in Figures 5.36.
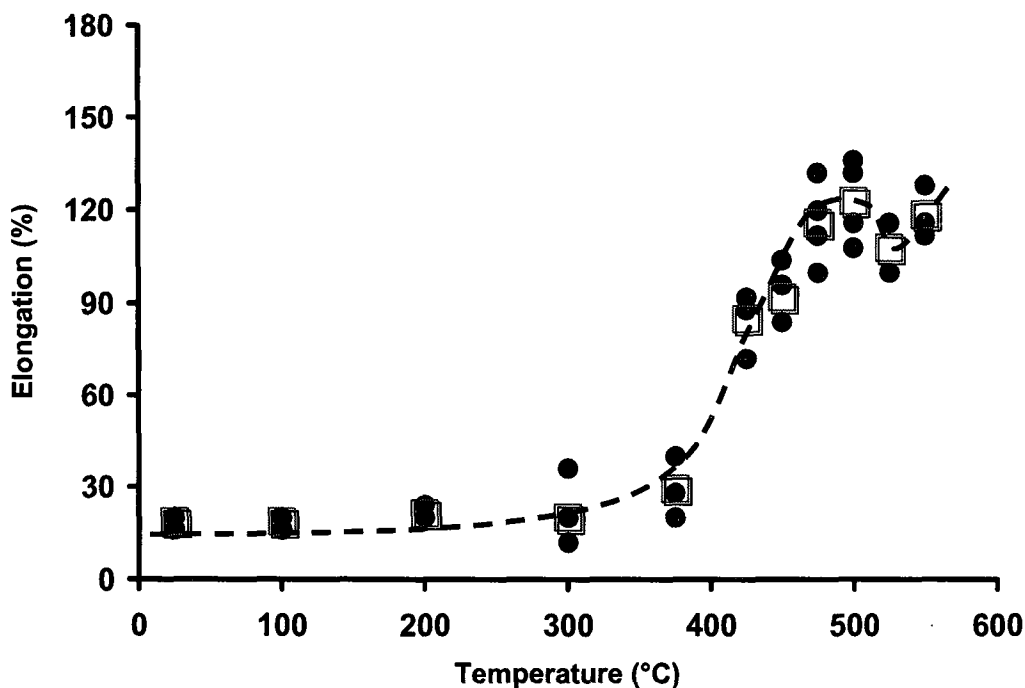
Figure 5.36.   Elongation vs. temperature curve for Al-3%Mg for a strain rate of 5×10^{-3} s^{-1}.

It can be seen that the average for each test condition reflects the observed rate sensitivity behavior. That is to say, there is a local maximum, followed by a slight decrease in elongation, which is then followed by an *increase* in elongation. Note also that the local maximum occurred at 475°C-500°C, i.e. below the solutionizing temperature used. It can be seen that there is very little change in elongation in the Al-3%Mg until a temperature of ~375°C is reached. After this, there is a marked increase until 475°C-500°C, before sinking at 525°C and then climbing again at 550°C. Tests were carried out up to 550°C with Mg always remaining in solution.

The behavior displayed in Figure 5.36 resembles that in Figure 5.30, although the peak 'm' observed in Figure 5.30 for a mean strain rate of 5×10^{-3} s^{-1} was 400°C. Nevertheless, Figures 5.30 and 5.36 both display local peaks, rather than a monotonic increase in elongation. The reason why the peaks are located at different temperatures is not known at this point, although it does suggest that the relevant 'm' curve should be determined at a higher mean strain rate.

The elongation vs. temperature curve given in Figure 5.36 is then plotted in Figure 5.37 against several measured values of elongation in c.p. Al, where the orange filled circles represent actual c.p. Al tests performed and the green empty squares represent the averages of these individual tests. The c.p. Al samples were pulled to failure at temperatures in the vicinity of the 'hump' observed in the Al-3%Mg alloy.
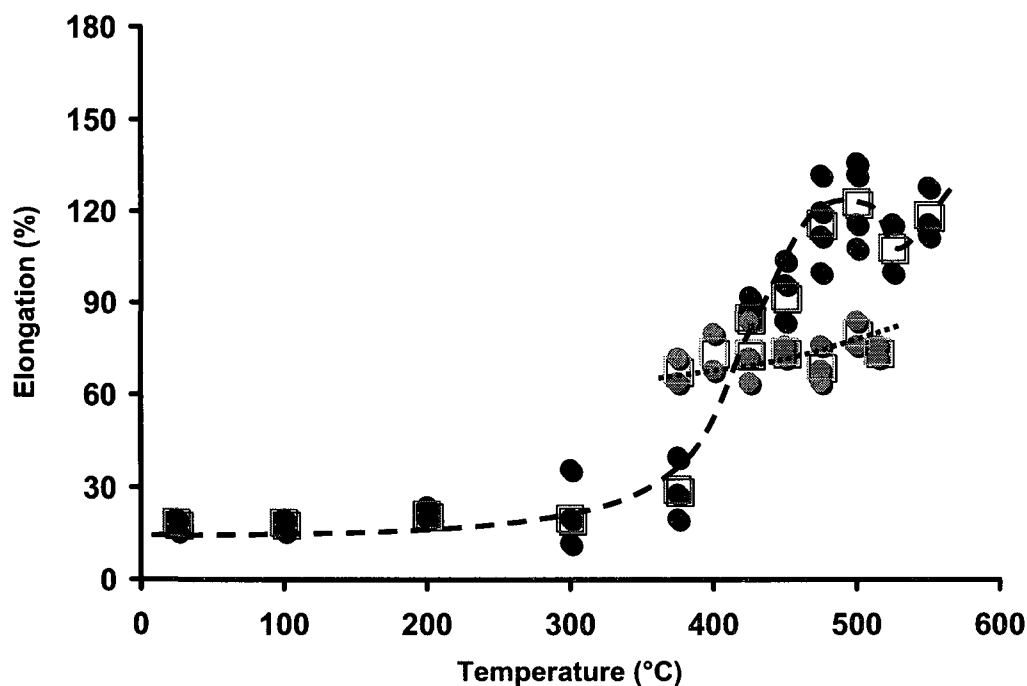
Figure 5.37. Elongation vs. temperature curves for Al-3%Mg and c.p. Al for a strain rate of 5×10^{-3} s^{-1}.

Note that the elongations in the Al-3%Mg at temperatures below 400°C are *below* those shown in Figure 5.37 for the c.p. Al curve. This can be linked with the negative rate sensitivities displayed by the alloy in this temperature range, particularly when higher strain rates are employed. It is evident from Figure 5.37 that there is a tendency for the elongation of the c.p. Al to increase with temperature, albeit not as dramatically as in the Al-3%Mg alloy.

The rate sensitivity behavior illustrated in Figure 5.31 for the Al-3%Mg and c.p. Al resembles that shown in Figure 5.37. Again, the elongation peak in Figure 5.37 occurs at a higher temperature than the 'm' peak in Figure 5.31 and in both cases the 'baseline' curve of the c.p. Al increases monotonically with temperature. The temperature difference is possibly attributable to the selection of the appropriate strain rate for the 'm' curve, as already suggested above.

The 'm' values observed in the Al-3%Mg 'hump' of Figure 5.31 are much higher than for c.p. Al. Similarly, the values of percent elongation in the c.p. Al in Figure 5.37 are lower than for Al-3%Mg along the 'hump'.

5.4.2   Enhanced Ductility in Al-5%Mg

The elongation vs. temperature curve for Al-5%Mg is given in Figure 5.38.

Figure 5.38.   Elongation vs. temperature curve for Al-5%Mg for a strain rate of 5x10^{-3} s^{-1}.

As in the case of the Al-3%Mg alloy, it can be seen that the elongation in the Al-5%Mg alloy depends on the temperature. The peak ductility occurs at 450°C and the variation in elongation here is slightly greater than at the other temperatures. Nevertheless, the test averages mimic the observed rate sensitivity behavior.

The Al-5%Mg alloy behaved in a fashion similar to that of the Al-3%Mg, although the initial period of little change in elongation only occurred up to a temperature of ~200°C. After this, there was a marked increase in elongation until 450°C, before sinking to 525°C and 550°C.

Were this material to have been tested at higher temperatures, one can anticipate that the elongation would have begun to climb again somewhat. The behavior displayed in Figure 5.38 resembles that illustrated in Figure 5.32, where the peak 'm' was observed at ~450°C for a mean strain rate of 5×10^{-3} s^{-1}.

Although further tensile tests are required at temperatures greater than 450°C in order to acquire a more 'complete' curve in Figure 5.32, it can be seen that Figures 5.32 and 5.38 both display local peaks, rather than a monotonic increase in elongation. The elongation vs. temperature curve for Al-5%Mg is plotted against that for c.p. Al in Figure 5.39.

Figure 5.39. Elongation vs. temperature curves for Al-5%Mg and c.p. Al for a strain rate of 5×10^{-3} s^{-1}.

It can be seen here that the elongation observed in the c.p. Al is much lower than in the Al-5%Mg. Given that the elongation values along the 'hump' in the Al-5%Mg are greater than in the Al-3%Mg, the 'hump' in Figure 5.39 contrasts more sharply with the c.p. Al curve.

As already indicated above, the Al-5%Mg elongations at the lower temperatures are *lower* than those expected by extrapolation of the c.p. Al data. Again, this is probably attributable to the negative alloy 'm' values in this temperature range, particularly if the 'm' tests are carried out at higher strain rates.

The rate sensitivity behaviors illustrated in Figure 5.33 for Al-5%Mg and c.p. Al resemble those shown in Figure 5.39. In both sets of curves, it can be seen that the 'baseline' c.p. Al curves lies well below the Al-5%Mg 'humps'. The 'm' values present in the Al-5%Mg 'hump' of Figure 5.33 are higher than for c.p. Al. Thus it is to be expected that the percent elongations in the c.p. Al in Figure 5.39 are lower than for Al-5%Mg along the 'hump'.

The Al-5%Mg samples were also tested at a strain rate of 10^{-2} s^{-1} to show that as the strain rate is increased, the elongation vs. temperature behavior shifts to higher temperatures (Figure 5.40). This coincides with what was predicted in Section 5.3, i.e. that the strain rate sensitivity vs. temperature behavior of an alloy shifts to higher temperatures as the strain rate is increased.
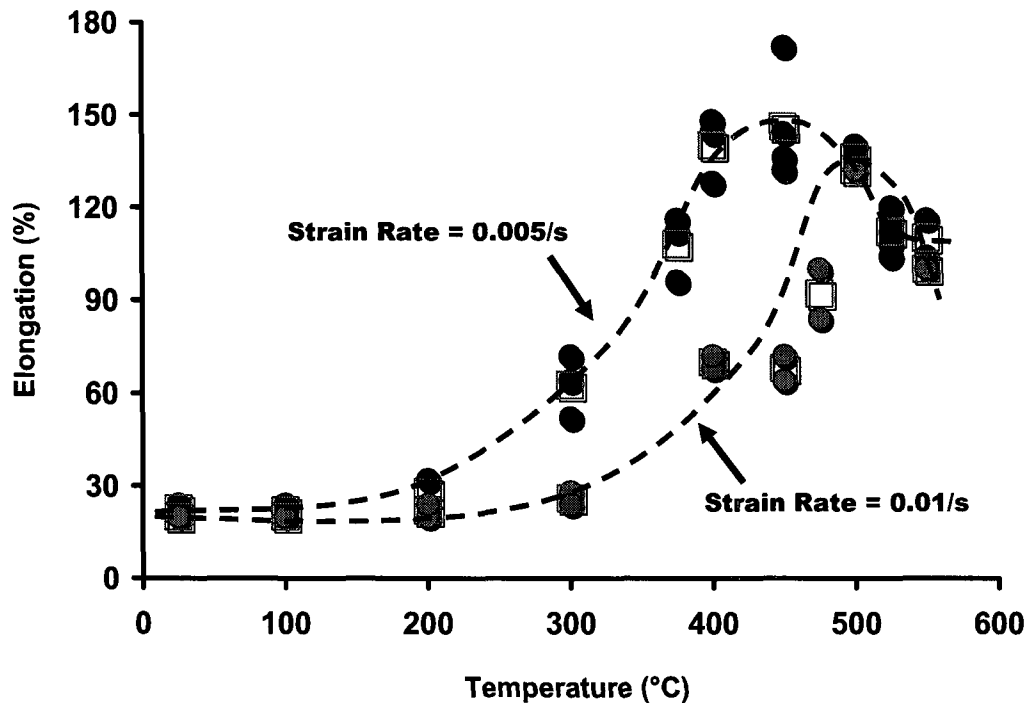
Figure 5.40. Elongation vs. temperature curve for Al-5%Mg for strain rates of 5×10^{-3} s^{-1} and 10^{-2} s^{-1}.

With an increase in strain rate from 5×10^{-3} s^{-1} to 10^{-2} s^{-1}, the initial period of little change in elongation at $\dot{\varepsilon} = 10^{-2}$ s^{-1} extends to a temperature of ~300°C, as opposed to ~200°C at $\dot{\varepsilon} = 5\times10^{-3}$ s^{-1}. This is internally consistent since very little change in elongation was detected at the lower temperatures for $\dot{\varepsilon} = 5\times10^{-3}$ s^{-1} (Figure 5.38).

Above ~300°C, there is a noticeable increase in elongation until 500°C, before it sinks to the value observed at 550°C. It should be noted that the two elongation peaks in Figure 5.40 are distinct and shifted to higher temperatures, as is the case with the strain rate sensitivity vs. temperature plots.

5.4.3   Enhanced Ductility in AA 5056

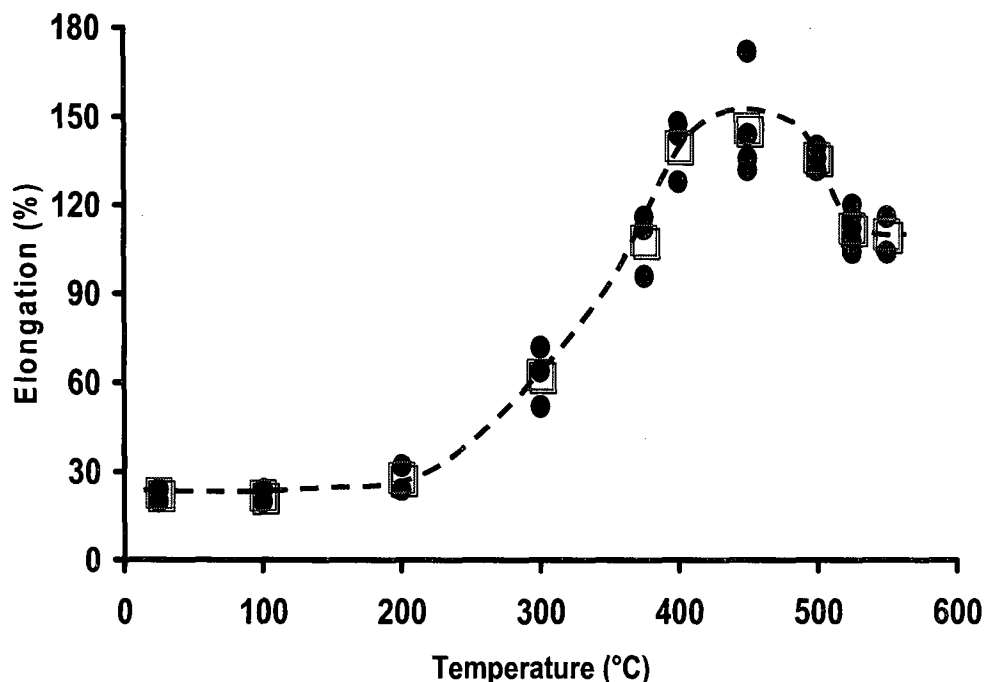The elongation vs. temperature curve for AA 5056 is given in Figure 5.41.
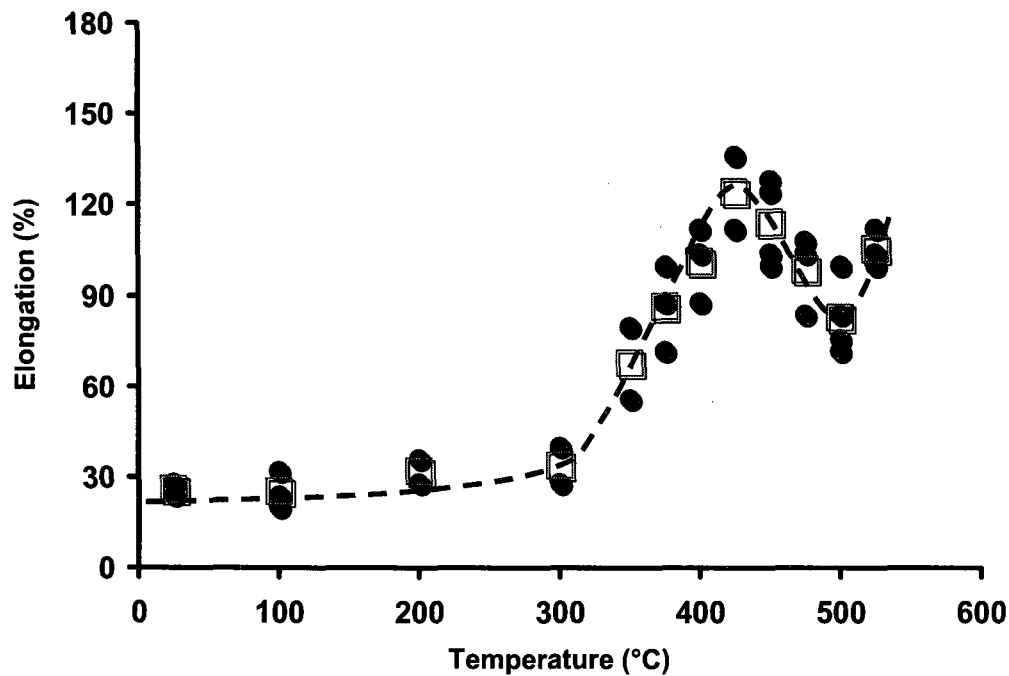
Figure 5.41.   Elongation vs. temperature curve for AA 5056 for a strain rate of 5×10^{-3} s^{-1}.

As in the case of the two binary Al-Mg alloys, it can be seen that the elongation depends on the temperature. Moreover, the test averages reflect the observed rate sensitivity behavior. The elongation increases noticeably above 300°C and reaches a peak at ~425°C before decreasing to a local minimum at 500°C; it eventually climbs again on further increases in temperature.

Given that the AA 5056 and Al-5%Mg alloys contain the same amount of Mg, it can be concluded that the probable reason for the slight decrease in elongation in the commercial alloy

is the formation of cavities due to the presence of second phase particles. Evidence for the presence of these phases was illustrated in Figure 4.2. Although the grains are much coarser in the super-pure Al-5%Mg alloy, there are no second phase particles to reduce the ductility. This promoted the DSA phenomenon by extending the strain range over which it could act.

The behavior displayed in Figure 5.41 resembles that reported in Figure 5.34, where the peak 'm' was observed at ~425°C-450°C for a mean strain rate of $5x10^{-3}$ s^{-1}. Although further tensile tests are again required at temperatures greater than 450°C in order to acquire a more 'complete' curve in Figure 5.34, it is seen that Figures 5.34 and 5.41 both display local peaks, rather than a monotonic increase in elongation. The elongation vs. temperature curve for AA 5056 is compared with that for c.p. Al in Figure 5.42.
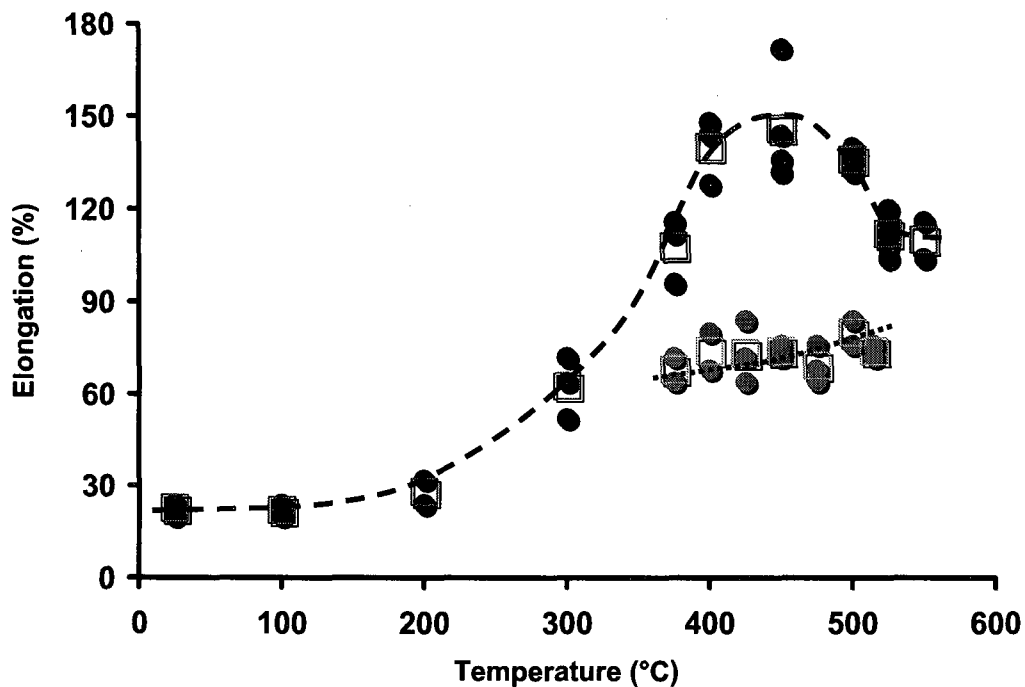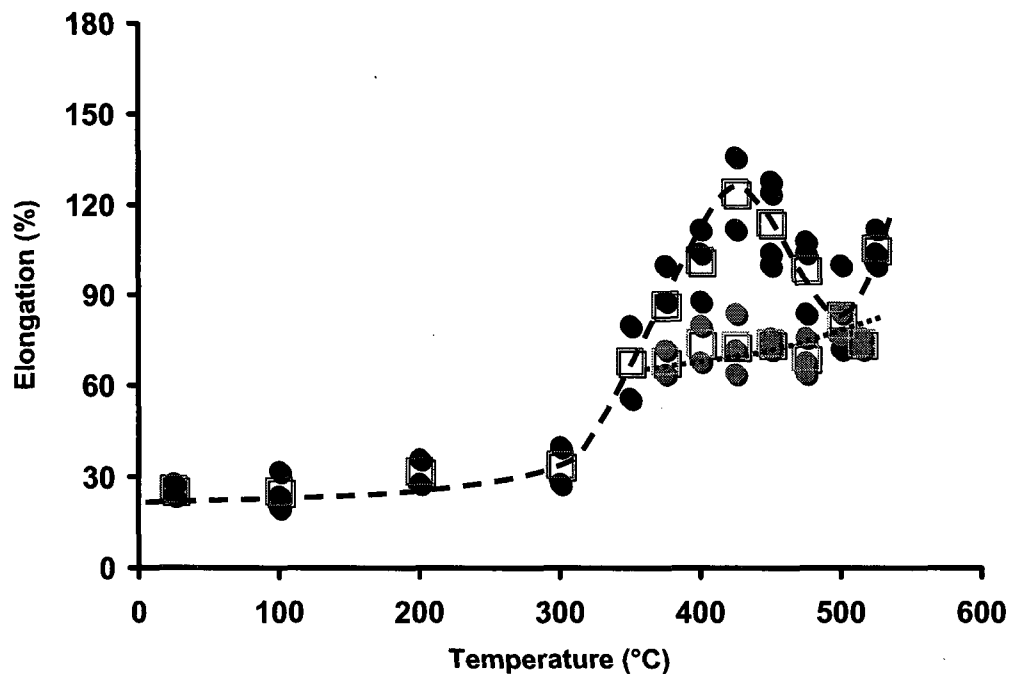

Figure 5.42.   Elongation vs. temperature curves for AA 5056 and c.p. Al for a strain rate of $5x10^{-3}$ s^{-1}.

Again, it is evident that the elongations displayed by the c.p. Al are much lower than in the AA 5056. This further emphasizes the 'hump' observed in the AA 5056, which extends over the same test temperature range as that used for the c.p. Al.

The rate sensitivity behaviors illustrated in Figure 5.42 for Al-5%Mg and c.p. Al resemble those shown in Figure 5.35. In both sets of curves, it can be seen that the 'baseline' c.p. Al curve lies well below the AA 5056 'hump'. The 'm' values observed in the AA 5056 'hump' of Figure 5.35 are higher than for c.p. Al. It is interesting to note that in Figure 5.42, the 'baseline' c.p. Al curve covers the same temperature range as the AA 5056 'hump'. As with Al-3%Mg and Al-5%Mg, it is to be expected that the percent elongations in the c.p. Al in Figure 5.42 will be lower than for AA 5056 along the 'hump'.

It is evident from these figures that the ductility reaches a local maximum in each material and for each mean strain rate at temperatures below the maximum test temperature. This is consistent with the predictions that can be made from the flow stress vs. temperature behaviors determined in the standard tensile tests. Regardless of the alloy being tested to failure, there is a steady increase in percent elongation with increasing temperature until a local peak in elongation is reached.

Given that grain boundary sliding cannot be responsible for enhanced ductility in coarse-grained materials, the observed enhanced ductility must be attributed to the unusual increase in strain rate sensitivity with temperature that is associated with DSA.

5.4.4   Enhanced Ductility in Commercial vs. Binary Al-Mg Alloys

It was seen in Figures 5.36 to 5.42 that there was a steady increase in percent elongation with increasing temperature until the point of maximum ductility was reached. Following the point of maximum elongation, the ductility decreased, somewhat unexpectedly. This coincides with the behaviors predicted from the strain rate sensitivity vs. temperature curves (Figures 5.30 to 5.35). In conventional materials, the strain rate sensitivity increases *continuously* with temperature, so that the elongation increases monotonically [129]. This is shown in Figure 5.43.
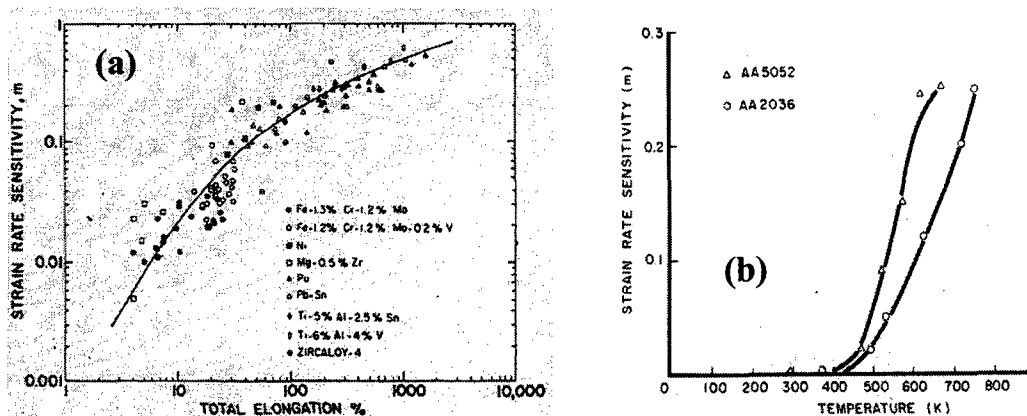
Figure 5.43.   **(a) Total elongation as a function of rate sensitivity in various materials [65] and (b) rate sensitivity as a function of temperature in Al alloys [130]**

In the work of Woo *et al.* [17], it was suggested that (1) since no second phases were observed in their coarse-grained binary Al-Mg alloys and (2) if the rate-controlling mechanism is solute drag, which is independent of grain size and is associated with high rate sensitivity, then cavitation and dynamic grain growth were not factors that limited the ductility.

This was proposed because the peak ductility in their work was associated with a temperature well below their highest test temperature, i.e. the alloys did not follow the monotonic behavior shown in Figure 5.29. Although peak ductilities of 240% to 350% were obtained, these values decreased as the temperature was increased to 500-550°C. This is presented in Figure 5.44.
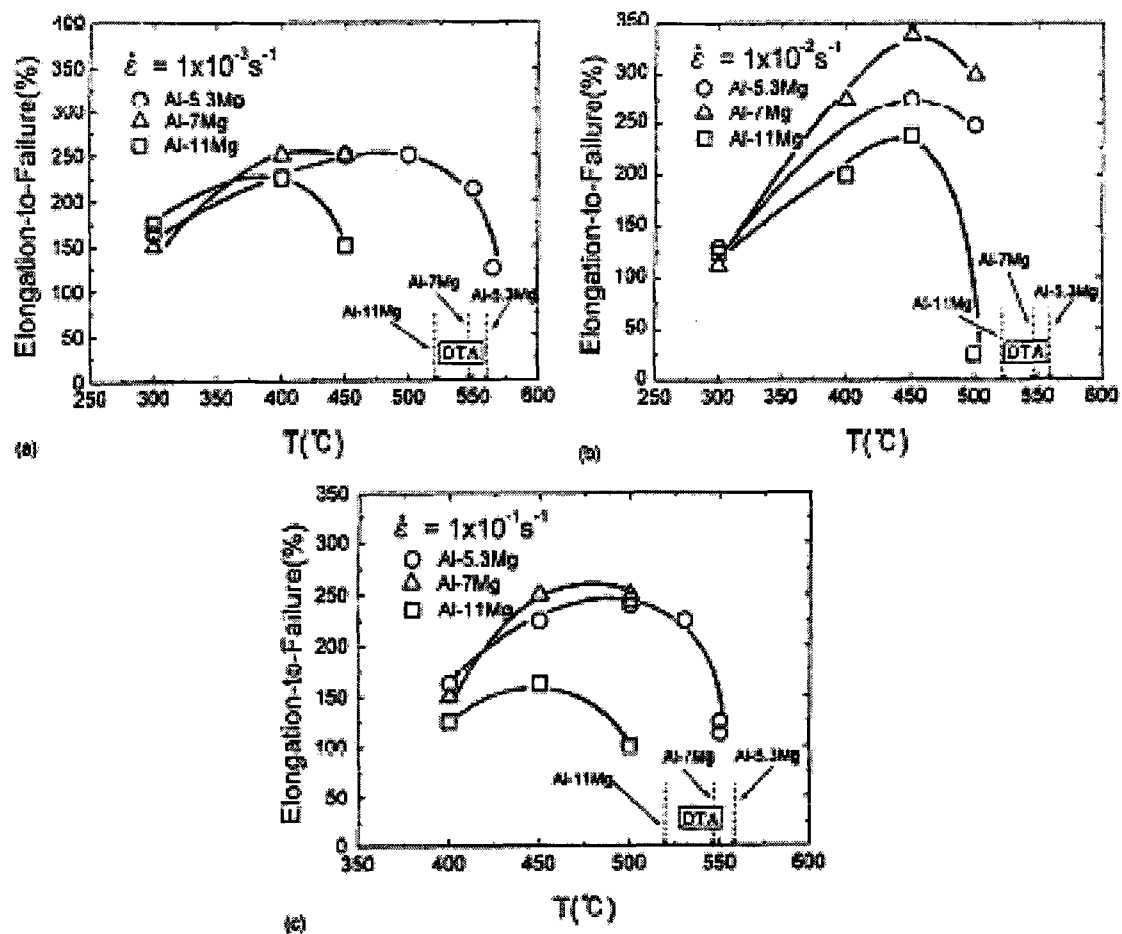
Figure 5.44. Elongation-to-failure vs. temperature in binary Al-Mg alloys [17].

The tensile ductility behaviors of Al-5.3%Mg and Al-7%Mg alloys with grain sizes of 130-140 μm were compared by Woo *et al.* [17] to that in a commercial 7475 Al alloy with a

grain size of 14 µm (Figure 5.45(a)). It was observed that the ductility in the 7475 alloy

decreased with increasing strain rate. Despite its finer grain size, the 7475 alloy experienced

limited ductility due to formation of the cavities that prevailed at the higher strain rates. Ghosh

[131] reported similar findings (Figure 5.45(b)).
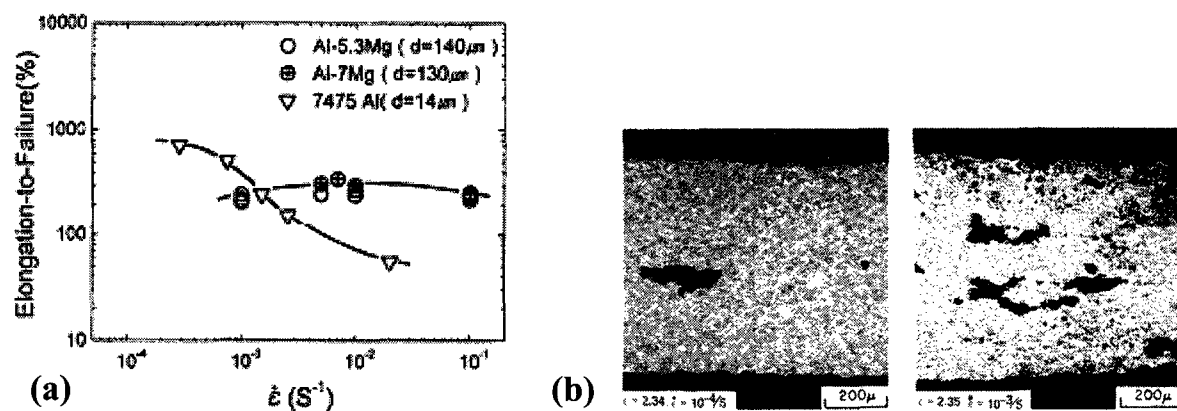
Figure 5.45. (a) Elongation-to-failure vs. strain rate in binary Al-5.3%Mg and Al-7%Mg alloys vs. 7475 Al alloy [17] and (b) the increase in cavitation nucleation with strain rate [131].

In the present work, it was shown in Figures 5.38 and 5.41 that the peak ductilities in the

binary Al-5%Mg alloy were greater than in the AA 5056 alloy when the strain rate employed

was 5×10^{-3} s^{-1}. What is interesting to note is that in the earlier attempts at exploring the

superplastic behavior of the current material, as shown in Figure 4.30, the ductility of the 5056

alloy was *greater* than that of the Al-5%Mg alloy, although in this case the strain rate employed

was 10^{-4} s^{-1}.

5.4.5   Enhanced Ductility Tests Using Reduced Sample Dimensions

Given that the three alloys studied exhibited the high rate sensitivity behaviors described above with m~0.2-0.25, it was decided to decrease the sample gage length so as to explore the possibility of obtaining further increases in ductility. Examples of such tests are given in Figure 5.46 for Al-5%Mg.

Original,
(l_{gage} = 7 mm)

425°C; 185%

450°C; 270%

500°C; 190%
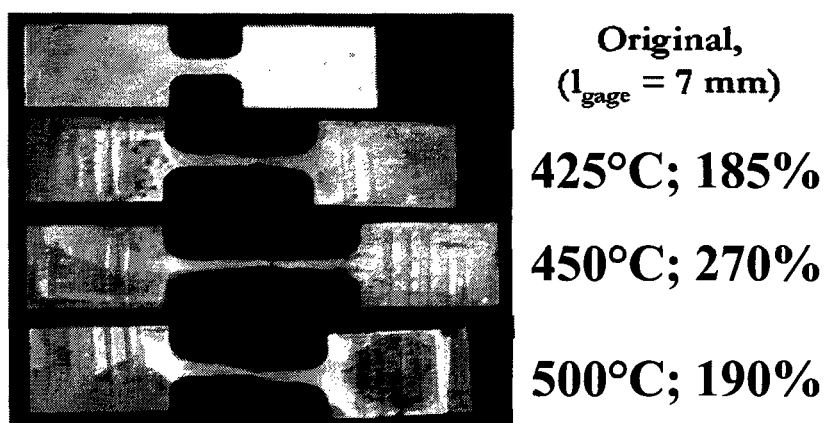
Figure 5.46.   Select shortened Al-5%Mg samples deformed at temperatures in the vicinity of the high strain rate sensitivity peak and at a strain rate of 5x10^{-3} s^{-1}.

As can be seen from Figure 5.46, a peak ductility of 270% was obtained at 450°C and $\dot{\varepsilon}$ = 0.005/s in the Al-5%Mg alloy. This indicated that it is possible to attain ductility values of ~300% in Al-5%Mg, despite the coarse-grained nature of this alloy. Thus, a type of superplasticity or enhanced ductility can be induced in coarse-grained Al-Mg alloys as a result of the unusual increase in rate sensitivity with temperature. Furthermore, the highest values of ductility are observed well below the highest test temperatures. Similar results were observed in Al-3%Mg and AA 5056. These samples are presented in Figures 5.47 and 5.49, respectively; an extension of Figure 5.46 is given in Figure 5.48.
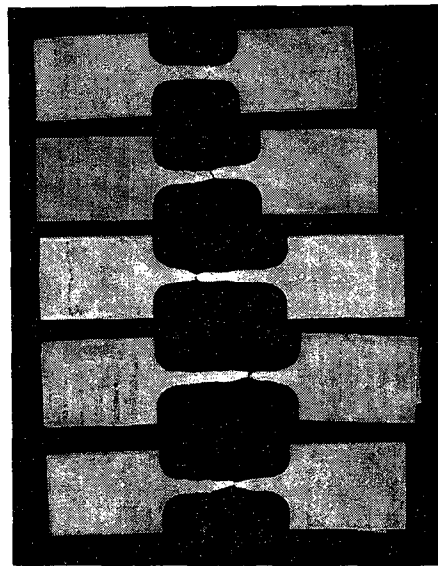
400°C; 55%

425°C; 100%

450°C; 160%

475°C; 185%

500°C; 170%

Figure 5.47.   Shortened Al-3%Mg samples deformed at temperatures in the vicinity of the high strain rate sensitivity peak and at a strain rate of 5×10^{-3} s^{-1}.
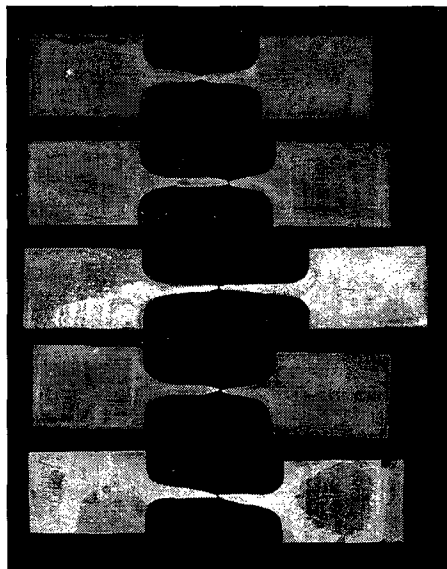
400°C; 140%

425°C; 185%

450°C; 270%

475°C; 170%

500°C; 190%

Figure 5.48.   Shortened Al-5%Mg samples deformed at temperatures in the vicinity of the high strain rate sensitivity peak and at a strain rate of 5×10^{-3} s^{-1}.
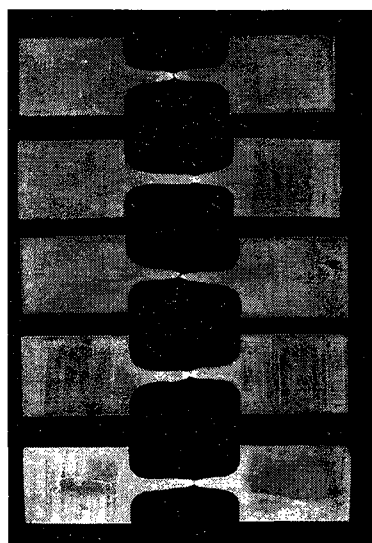
400°C; 125%

425°C; 140%

450°C; 160%

475°C; 160%

500°C; 150%

Figure 5.49. Shortened AA 5056 samples deformed at temperatures in the vicinity of the high strain rate sensitivity peak and at a strain rate of $5x10^{-3}$ s^{-1}.

As can be seen from the preceding figures, a local maximum in elongation occurs in Al-3%Mg at 475°C (Figure 5.47) and Al-5%Mg at 450°C (Figure 5.48), while there is very little change in AA 5056 (Figure 5.49). Figure 5.50 shows three samples of Al-5%Mg that were tested at a strain rate of 10^{-2} s^{-1}. From this figure, it is evident that further tests at higher temperatures are required in order to establish the existence of a local maximum in elongation at this strain rate.

400°C; 115%

425°C; 140%

450°C; 170%

Figure 5.50. Select shortened Al-5%Mg samples deformed at temperatures in the vicinity of the high strain rate sensitivity peak and at a strain rate of 10^{-2} s^{-1}.

Given the small sample cross-section along the gage length, it was crucial to have a surface free from possible sources of stress localization during deformation. Moreover, a small gage cross-section results in very low applied forces and, in turn, a high degree of care is required (e.g. in the load cell, preload, etc.) when applying the load during deformation. For these reasons and the ensuing difficulties in ensuring reproducible results, the sample geometry published in the standard for superplasticity samples (Figure 3.3) was adopted in the further stages of this study. Nevertheless, the results shown in Figures 5.46 to 5.50 reveal values of ductility that exceed those obtained using the sample dimensions in Figure 3.3 at the same temperatures and a strain rate of 5×10^{-3} s^{-1}. Moreover, these results illustrate the potential for enhanced degrees of ductility in these materials.

Another observation made was that the surfaces of the tensile test and superplasticity samples were oxidized during solution heat treatment. With respect to the geometry of the ASTM E8M standard tensile samples, the presence of an oxide layer was not considered a detrimental variable with respect to the recorded values of flow stress at 10% strain. Given the larger gage cross-sectional area, and the fact that tensile deformation was only carried out to 10% (rather than to failure), any effect of the surface oxide layer on the final recorded value of stress at 10% strain - as well as on the observed serrated stress-strain curves - was considered negligible. With a decrease in sample cross-sectional area, it was speculated that the possible depletion of Mg towards the sample surface during heat treatment could reduce the measured value of ductility in the superplasticity samples. Consequently, the reproducibility in the results would be affected. This is explored further in the following section.

5.4.6   Oxidation of Shortened Enhanced Ductility Samples

In order to investigate any possible influence arising from variations in the alloy Mg content on the enhanced ductility behavior of the Al-Mg alloys studied, line scans measuring the Mg content were taken across different sections of the samples shown in Figures 5.46 to 5.50. These were examined in both the as-received condition, as well as after the samples were deformed. In the first case, the line scans were taken across the shoulder section of the sample, while for the deformed samples, the line scans were taken across the gage width from an area just above the fracture tip. For this purpose, a JEOL JXA-8900L WD/RD combined microanalyzer operating at 20 kV and 30 nA was employed, using an electron beam ~1μm in diameter. The solution heat treatment temperature, and in turn, the maximum test temperature, was increased to 500°C.

Given that the thickness of the sample was 1 mm, fifty spot analyses were carried out at intervals of 20 μm to cover the entire area. For line scans taken across larger areas, such as the shoulder width for example, a larger number of readings (~100 spot analyses) was required. Approximately 100 spot analyses at intervals of 10 μm were carried out for the scans taken across the sample thickness in order to cover the region from edge to edge.

Figures 5.51 through 5.55 show typical examples representing the line scan data obtained across these paths for different alloy samples and conditions. The line scans for the three alloys after a solution heat treatment of 450°C/8 hours in air are given in Figure 5.51. As can be seen, there is a reduction in the Mg content towards the edges of the samples.
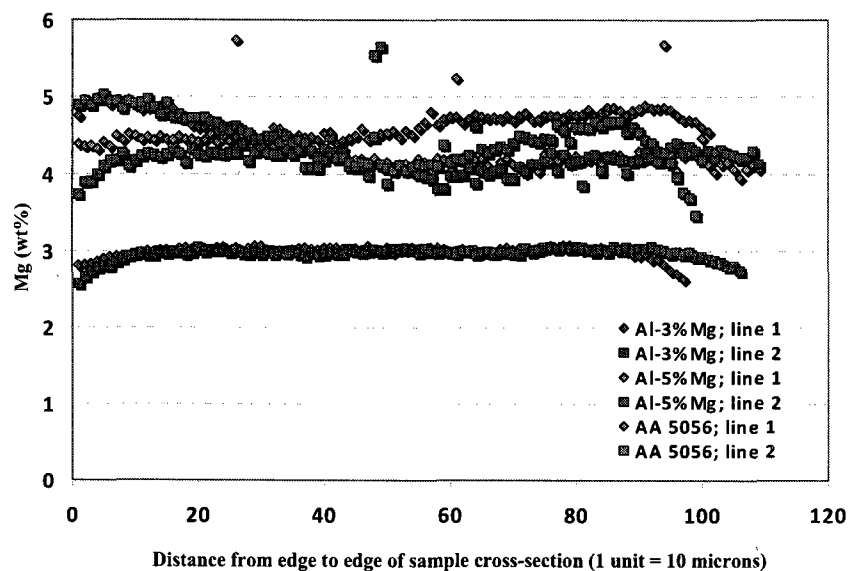
Figure 5.51. Line scans for Al-3%Mg, Al-5%Mg and AA 5056 taken across the 1 mm thickness of the samples after a solution heat treatment at 450°C/8 hours.

The line scans taken across the shoulder cross-sections of samples deformed at 500°C and 5×10^{-3} s^{-1} for Al-3%Mg, Al-5%Mg and AA 5056 are shown in Figure 5.52.
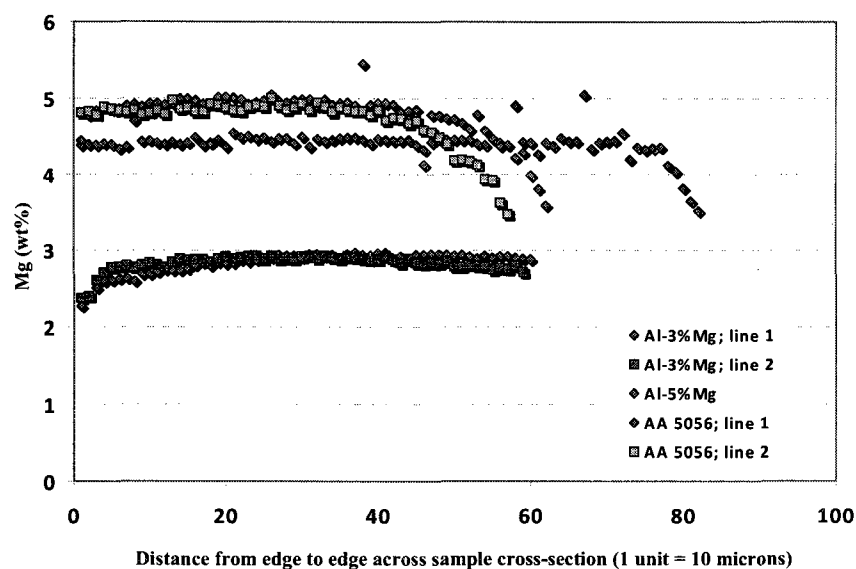
Figure 5.52. Line scans for Al-Mg alloys taken across the 1 mm thickness of the shoulder cross-sections after deformation at 500°C and 5 x 10^{-3} s^{-1}.

These samples were solution treated at 500°C rather than 450°C prior to deformation. The line scans taken for each alloy show that the Mg contents are more or less the same across the shoulder cross-section, yet decrease towards the edge. That is to say that there is a depletion of Mg towards the sample surface to create a visible oxide layer. An extension of Figure 5.52 is presented in Figure 5.53 for AA 5056 deformed at 450°C and 5×10^{-3} s^{-1}.
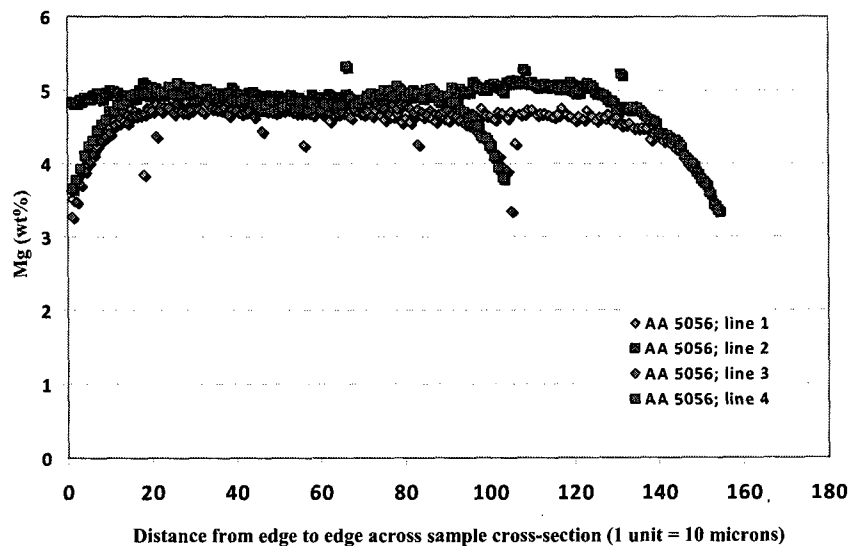
Figure 5.53. Line scans for AA 5056 taken across the 1 mm thickness of the shoulder cross-sections after deformation at 450°C and 5×10^{-3} s^{-1}.

It is evident from Figure 5.53 that there is a marked depletion of Mg towards the sample surface. In view of the fact that these tests were carried out at temperatures of 450°C and 500°C, it was reasonable to conclude that the depletion resulted from the diffusion to the surface and the subsequent oxidation of magnesium.

Line scans were also taken across the sample gage width just before the fracture tip for alloy samples deformed at 450°C and 5×10^{-3} s^{-1} (Figure 5.54). The interval between readings was

held at 20 μm and the line scan length was varied depending on the resulting gage width following deformation.
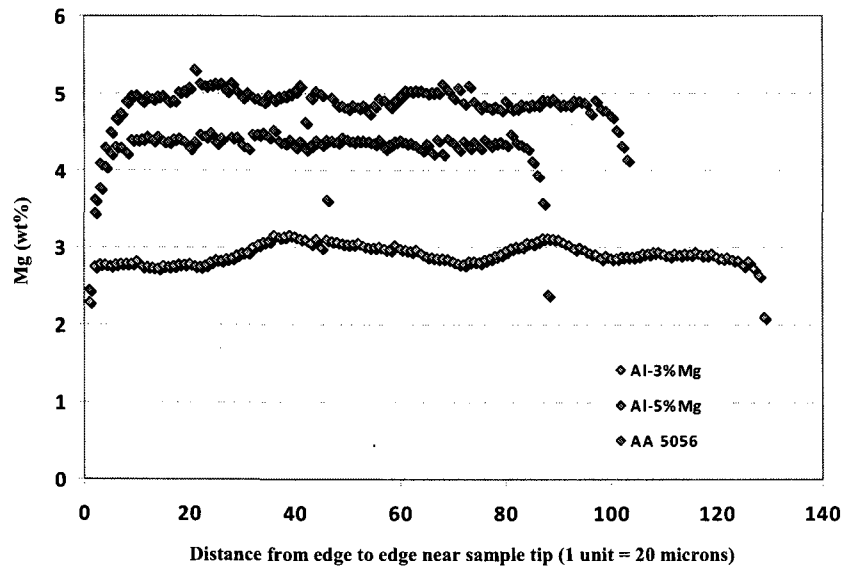
Figure 5.54. Line scans for Al-Mg alloys taken across the gage width, just before the fracture tip, after deformation at 450°C and $5x10^{-3}$ s^{-1}.

As can be seen from Figure 5.54, noticeable drops in Mg content are observed at the edges of the deformed gage length near the fracture tip in the Al-5%Mg and AA 5056. This is also evident in the Al-3%Mg, though it was not as marked as in the other two alloys. Bearing in mind that the superplasticity test samples were deformed in air up to a maximum temperature of 550°C, a certain number of tests were performed under inert gas conditions for comparison purposes. Moreover, the solution heat treatment was also carried out in an inert atmosphere. The resulting line scans for these samples were taken across the sample shoulder cross-section. An example of this is provided in Figure 5.55.
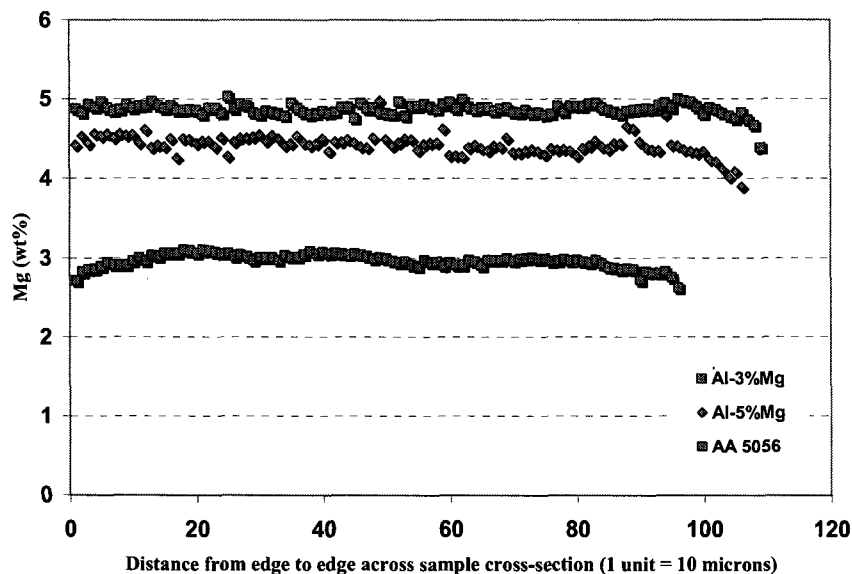
Figure 5.55. **Line scans for Al-Mg alloys taken across the 1 mm thickness of the samples after a solution heat treatment at 550°C/2 hours in argon.**

As can be seen from Figure 5.55, the depletion in Mg content was drastically reduced. More importantly, the solution treatment temperature was increased to 560°C in order to expand the test temperature range for the tests shown in Figures 5.36 to 5.42. These results suggest that higher values of elongation should be achievable when testing samples annealed in inert gas or in a vacuum.

CHAPTER 6

CONCLUSIONS

A study was carried out to investigate the possible superplastic behavior of coarse-grained super-pure Al-3%Mg and Al-5%Mg alloys and of commercial AA 5056 alloys. Flat sheet tensile tests were carried out at various temperatures ranging from -75°C to 450°C at strain rates of 10^{-3} s^{-1}, 10^{-2} s^{-1} and 10^{-1} s^{-1}. The temperature and strain rate dependent flow stress and rate sensitivity behaviors of these alloys were examined. From an analysis of the results obtained, the following may be concluded:

- The three alloys studied exhibited dynamic strain aging (DSA), as evidenced by the presence of a negative strain rate sensitivity region occurring at particular combinations of temperature and strain rate. In this regime, stresses were noted to increase with decreasing strain rate. Moreover, serrated stress vs. strain curves were observed at the temperatures and strain rates comprising the DSA range associated with each alloy.

- The flow stress vs. temperature curves of the three alloys studied were characterized by DSA 'humps'. These 'humps' were seen to shift to higher temperatures as the strain rate was increased.

- In the negative strain rate sensitivity regime, the serrations increased in amplitude with increasing temperature. Moreover, the serration intensity was greater in the Al-5%Mg and AA 5056 alloys than in the Al-3%Mg alloy. This can be attributed to the additional 2wt%Mg, which contributed to increasing the strength of the solute-dislocation interaction. Similarly, the serrations observed in the AA 5056 were more pronounced than in the Al-5%Mg due to the additional alloying elements (Cr, Fe, Mn and Si) found in the AA 5056. The latter also appeared to contribute to the DSA phenomenon.

- Serrations are more pronounced at lower strain rates due to the longer times available for the dislocations to become locked by the diffusing solute clouds. There may also be a machine interaction effect at the lower strain rates.

- Yield point elongations (YPE's) were only observed in the AA 5056. Neither of the binary Al-Mg alloys displayed this behavior. The YPE's can be attributed to the finer grain size of the commercial alloy. A contribution can also be expected from dislocation locking by some combination of the additional alloying elements, i.e. Cr, Fe, Mn and Si.

- The 'humped' stress-temperature curves give rise to 'humped' strain rate sensitivity vs. temperature curves, where the 'humps' also shift to higher temperatures as the strain rate is increased. The rate sensitivity curves for each alloy display a region of higher-than-normal 'm' at increased temperatures, coupled with the negative 'm'

region occurring at lower temperatures. This local maximum in 'm' is associated with the likelihood of a local maximum in elongation.

- The local maximum in 'm' shifts to higher temperatures as the strain rate is increased; nevertheless, it always occurs at temperatures well below the maximum test temperature. The maximum elongation, therefore, is also observed at temperatures below the maximum test temperature.

- Parasite serrations occur when the test samples are not properly polished. Nevertheless, the serrations due to DSA are more pronounced and readily identifiable.

- The commercial purity Al tensile samples display no indication of DSA, as expected. In this case, the stress-strain curves are not serrated at the temperatures and strain rates in which serrations are present in the three alloys. Moreover, the rate sensitivity curves for the c.p. Al all increase monotonically with temperature.

- The activation energy values determined for the appearance and disappearance of serrations in each alloy fall within the range of values found in the literature.

- The ductilities (% elongations) observed in the three alloys for the ASTM E2448-06 superplasticity samples reached local peaks at temperatures below the maximum test temperature. Moreover, the elongation peak in the Al-5%Mg at a strain rate of

5×10^{-3} s^{-1} shifted to a higher temperature when the strain rate was increased to 10^{-2} s^{-1}.

- The E2448-06 AA 5056 superplasticity samples failed via the formation of cavities due to the presence of the second phases. This was not the case in either of the Al-3%Mg or Al-5%Mg binary alloys. The ductilities of the c.p. Al samples increased monotonically with temperature, although only slightly. The 'baseline' c.p. Al ductility curve helps to highlight the 'humps' that are present in the elongation vs. temperature curves for the three alloys.

- The shortened superplasticity samples displayed higher ductilities at the same temperature/strain rate combinations than the standard E2448-06 superplasticity tensile samples. It was possible to minimize oxidation during annealing and testing by using an inert heating atmosphere.

STATEMENT OF ORIGINALITY AND CONTRIBUTION TO KNOWLEDGE

To the best of our knowledge, this is the first time dynamic strain aging in Al-Mg alloys has been linked to enhanced ductility. The characteristics of dynamic strain aging were presented for coarse-grained Al-Mg alloys of varying chemical compositions and linked to the occurrence of a local maximum in the strain rate sensitivity. This local maximum was associated, in turn, with the local maximum in the tensile ductility, expressed as percent elongation. Such "enhanced ductility" or coarse-grained superplasticity eliminates the need for a fine-grained material in order to obtain good formability.

Commercial purity Al was shown to display a gradual increase in 'm' with temperature, although the values never attained levels as high as in any of the three alloys tested. These findings parallel those reported by Barnett and Jonas [51, 52] and Humphreys et al. [53], among others, for dynamic strain aging in (bcc) steel containing interstitial C and N. In *substitutional* fcc systems such as the Al-Mg alloys, evidence of DSA (e.g. serrated stress-strain curves, 'humped' stress-temperature curves, etc.) is much more subtle than in the interstitial systems. As a result, the evidence presented here was more difficult to obtain and departs further from the existing literature.

This required the employment of a particularly wide range of temperatures so that the start of the negative strain rate sensitivity regime could be carefully monitored at lower

temperatures than conventionally used. In a similar way, testing was extended to much higher temperatures so that the end of the higher-than-normal 'm' region could be accurately defined. Consequently, for the strain rates used in this study, an extra wide temperature range of -75°C to 450°C was employed for the standard tensile tests. This range was increased to 550°C for the enhanced ductility tests in order to obtain a more 'complete picture' of the higher-than-normal 'm' behavior via actual values of enhanced ductility in the shortened tensile samples.

The results obtained provide an alternative to the conventional view that enhanced ductility in Al-Mg alloys is due to solute drag. A strong case is made for the contention that it is associated with dynamic strain aging effects instead.

REFERENCES

1.   E. Romhanji, M. Dudukovska and D. Glišić, *J. of Mater. Proc. Technol.*, **125-126** (2002), 193-198.

2.   F. Musin, R. Kaibyshev, Y. Motohashi and G. Itoh, *Metall. Mater. Trans. A*, **35A** (2004), 2383-2392.

3.   J.R. Cho, W.B. Bae, W.J. Hwang and P. Hartley, *J. of Mater. Proc. Technol.*, **118** (2001), 356-361.

4.   R. Verma, A.K. Ghosh, S. Kim and C. Kim, *Mater. Sci. Eng. A*, **191** (1995), 143-150.

5.   D. Li and A. Ghosh, *Mater. Sci. Eng. A*, **352** (2003), 279-286.

6.   V.N. Perevezentsev, V.N. Chuvil'deev, V.I. Kopylov, A.N. Sysoev and T.G. Langdon, *Ann. Chim. Sci. Mat.*, **27** (2002), 99-109.

7.   S. Komura, P.B. Berbon, M. Furukawa, Z. Horita, M. Nemoto and T.G. Langdon, *Scripta Mater.*, **38** (1998), 1851-1856.

8.   H. Akamatsu, T. Fujinami, Z. Horita and T.G. Langdon, *Scripta Mater.*, **44**(2001), 759-764.

9.   A.A. Tavassoli, S.E. Razavi and N.M. Fallah, *Metall. Trans. A*, **6A** (1975), 591-594.

10. E.M. Taleff, D.R. Lesuer and J. Wadsworth, *Metall. Mater. Trans. A*, **27A** (1996), 343-352.

11. M. Otsuka, S. Shibasaki and M. Kikuchi, *Mater. Sci. Forum*, **233-234** (1997), 193-198.

12. K.A. Padmanabhan, R.A. Vasin and F.U. Enikeev, Superplastic Flow: Phenomenology and Mechanics, Springer-Verlag, (2001).

13. T.G. Nieh, J. Wadsworth and O.D. Sherby, "Superplasticity in Metals and Ceramics", Cambridge University Press; 1997.

14. O.D. Sherby and J. Wadsworth, *Prog. Mater. Sci.*, **33** (1989), 169-221.

15. G.E. Dieter, Mechanical Metallurgy SI Metric Edition, McGraw Hill Book Company, (1988).

16. T. Sakuma, *Current Opinion in Solid State and Materials Science*, **2** (1997), 296-299.

17. S.S. Woo, Y.R. Kim, D.H. Shin and W.J. Kim, *Scripta Mater.*, **37** (1997), 1351-1358.

18. E.M. Taleff, G.A. Henshall, T.G. Nieh, D.R. Lesuer and J. Wadsworth, *Metall. Mater. Trans. A*, **29A** (1998), 1081-1091.

19. B. Baudelet, *Mater. Sci. Eng.*, **A137** (1991), 41-55.

20. Z. Horita, M. Furukawa, M. Nemoto, A.J. Barnes and T.G. Langdon, *Acta Mater.*, **48** (2000), 3633-3640.

21. R. Sawle, Superplastic Forming of Structural Alloys – Conference Proceedings, The Metallurgical Society of AIME (1982), 307-317.

22. A. Arieli and R.B. Vastava, Superplastic Forming – Conference Proceedings, ASM (1984), 70-75.

23. C. Bampton, F. McQuilkin and G. Stacher, Superplastic Forming – Conference Proceedings, ASM (1984), 76-83.

24. H. Watanabe, H. Tsutsui, T. Mukai, M. Kohzu, S. Tanabe and K. Higashi, *Int. J. Plasticity*, **17** (2001), 387-397.

25. P. Griffiths and C. Hammond, *Acta Metall.*, **20** (1972), 935-945.

26. J.P. Chu, I.M. Liu, J.H. Wu, W.Kai, J.Y. Wang and K. Inoue, *Mater. Sci. Eng. A*, **258** (1998), 236-242.

27. X. Wu and Y. Liu, *Scripta Mater.*, **46** (2002), 269-274.

28. K.D Woo, S.W. Kim, C.H. Yang, T.P. Lou and Y. Miura, *Mater. Letters*, **57** (2003), 1903-1909.

29. A.R. Chezan and J.Th.M. De Hosson, *Mater. Sci. Eng. A*, **410-411** (2005), 120-123.

30. T.G. Nieh, L.M. Hsiung, J. Wadsworth and R. Kaibyshev, *Acta Mater.*, **46** (1998), 2789-2800.

31. J.G. Morris, *Mater. Sci. Eng.*, **13** (1974), 101-108.

32. P.G. McCormick, *Acta Metall.*, **19** (1971), 463-471.

33. I.S. Kim and M.C. Chaturvedi, *Mater. Sci. Eng.*, **37** (1999), 165-172.

34. K. Chinab, Y. Estrin, L.P. Kubin and J. Vergnol, *Scripta Metall.*, **21**(1987), 203-208.

35. W. Wen and J.G. Morris, *Mater. Sci. Eng.* **A354** (2003), 279-285.

36. F.B. Klose, A. Ziefenbein, F. Hagemann, H. Neuhauser, P. Hahner, M. Abbadi and A. Zeghloul, *Mater. Sci. Eng.* **A369** (2004), 76-81.

37. F.B. Klose, F. Hagemann, P. Hahner and H. Neuhauser, *Mater. Sci. Eng.* **A387-389** (2004), 93-97.

38. P.G. McCormick, *Scripta Metall.*, **4** (1970), 221-224.

39. J.G. Morris, *Mater. Sci. Eng.*, **9** (1972), 361-367.

40. J.G. Morris and H.K. Howard, *J. Appl. Phys.*, **42** (1971), 3252-3254.

41. C.P. Hinesley and J.G. Morris, *Mater. Sci. Eng.*, **6** (1970), 48-54.

42. J.G. Morris, *Mater. Sci. Eng.*, **5** (1969), 299-302.

43. J.G. Morris and B.J. Roopchand, *Mater. Sci. Eng.*, **17** (1975), 77-80.

44. A. Gilat and X. Wu, *Int. J. Plasticity*, **6-7** (1997), 611-632.

45. A. Benallal, T. Borvik, A. Clausen and O. Hopperstad, *Technische Mechanik*, **23** (2003), 160-166.

46. A. Benallal, T. Berstad, T. Borvik, A.H. Clausen and O.S. Hopperstad, *European J. Mech. A/Solids*, **25** (2006), 397-424.

47. R.C. Picu, *Acta Mater.*, **52** (2004), 3447-3458.

48. L.P. Kubin and Y. Estrin, *J. Phys. III*, **1** (1991), 929-943.

49. B.A. Wilcox and A.R. Rosenfield, *Mater. Sci. Eng.*, **1** (1966), 201-205.

50. M. Lebyodkin, Y. Brechet, Y. Estrin and L.P. Kubin, *Acta Mater.*, **44** (1996), 4531-4541.

51. M.R. Barnett and J.J. Jonas, *ISS 37th Mechanical Working and Steel Processing Conference* (1995), 39-45.

52. M.R. Barnett and J.J. Jonas, *ISIJ Int.*, **37** (1997), 697-705.

53. A.O. Humphreys, D.S. Liu, M.R. Toroghinezhad and J.J. Jonas, *ISIJ Int.*, **42** (2002), Supplement.

54. D.S. Liu, A.O. Humphreys, M.R. Toroghinezhad and J.J. Jonas, *ISIJ Int.*, **42** (2002), 751-759.

55. M.R. Barnett and J.J. Jonas, *ISIJ Int.*, **39** (1999), 856-873.

56. L.P. Troeger and E.A. Starke Jr., *Mater. Sci. Eng.* **A277** (2000), 102-113.

57. T.G. Nieh, A.J. Schwartz and J. Wadsworth, *J. Mater. Sci. Eng. A*, **208** (1996), 30.

58. O.D. Sherby and J. Wadsworth, *Prog. Mater. Sci.*, **33** (1989), 169-221.

59. U.F. Kocks, Superplastic Forming of Structural Alloys – Conference Proceedings, The Metallurgical Society of AIME (1982), 41-55.

60. D.B. Laycock, Superplastic Forming of Structural Alloys – Conference Proceedings, The Metallurgical Society of AIME (1982), 257-271.

61. A.A. Tavassoli, S.E. Razavi and N.M. Fallah, *Metall. Trans.*, **6A** (1975), 591-594.

62. M.S. Mostafa and M.A. Mohamed, *Metall. Trans.*, **17A** (1986), 365-366.

63. P.K. Chaudhury and F.A. Mohamed, *Metall. Trans.*, **18A** (1987), 2105-2114.

64. T.R. McNelley, D.J. Michel and A. Salama, Advances in Superplasticity and Superplastic Forming, The Minerals, Metals and Materials Society (1993), 45.

65. D.A. Woodford, Technical Notes for Transactions of the ASM, **62** (1969), 291-293.

66. J.A. Wert, Superplastic Forming of Structural Alloys – Conference Proceedings, The Metallurgical Society of AIME (1982), 69-83.

67. D.H. Bae and A.K. Ghosh, *Acta Mater.,* **50** (2002), 511-523.

68. D.H. Bae and A.K. Ghosh, *Acta Mater.,* **50** (2002), 993-1009.

69. D.H. Bae and A.K. Ghosh, *Acta Mater.,* **50** (2002), 1011-1029.

70. D. Delafosse, G. Lapasset and L.P. Kubin, *Scripta Metall. Mater.*, **29** (1993), 1379-1384.

71. P.G. McCormick, *Acta Metall.*, **36** (1988), 3061-3067.

72. M.R. Winstone, R. D. Rawlings and D.R.F. West, *J. Less Common Metals*, **31** (1973), 143-150.

73. S.D. Mesarovic, *J. Mech. Phys. Solids*, **43** (1995), 671-700.

74. A.K. Taheri, T.M. Maccagno and J.J. Jonas, *ISIJ Int.*, **35** (2002), 1532.

75. E. Pink and A. Grinberg, *Mater. Sci. Eng.*, **51** (1981), 1-8.

76. R.A. Mulford and U.F. Kocks, *Acta Metall.*, **27** (1979), 1125-1134.

77. H.J. Harun and P.G. McCormick, *Acta Metall.*, **27** (1979), 155-159.

78. J.G. Morris, *Mater. Sci. Eng.*, **16** (1974), 79-84.

79. Y.V.R.K. Prasad, D.H. Sastry and K.I. Vasu, *Mater. Sci. Eng.*, **6** (1970), 327-333.

80. L.P. Kubin, Y. Estrin and C. Perrier, *Acta Metall. Mater.*, **40** (1992), 1037-1044.

81.   R.B. Schwarz, *Scripta Metall.*, **16** (1982), 385-390.

82.   A. van den Beukel and U.F. Kocks, *Acta Metall.*, **30** (1982), 1027-1034.

83.   A. Wijler and J. Schade van Westrum, *Scripta Metall.*, **5** (1971), 159-164.

84.   A.T. Thomas, *Acta Metall.*, **14** (1966), 1363-1374.

85.   A.W. Sleeswyk, *Acta Metall.*, **6** (1958), 598-603.

86.   P.G. McCormick, *Acta Metall.*, **20** (1972), 351-354.

87.   P.G. McCormick and Y. Estrin, *Scripta Metall.*, **23** (1989), 1231-1234.

88.   V.A. Phillips, A.J. Swain and R. Eborall, *J. Inst. Metals*, **81** (1952), 625.

89.   A.H. Cottrell, <u>Dislocations and Plastic Flow in Crystals</u>, Oxford University Press (1953).

90.   A. van den Beukel, *Acta Metall.*, **28** (1980), 965-969.

91.   R. McCallum, S. Yue and J.J. Jonas: *Wire J. Int.*, **27** (1994), 102-107.

92.   L.P. Kubin, K. Chinab and Y. Estrin: <u>Patterns, Defects and Microstructures in Nonequilibrium Systems</u> (1986), 220-236.

93.   D. Blanc and J.L. Strudel, Proceedings of the 7th International Conference on the Strength of Metals and Alloys, Pergamon Press (1985), 349-354.

94.   E. Pink and A. Grinberg, *Acta Metall.*, **30** (1982), 2153-2160.

95.   H. Fujita and T. Tabata, *Acta Metall.*, **25** (1977), 793-800.

96.   J.D. Baird, "Chapter 8: Dynamic Strain Aging" in <u>The Inhomogeneity of Plastic Deformation</u>, ASM, (1973), 191.

97.   J.M. Robinson and M.P. Shaw, *Int. Mater. Rev.*, **39** (1994), 113.

98.   B.J. Brindley and P.J. Worthington, *Metall. Rev.*, **15** (1970), 101-114.

99.   C.C. Li and W.C. Leslie, *Metall Trans* **9A** (1978), 1765.

100.   L. Shi and D.O. Northwood, *Acta Metall. Mater.*, **43** (1995), 453-460.

101.   K. Dehghani, *Ph.D. Thesis*, McGill University (1999).

102.   N. Romani, A.O. Humphreys and J.J. Jonas, *Can. Metall. Quart.*, **45** (2006), 451-458.

103.   R.C. Picu, G. Vincze, F. Ozturk, J.J. Gracio, F. Barlat and A.M. Maniatty, *Mater. Sci. Eng.* **A390** (2005), 334-343.

104. A. Wijler, M.M.A. Vrijhoef and A. van den Beukel, *Acta Metall.*, **22** (1974), 13-19.

105. M.R. Winstone and R. D. Rawlings, *J. Mater. Sci.*, **6** (1971), 1355.

106. P. Rodriguez, *Bull. Mater. Sci.*, **6** (1984), 653.

107. A.H. Cottrell, *Phil. Mag.*, **44** (1953), 829.

108. P.J. Worthington and B.J. Brindley, *Phil. Mag.*, **19** (1969), 1175.

109. G.R. Stewart, *Ph.D. Thesis*, McGill University (2004).

110. D. Lobo, *M.Eng. Thesis*, McGill University (2000).

111. S. Cunningham, *M.Eng. Thesis*, McGill University (1999).

112. D. Park and J.G. Morris, *Scripta Metall. Mater.*, **29** (1993), 365-369.

113. D. Thevenet, M. Mliha-Touati and A. Zeghloul, *Mater. Sci. Eng.* **A266** (1999), 175-182.

114. M. Abbadi, P. Hahner and A. Zeghloul, *Mater. Sci. Eng.* **A337** (2002), 194-201.

115. N. Q. Chinh, F. Csikor, Zs. Kovács, J. Lendvai, *J. Mater. Res.*, **15** (2000), 1037-1040.

116. B.J. Brindley and P.J. Worthington, *Acta Metall.*, **17** (1969), 1357-1361.

117. D. Munz and E. Macherauch, *Z. Metallk.* **57** (1966), 552.

118. O. Vohringer and E. Macherauch, *Z. Metallk.* **58** (1967), 317.

119. W. Charnock, *Phil. Mag.*, **18** (1968), 89.

120. K. Mukherjee, C. D'Antonio and R. J. Maciag, *Scripta Metall.*, **4** (1970), 209-212.

121. A.R.C. Westwood and T. Broom, *Acta Metall.*, **5** (1957), 249-256.

122. A. Inagaki, T. Komatsubara and H. Inagaki, *J. Japan. Inst. Light Metals*, **48** (1998), 312-316.

123. E.J. Hearn, Mechanics of Materials: An Introduction to the Mechanics of Elastic and Plastic Deformation of Solids and Structural Components, 2nd ed., Permagon Press (1985), 5.

124. D.J. Lloyd, S.A. Court and K.M. Gatenby, *Mater. Sci. Tech.* **13** (1997), 661.

125. J.M. Robinson and M.P. Shaw, *Mater. Sci. Eng.* **A159** (1992), 159-165.

126. E. Romhanji, D. Glišić and V. Milenković, *Mater. Technol.*, **35** (2001), 22.

127. G. de With, Structure, Deformation and Integrity of Materials – Volume II: Plasticity, Visco-elasticity and Fracture, Wiley-VCH (2006), 525.

128. J.E. King, C.P. You and J.F. Knott, *Acta Metall.*, **29** (1981), 1553-1566.

129. S.L. Semiatin and J.J. Jonas, Formability and Workability of Metals, ASM (1984), 179.

130. D.J. Lloyd and D.M. Moore, Superplastic Forming of Structural Alloys – Conference Proceedings, The Metallurgical Society of AIME (1982), 147-172.

131. A.K. Ghosh, Superplastic Forming of Structural Alloys – Conference Proceedings, The Metallurgical Society of AIME (1982), 85-103.